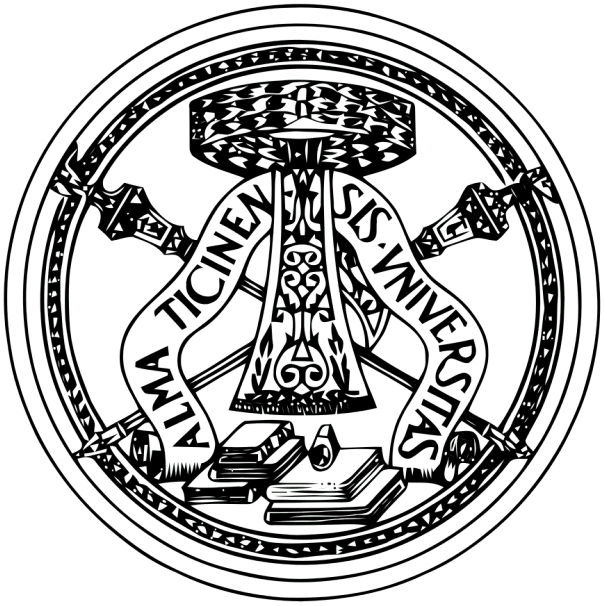

Università di Pavia
PhD program in Electronics, Computer Science and Electrical Engineering
Faculty of Engineering

Innovative high spectral purity DPSS lasers for LIDAR systems

Dissertation for the degree of philosophiae doctor (PhD)
at the University of Pavia, Dipartimento di Ingegneria Industriale,
Laser Source Laboratory

Author: Jacopo Rubens Negri

Supervisor: Federico Pirzio

Ph.D. Thesis of Jacopo Rubens Negri

XXXIII cycle

Year 2020

Year: 2020
Title: Monograph thesis at the University of Pavia
Author: Jacopo Rubens Negri
Signature:

A Patrizia

Acknoledegment

Before to start, I would like to write few lines for all the people that have been close to me during this experience of professional and personal growth.

First, I specially thank my supervisor Federico Pirzio, for his tireless intellectual vivacity and enthusiasm, for his indispensable advice, for the knowledge transmitted throughout the Ph.D. course. Equally fundamental to the development of my skills and knowledge was Professor Antonio Agnesi, whom I also thank.

To all the colleagues, who have accompanied me on this journey and who have been points of reference for discussing and growing together, I extend a warm thanks to Paolo Farinello, Etienne Caracciolo, Luigi Fregnani, Simone Tacchini, Francesca Demetrelli and Sara Pizzurro. Furthermore, I would like to thank all the engineering members of the University of Pavia and of the Bright Solutions Research and Development department group, with whom I have shared during these years, an atmosphere of great professionalism and serenity.

The Ph.D. course also allowed me to compare myself and grow abroad, specifically in Stockholm. Here I was able to test myself and cultivate new experiences on an academic, methodological and cultural level. I thank Professors Valdas Paskevicius and Fredick Laurell for their hospitality and I am grateful to have collaborated with the many colleagues of the KTH, in particular with Ph.D. student Kjell Molster.

A special thanks goes to my family and in particular to my parents Claudio and Patrizia who have always encouraged me to continue my studies and have always supported me in this long journey. Not secondary was the support of all the other numerous members of my family, such as my grandparents: Albino and Luisa, my sisters: Francesca and Veronica, my uncles: Carlo, Cristina, Agostino, Anna, Renato, Cristina, Eolo, my cousins: Nicolò, Flavio, Barbara, Michele, Francesco, Ilaria, my brother/sister-in-law Nikita, Elisa and my nephews: Katerina, Anastasia and Leonid.

A further thanks goes to the friendships with Matteo, Laura, Francesco, Potter, Manuele, Mattia, Riccardo, Stefano and to the people who have studded my daily life such as Gianni, Roberto and Serena. I also thank Cinzia, Lucia, Pina, Vittorio.

Finally, I thank Valentina, for all the smiles you have given me and that you continue to give me by staying close to me.

Without all these supports it would not have been possible to achieve these goals, as well as a building without foundations. I wish to dedicate the result of all these years of study and research to my mother Patrizia, hoping to make her proud.

Abstract

An innovative oscillator for solid-state laser technology is developed for Single-Longitudinal-Mode (SLM) operation, enabling narrow bandwidth, low pulse-to-pulse time jitter, laser emission at 1064 nm. The system realized is fully characterized in terms of power, energy, spatial, temporal and spectral performance. The technology developed is defined Self Injection Seeding Ring Oscillator (SISRO), which enables to generate close to transform limited pulses with remarkable reliability and unparalleled simplicity. Both Coherent Doppler LIDARs (CDL) and High Spectral Resolution LIDARs (HSRL) can benefit from this technology, in terms of cost-efficiency, reliability and complexity. An additional significant advantage introduced by the SISRO laser architecture is modularity. This property allows to tailor the technology to the desired application and LIDAR system. Both CDL and HSRL are thus presented, after the fundamental principles governing standard LIDAR techniques have been introduced. CDL is intended to measure the motion of winds whereas HSRL is employed for discrimination between molecules and particulate matter. In both applications, the systems share the need of a laser source able to generate narrow bandwidth pulses in order to discriminate spectral broadening induced into the backscattered radiation.

The SISRO technique exploits a unidirectional ring architecture to suppress Spatial Hole Burning (SHB), which is the main antagonist to SLM operation. Unidirectional propagation and thus SLM operation is achieved by means of self-seeding. The SISRO technique emerges as an appealing candidate for Master Oscillator Power Amplifier (MOPA) architectures, because of the good spatial, spectral, temporal properties and the significant pulse energies involved (μJ order), which can be easily scaled depending on the application. It is also discussed nonlinear techniques to extend the wavelength operation. Indeed, conventional laser systems struggle to access specific wavelengths, which are required for both physical reasons and health considerations, such as laser safety. Nonlinear devices enable to shift conventional high energies laser to exotic wavelengths. In this elaborate is presented nonlinear parametric oscillators for wavelength extension from 1 μm to the Short-Wavelength InfraRed (SWIR) region (1.8-2.5 μm).

Each part is independently addressed in different chapters of this work. First, it is introduced the LIDAR technology and optical requirements. Then, the optical theory necessary to develop the SISRO, such as Passive Q-Switching and SLM operation, is described. Subsequently, the novel SISRO laser and the several iterations of the architecture based on Neodymium active materials are presented. The key parameters governing the SISRO performance and especially stability are also investigated in details, while the reader is also made aware of the typical trends associated with comparable technologies. Experimental results and theoretical predictions are thoroughly discussed, in order to understand the advantages offered by the SISRO technique and to devise suggestions to overcome its major limitations. The nonlinear theory for wavelength extension is thereafter introduced. Both Optical

Parametric Ocillators (OPO) and Backward-Wave Optical Parametric Oscillators (BWOPO) systems are described, in combination with an Optical Parametric Amplifier (OPA) aimed at the extension of the spectral coverage offered by traditional bulk devices. In these regards, particular attention is dedicated to the spectral performance, showing the trade-off between these two oscillators technologies.

During the course of my PhD I had in particular the opportunity to cooperate with Bright Solutions Srl. The thesis is organized as follows:

- *Chapter (1)* introduces LIDAR systems and their applications. Then, it is outlined the possible physical process involved in atmospheric LIDAR and the emitter requirements, especially for CDL and HSRL systems.
- *Chapter (2)* presents the Single Longitudinal Mode laser operation and Q-Switching laser theory. It is then described the possible techniques to be employed to force SLM operation, focusing on the seeding technique which constitutes the basis for the Self Injection Seeded Ring Oscillator (SISRO).
- *Chapter (3)* describes the SLM investigation of the SISRO design. Three ring laser oscillators are tested to verify SLM operation and the technology potential.
- *Chapter (4)* illustrates the ring laser oscillator improvement to enhance SLM stability by means of a new ring laser design and mechanical support. Then it is described how to pulse-to-pulse time jitter was reduced, after developing a mathematical model.
- *Chapter (5)* describes nonlinear parametric optical theory for wavelength extension to the SWIR spectral region. Specifically, it is described optical parametric oscillators and the technologically emerging optical Backward-Wave Parametric Oscillators (BWOPO), also named as Mirrorless Optical Parametric Oscillators (MOPO).
- *Chapter (6)* presents the thesis conclusion, outlining the most important results.
- *Appendix (A)* illustrates the mechanical part developed with CAD for the SISRO technology.

Contents

List of Figures

List of Tables

Chapter 1

LIDAR technology

The acronym LIDAR stands for Light Imaging Detection And Ranging. LIDAR is analogous to RADAR (RAdio Detection And Ranging) and SODAR (SOund Detection and Ranging), all these technologies exploit waves (either electromagnetic or acoustic) to gather informations about the surrounding environment or to vehicle informations through space. Radar operates emitting electromagnetic waves in the radio frequency spectral region spanning from tens of MHz to hundreds of GHz. For higher frequencies, conventionally the radiation belongs to the optical domain. Indeed, for frequencies extending from units to thousands of THz (which corresponds to wavelengths spanning from far infrared, i.e., 10-μm to the deep UV, i.e., 100-nm), the device is no more called RADAR, but instead it is identified as LIDAR. Depending on the wavelength chosen and the properties of the light emitted, it is possible to employ this technology in an impressively large variety of fields, such as:

- *Range finding, target identification and tracking (military):* Land platforms such as tanks or self-propelled artillery as well airborne systems like UAVs (Unmanned Aerial Vehicles) can take advantage of LIDAR devices to enhance battle awareness, to improve effective counter-measures and to gather informations about different threats, such as chemical or biological agents [1]. LIDARs allow to enhance offensive actions too, enabling automated target acquisition for weapons systems, e.g, missiles [2, 3, 4].
- *Autonomous driving:* Probably the most iconic LIDAR application, the self-driving cars [5] or trucks would enable at first an impressive improvement for passengers safety, considering only the thousands of casualties and injuries in the European Union alone [6]. Furthermore, LIDAR could allow automated transportation of people and goods. This would result in traffic reduction and more efficient viability [7, 8].
- *Topography:* LIDAR are able to 3-dimensionally map the earth surface and coastal regions with unprecedented resolution, allowing even to identify foliage and buildings as well as ground morphology, [9, 10, 11, 12].
- *Agriculture:* Monitoring crops field with LIDAR, enables to control the growth rate and to locate infesting plants, realizing more productive cultivations and reducing the use of chemical substances. [13, 14, 15]. LIDARs would improve automation in this sector, leading to an increase of productivity and efficiency [16].
- *Medical application:* LIDARs can be used also for diagnosis and disease monitoring. It has been reported detection of cancer tissues by LIDAR-RADAR hybrid system [17].

- *Mining:* A profitable extraction of raw minerals and other soil resources is a critical component for many nations economies. The use of LIDAR allows to gather informations on ore volumes, penetrating earth's surface. LIDAR technology would boost investments and improve mine structures revenues [18, 19, 20].

- *Pollution monitoring:* The amount of pollutant concentration in the atmosphere or deposited on surfaces can be measured and monitored with LIDARs. This approach would permit to identify toxic areas for human activities as well as to preserve environmental heritage [21, 22, 23, 24, 25, 26, 27].

- *Green Energy Improvement:* Wind-Turbines can drastically improve their performance by means of LIDARs. High spatial and temporal resolution wind and turbolence measurements carried out from the ground up to several hundred meters of altitude, can significantly aid the design of highly efficient turbine rotors for eolian energy generation [28, 29, 30, 31, 32, 33, 34, 35].

- *Meteorology:* Weather forecasting is extremely important for all economic activities impacted by atmospheric conditions at a certain place and time, including fog, haze, smog, heavy wind, rain, snow and other critical events. Most natural disasters stem from severe weather phenomena. Worst of all, these disasters often lead to human casualties and property damage. The use of LIDARs improves the detection and forecast of hazardous meteorological events allowing to execute timely emergency response and rescue operations [36, 37, 37, 38, 39, 40, 41].

- *Aviation:* LIDARs enable safety and efficiency in this field. Airports use LIDARs to gather real-time and highly accurate wind and aerosol measurements adapted to the airport environment, providing critical information that helps ensure safe takeoffs and landings, improving the overall air traffic management [42, 43].

As described above LIDARs can be employed by a large variety of utilizers for several different applications. LIDAR platforms can be static and dynamic as well. Cars, trucks, boats, ships, planes and satellites platform have been equipped already with LIDAR systems. This is a clear indication of LIDAR technology flexibility, which traduces in several successful market products.

The LIDAR market is constantly growing in the last years, reaching a value between 800 millions of USD and 1.2 billion of USD in 2019 [44, 45, 46, 47]. A strong market expansion is expected in this sector, expecting values ranging from 2 billion to 6 billion of USD in 2024. A non-exhaustive list of the leading companies in this sector for their impact on the market are: Teledyne Technologies (US), Hexagon (Sweden), Trimble (US), FARO (US), RIEGL (Austria), SICK AG (Germany), Quantum Spatial (US), Beijing Beiketian Technology Co., Ltd. (China), Velodyne LIDAR (US), and YellowScan (France).

LIDAR system can be decomposed in several key elements, illustrated in Fig. (1.1). The emitter is the core of the LIDAR system. It is responsible to generate the light probe with suitable properties in order to select a suitable interaction with the target. The receiver is the optical sensor able to detect a small fraction of the light probe returning to the LIDAR. After the collection of the returning signal, a series of signal-processing and data-processing devices can be found, e.g, optical spectrum analyzers and computers. All the system components are powered by a mission compatible energy source (e.g, batteries or a power link

to the LIDAR platform). The beam steering mechanism is the LIDAR component responsible of directing the light probe toward the desired target. Electronics provides an appropriate control of all the above mentioned components, as well timing references. The tracker is necessary in order to determine the LIDAR position with respect to the target. Finally the system frame must be a suitable architecture for the chosen application, considering the mechanical requirements and the cost-effectiveness.

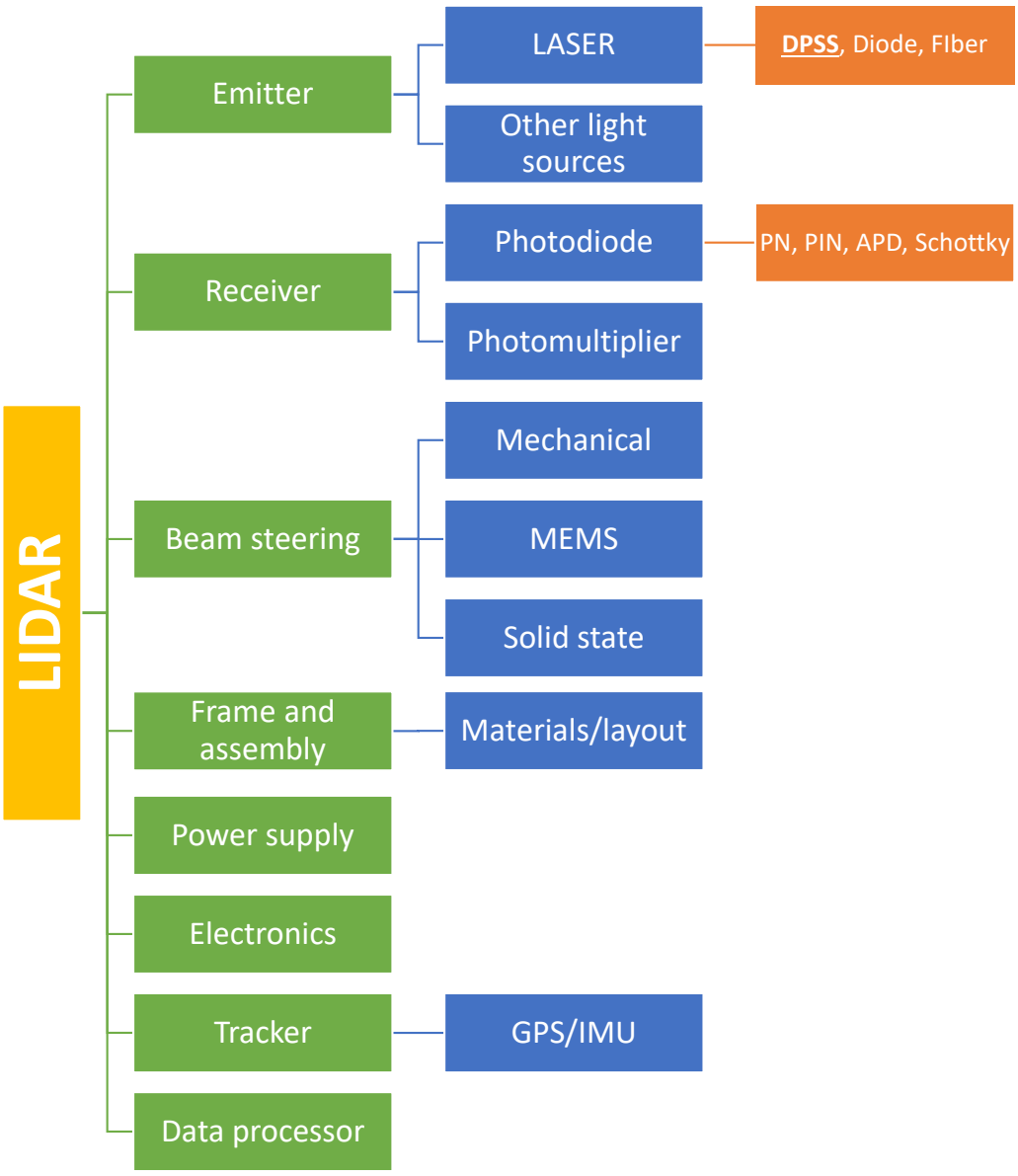

Figure 1.1: *LIDAR system components, the DPSS lasers are the main topic of this elaborate*

LIDAR systems can be classified in several ways depending on applications, requirements, scan rate, cost and transportability. However, it is possible to identify a LIDAR classification based on the physical effect involved between the light probe generated and the target. This description allows to point out the motivation of my work. In this Ph.D. thesis we will focus on the emitter component, namely the Diode-Pumped Solid-State (DPSS) laser category.

1.1 LIDAR typologies

The LIDAR basic function is the ToF measurement, in order to locate the target likewise Radar. Lidars can obtain a returning signal exploiting different optical phenomena. Certain Lidar categories are even able to fulfill multiple measures at the same time in order to gather more data about the target, relying on multiple phenomena. LIDAR classification is made up by [48]:

- *LIDARs based on reflection:* This typology is employed when it is expected a strong signal reflection from the target. The signal received will show spikes emerging from a noise floor. These spikes are generated by reflections coming back from the solid or liquid reflecting targets and emerge as the dominant components in the received signal. The multiple echos permit to identify obstacles and even to determine to a certain extent the shape of the target.

- *Elastic back-scattering LIDARs:* This kind of devices, usually referred to as Rayleigh-Mie LIDARs, acquire data about the presence and the location of aerosols and cloud layers. Indeed, Rayleigh and Mie scattering are specific case of elastic scattering, "elastic" because the energy (therefore the frequency/wavelength) of the scattered photon is equal to the incident one. The Rayleigh scattering intensity is proportional to λ^{-4}, then this regime takes place when light interacts with particles smaller than the wavelength, such as oxygen and nitrogen molecules. When the diameter of the particulate is similar or greater than the wavelength, the regime is typically named Mie scattering. However, the scattering from very large particles does not depend on the wavelength [48]. Mie scattering theory is often a rough approximation. For non spherical large particles Mie scattering is inappropriate, but more elaborate scattering theories are required.

  High Spectral Resolution LIDARs (HSRL) are a particular sub-category, which improve drastically the LIDAR performance for aerosol transmission and light exinction properties [48]. This system will be further discussed in Sect. (1.3.1).

  Coherent Doppler LIDARs (CDL) use the Doppler effect on the laser spectrum to recover information about the target motion. Several sub-categories exist depending on how the information is recovered. They are Time of Flight Velocimetry (TFV), Laser Doppler Velocimetry (LDV), Continous Wave Doppler LIDARs and Pulsed Doppler LIDARs. In Sect. (1.3.2) it is discussed the the Pulsed Doppler LIDARs, because they are the most successful and practical devices [48].

- *Raman LIDARs:* This class exploits an inelastic scattering process called Raman scattering, which involves the excitation of vibrational-rotational energy levels of molecules resulting in a molecule-related wavelength (red) shift of the back-scattered signal with respect to the incoming radiation. The specificity of the frequency shift allows to identify univocally a vast variety of atmospheric specimens. The main drawback of this solution is related to the typically low intensity of the Raman-shifted signal that limits the practical usability of this technique to high concentration targets. Another interesting feature of Raman LIDARs, is that the temperature of the atmosphere can be remotely measured through Raman scattering. Indeed, the population of the molecules vibrational and rotational levels depends on the temperature according to the Boltzmann's distribution law.

Differential-Absorption LIDARs (DiAL), use two wavelengths to identify atmospheric gases with high sensitivity. The use of two wavelengths, allow to acquire more information. E.g., if the differential absorption cross-section is known, then the gases concentration can be easily determined. This technique can be succesfully employed to measure concentration of chemical substances such as O_3, NO_2, NO, CH_4, NH_4 and HCl [48].

- *Brillouin LIDARs:* This kind of inelastic scattering LIDARs rely on the light third-order nonlinear interaction with the medium, involving acoustic phonons. As for Raman scattering the light scattered in this process is less energetic (Stokes process) or more energetic (anti-Stokes process), depending on the direction of the energy exchange between radiation photons and medium phonons. For different incident optical power the gain related to back-scattering can drastically change due to the substantial phonon contribute from the medium. Exploiting Brillouin scattering it is possible to measure, for instance, the temperature of oceans and the speed of sound in water [49].
- *Fluerescence LIDARs:* They rely on the absorption of LIDAR signal photons with energy tuned to match the bandgap of the target molecules, typically dispersed in the high layers of the atmosphere. The fluorescence signal at longer wavelength is then collected by the receiver. The strong cross section of metallic molecules and ions allows to easily identify also small target concentrations.

Elastic back-scattering LIDARs are widely applied in atmospheric analysis. In the following Sect. (1.2), it is described the working mechanism.

1.2 Atmospheric LIDAR working principle

The emitter is typically a high power DPSS laser source responsible of the illumination of the target. The light generated is usually a light pulse, which is directed towards the target with a proper optical systems (e.g, telescopes and steering mirrors). As the light hits the target, part of the signal is redirected back to the source by means of elastic scattering. The time required to reach the target and to return to the source is known as Time of Flight (ToF).

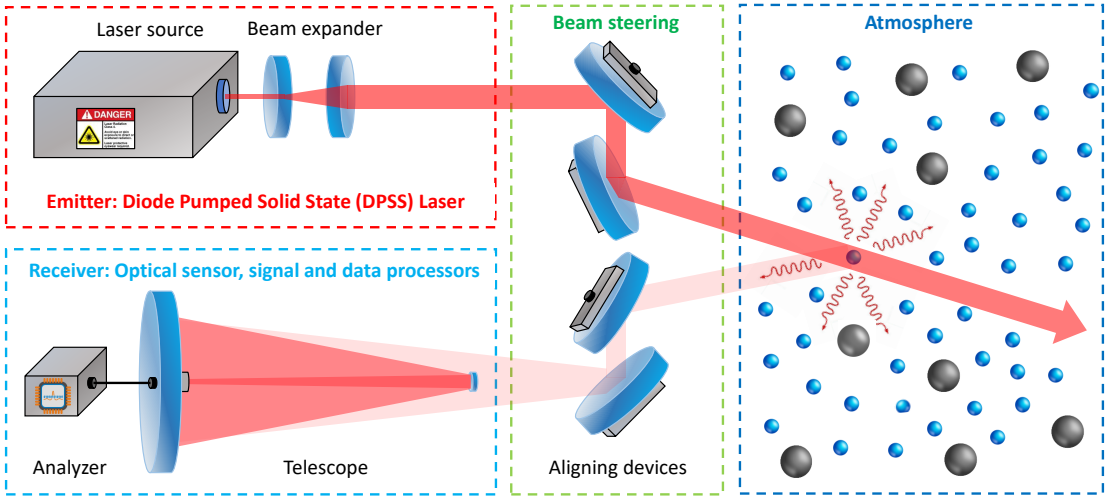

Figure 1.2: *Atmospheric LIDAR working principle*

If the speed of light in the medium is known, the ToF measurement permits to determine with a precision that depends also on the light pulse duration, the distance between the source and the target. If the effective refractive index of the atmosphere is perfectly modelled and no distortion of the returning waveform is taken into account, the target ranging resolution (spatial resolution on the light propagation axis) is equal to $\Delta r = c\tau/2$. The quantity r is the distance between the LIDAR and the target. The fraction $c\tau/2$ indicates the scattering volume. Thus a laser probe with $\tau = 1$ ns pulse duration traduces theoretically into 0.3 m ranging accuracy in the vacuum. The achievable resolution can be significantly lower than the theoretical one, considering the LIDAR movements, imprecise modelling of propagation through the medium due to atmosphere inhomogeneities and perturbations, waveform distortions on the returning signal. All these source of errors can be reduced employing a series of techniques. Tracker can be placed on LIDAR to compensate perturbation and motion for accurate range finding. A better modelling with the aid of precise data collected from ground sensor, e.g, humidity and pressure, can lead to effective modelling of the refractive index at the working wavelength. Finally, for what concerns waveform distortions, post-receiver processors can minimize propagation error and improve discrimination.

Pulse repetition rate spanning from few to hundreds of shots per seconds are typically sufficient and signals can be averaged over time intervals up to minutes in order to reduce the amount of data to be stored. The output beam divergence, thanks to the the use of beam expanders, is typically of the order of 100 μrad. A telescope is also used on the receiver side to enhance collection of incoming photons from the target, as illustrated in Fig. (1.2). The telescope field of view can be chosen as low as a few hundreds µrad by means of a field stopper located in the focal plane, allowing an efficient reduction of the background light coming from the atmosphere. After the receiver telescope, usually it is positioned an optical spectrum analyser, which selects specific wavelengths or polarization states from the collected light. Some examples of analysing elements are grating spectrometers, interferometers and atomic-vapor filters. In the final stage, signal detection is achieved with photomultiplier tubes (PMTs) or photodiodes. PMTs or avalanche photodiodes (APDs) operated in Geiger mode are preferably employed in case of weak incoming signal. On the contrary for strong incoming signal, analogic recording is preferred [48].

LIDAR system can be design in first hand starting by the expression of the detected signal power [48]:

$$P(r, \lambda) = KG(r, \lambda)T(r, \lambda)\beta(r, \lambda) \tag{1.1}$$

K measures the LIDAR system performance through Eq. (1.2), $G(r, \lambda)$ describes the geometric disposition of transmitter and receiver optics, $T(r, \lambda)$ is the transmittivity relative to the light path, $\beta(r, \lambda)$ is the back-scattered coefficient, r and λ are respectively the distance from the target and the wavelength of the signal involved in the measurement. Part of the equation is known from the designer, indeed K and G can be quantified experimentally. On the contrary, T and β are uncertain parameters, depending on the environment and the target specific characteristics. From Eq. (1.1) it is possible to derive the required emitter energy, enabling to outline the DPSS laser source specifications.

Expanding the previous terms, we have:

$$K = \eta P_0 A \frac{c\tau}{2} \tag{1.2}$$

where η indicates the system overall efficiency, P_0 is the pulse peak power, A is the area of the receiver, τ is the pulse duration and c is the speed of light in vacuum. Thus, the term $c\tau/2$ is the effective spatial pulse length from which back-scattering occurs. Eq. (1.2) shows how to maximize K and consequently the detected power P. The straightforward optimization strategy is to increase, if possible, pulse energy, receiver area and system efficiency. However, the increase of pulse energy can lead to laser safety issues and a larger receiver area can cause a worst frequency response. System efficiency also presents intrinsic trade-offs. Therefore, numerous compromises have to be taken into account to entirely design a LIDAR system.

The equation defining G is:

$$G(r) = \frac{O(r)}{r^2} \tag{1.3}$$

$O(r)$ is called the "laser beam receiver field of view overlap function". It depends on all the geometric features of the LIDAR system, such as: beam diameter and divergence, optics focal lengths and sizes, optical axes of the transmitter and receiver. The $O(r)$ function vanishes approaching the LIDAR and it is maximized, i.e. it reaches the unity, when the beam is perfectly imaged on the receiver detector.

The transmission coefficient T is give by the following equation:

$$T(r,\lambda) = \exp\left(-2\int_0^r \alpha(x,\lambda)dx\right) \tag{1.4}$$

Function T takes into account the loss accumulated by the signal travelling from the instrument to the target placed at distance r and coming back. The term $\alpha(x,\lambda)$ is the overall coefficient accounting for all the losses experienced through the propagating medium. Finally, the back-scattering function $\beta(r,\lambda)$ describes the key interaction to realize with the target:

$$\beta(r,\lambda) = \beta_{par}(r,\lambda) + \beta_{mol}(r,\lambda) \tag{1.5}$$

The terms β_{par} and β_{mol} are the particles and molecules back-scattering. In case of atmospheric applications, the molecular scattering is mainly due to nitrogen and oxygen molecules and the function is strictly dependent on the gas density. The consequences of this density-dependent back-scattering are extremely variable, depending on the nature of the target and its shape. A last term to insert in detected power equation is the unwanted P_{noise} contribution due to other sources, such as sun light or artificial lights.

$$P(r,\lambda) = KG(r,\lambda)T(r,\lambda)\beta(r,\lambda) + P_{noise} \tag{1.6}$$

This noise contribution must be accurately evaluated in order to avoid possible blinding of the receiver. Wavelengths filters and polarizers, as well as an estimation of background noise, can contribute to increase the Signal-to-Noise Ratio (SNR). The evaluation and subtraction of the background noise can be accomplished using data coming from region beyond the target or using the received signal in the time interval preceding the laser pulse emission.

1.3 LIDARs based on narrow bandwidth laser emitter

Narrow bandwidth LIDARs are extremely interesting and powerful remote sensing tools, thanks to several peculiar features. Firstly, they offer the possibility to obtain very high selectivity for the desired light-target interaction. Furthermore, and even more interestingly, in particular for atmospheric sensing applications, narrow bandwidth LIDARs offer the possibility to easily identify the target and simultaneously monitor its motion. To this class of LIDARs belong both HSRL and CDL, which both exploit the Doppler frequency broadening and shift induced on the spectrum of the back-scattered signal to enhance target data acquisition. Indeed, in the atmosphere, the back-scattered light is subject to two different alteration: one is due to molecules thermal motion, the other to particulate motion. By observing the returning spectrum, it is possible to easily discriminate the spikes related to aerosol particles scattering on top of the broader frequency distribution due to molecules scattering [50, 48], as it is shown in Fig. (1.3).

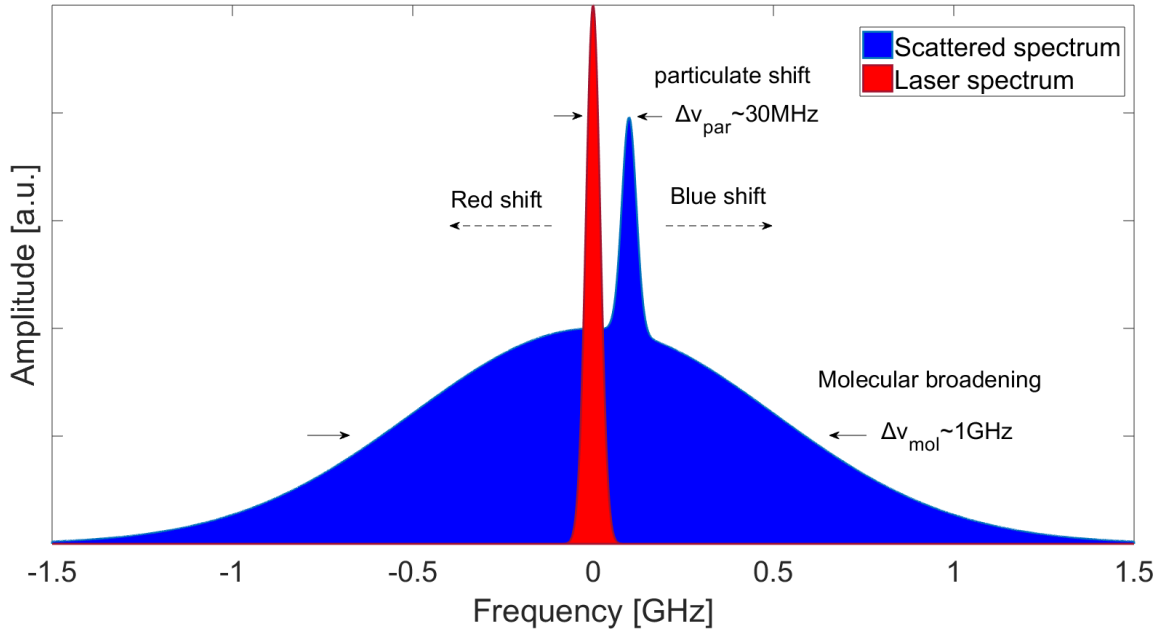

Figure 1.3: *Doppler effects on the laser spectrum. Molecular scattering is due to Cabannes-Brillouin scattering, whereas aerosol particulates scattering is related to Mie scattering*

To realize any measurement on the particulate frequency shift, the laser linewidth must be narrower than the expected shift. This happens because the shift is accompanied by a broadening effect that depends on the aerosol properties and motion homogeneity. In particular, we can identify three main contributions:

- *Molecular broadening:* molecules are subjected to Brownian motion in accordance with kinectic theory of gases related to temperature. The speed of molecoles is typically $v_{mol} \sim 300$ m/s, which means a spectral braedening of ~ 1 GHz order of magnitude.
- *Aerosol particulate shift:* for several aerosol particles moving homogeneously, the Doppler effect leads to a shift to higher frequency (blue shift) or lower frequency (red

shift). For wind speed ($v_{par} \sim 10$ m/s) the Doppler shift can be of $\Delta\nu_{par} \sim 30$ MHz, in case of turbolence ($v_{par} \sim 1$ m/s) then the shift is only $\Delta\nu_{par} \sim 3$ MHz.

- *Aerosol particulate broadening:* the Doppler shift is caused by the same agent as before, the aerosol particles, but an amount of disorder must be taken into account, leading to a broadening effect also in this case. The scattering volume can have an homogeneous aerosol motion, which causes no appreciable broadening. On the contrary, if inhomogeneous motion is present inside the investigated region, spectral broadening is observed. In this case, useful informations can be still extracted, by comparing the surrounding spatial regions to the one acquired.

If the spectral purity of the LIDAR laser emitter source is high enough, then it is possible to effectively discriminate the above mentioned contributions in the spectrum of the back-scattered radiation.

1.3.1 HSRL: High Spectral Resolution LIDAR

The master equation that must be solved to identify, for example, the concentration of a given substance in the atmosphere, is Eq. (1.6). Unfortunately to solve Eq. (1.6), six unknown variables must be quantified for each distance r, at a chosen operative wavelength λ. The unknown coefficients are the sum of the following components: the extinction coefficient $\alpha(r, \lambda)$ and the back-scattering coefficient $\beta(r, \lambda)$. Luckily, the available knowledge of physics of the atmosphere permits to reduce the unknown coefficients from six to only two. The first consideration regards β_{mol}, which is proportional to the medium density, according to Rayleigh theory. Therefore, it is possible to quantify this coefficient on the basis of a measurement of ground atmospheric pressure and temperature. Consequently, also $\alpha_{mol,sca}$ which is derived by β_{mol} by means of geometric considerations, can be estimated. Moreover, $\alpha_{mol,abs}$ is usually negligible, except in presence of high absorbent substances at operative wavelength, an event that can be avoided, for instance, by properly selecting the working wavelength of the emitter. After all these considerations, only two unknown coefficients are remaining, namely $\alpha_{aer} = \alpha_{aer,abs} + \alpha_{aer,sca}$ and β_{aer}. If the laser has a narrow enough bandwidth, then it is possible to write two equations, one for molecules and one for aerosol, instead of only Eq. (1.6), thus allowing to solve two equation with two unknowns, for a chosen wavelength. The two equations are [48]:

$$\begin{cases} P_{mol}(r) = K_{mol} \frac{O(r)}{r^2} \beta_{mol}(r) exp\left(-2 \int_0^r \alpha(x) dx\right) \\ P_{aer}(r) = K_{aer} \frac{O(r)}{r^2} \beta_{aer}(r) exp\left(-2 \int_0^r \alpha(x) dx\right) \end{cases} \tag{1.7}$$

K_{mol} and K_{aer} contain all distance-independent variables, while the term α is given by:

$$\alpha = \alpha_{mol,abs} + \alpha_{aer,abs} + \alpha_{mol,sca} + \alpha_{aer,sca} \tag{1.8}$$

HSRL requires, in addition, narrow bandwidth filters, used to enhance SNR and to discriminate between signals. Typical devices chosen for this purpose are Fabry-Perot interferometers and atomic and molecular absorption filters. Narrower laser linewdith (<100 MHz)

relaxes the necessity of spectral filters, driving photonics engineers to look for novel laser system able to achieve appropriate laser spectrum to simplify HSRL design and reduce costs.

1.3.2 CDL: Coherent Doppler LIDAR

To measure wind velocity, the Doppler shift or broadening can be measured with respect to the LIDAR line of sight, in order to recover the speed of particles. The relevant component of detected power is:

$$P_{aer}(r, \lambda + \Delta\lambda_{Dop}(v_{aer})) = K_{aer}\frac{O(r)}{r^2}\beta_{aer}(r,\lambda)exp\left(-2\int_0^r \alpha(x,\lambda)dx\right) \tag{1.9}$$

$\Delta\lambda_{Dop}$ is the wavelength shift due to aerosol particulate velocity v_{aer} along LIDAR line of sight. Recalling that $\nu = c/n\lambda$, where n is the refractive index of the medium, then the detected power can be recast as $P_{aer}(r, \nu_{det})$, where ν_{det} is the detected central frequency. The frequency shift $\Delta\nu_{Dop}$ done to the emitter frequency ν_0 is equal:

$$\nu_{det} = \frac{(c \pm v_{aer})}{(c \pm v_{source})}\nu_0 \approx \left(1 + \frac{\Delta v}{c}\right)\nu_0 \tag{1.10}$$

v_{aer}, v_{source} are respectively the aerosol, LIDAR velocities and Δv is the speed difference.

The signal collected is mixed with the local oscillator signal (heterodyne detection), allowing to generate a beat frequency, which is subsequently filtered by a low pass filter, then sampled and finally demodulated. Thanks to the speed of aerosol particle, the two light frequencies (laser and back-scattered frequencies) are similar enough that their difference or beat frequency produced by the detector is in the radio band that can be conveniently processed by standard electronics. The goal of the system is to traduce the beat frequency into a velocity.

$$P_{aer}(\nu_{det}) \propto [E_{det}\cos(2\pi\nu_{det}t + \phi)]^2 \tag{1.11}$$

$$P_{lo}(\nu) \propto [E_{lo}\cos(2\pi\nu_{lo}t)]^2 \tag{1.12}$$

where P_{aer}, E_{det}, ν_{det} and P_{lo}, E_{lo}, ν_{lo} are respectively the detected and local oscillator power, electric field amplitude and optical radiation frequency; ϕ is the phase of returning signal. Mixing the two signals lead to the folliwng equation:

$$P_{mix} \propto [E_{lo}\cos(2\pi\nu t) + E_{det}\cos(2\pi\nu_{det}t + \phi)]^2 \tag{1.13}$$

$$P_{mix} \propto \frac{1}{2}E_{lo}^2 + \frac{1}{2}E_{det}^2 + 2E_{lo}E_{det}\cos(2\pi\nu_{det}t + \phi)\cos(2\pi\nu_{lo}t) \tag{1.14}$$

The first and second term are non-oscillating contributions. Information is carried by the third oscillating term of Eq. (1.14), which has sum and difference frequencies of the original frequencies. Sum frequencies is too high for electronics (THz range), then only frequencies

difference (MHz range) is exploited in heterodyne detection. The useful induced current in the receiver derived by expression Eq. (1.14) is [48]:

$$i_{det} = \rho\sqrt{2P_{lo}P(r,\lambda)}\cos\left[2\pi(\nu_{lo} - (\nu_0 + \Delta\nu_{Dop})\right] \tag{1.15}$$

where ρ is the detector sensitivity, P_{lo} and ν_{lo} are the power and the reference frequency of the local oscillator employed for the heterodyne detection. It can be used only one laser oscillator, splitting the emitter laser output. $P(x,\lambda)$ and $\nu_0 + \Delta\nu_{Dop}$ are the power and the frequency of the backscattered radiation. It is clearly from Eq. (1.15) that the beating signal can be boosted by using a stronger local oscillator. The main advantages of the heterodyne detection technique are the high tolerance of background light and the independence from temperature and system components properties [48]. It is also clear that a Doppler LIDAR presents a greater number of components compared to conventional LIDAR as illustrated in Fig. (1.4). An other possible detection technique for Doppler LIDARs is the Direct Detection, which exploits optical filters, e.g. etalons [48].

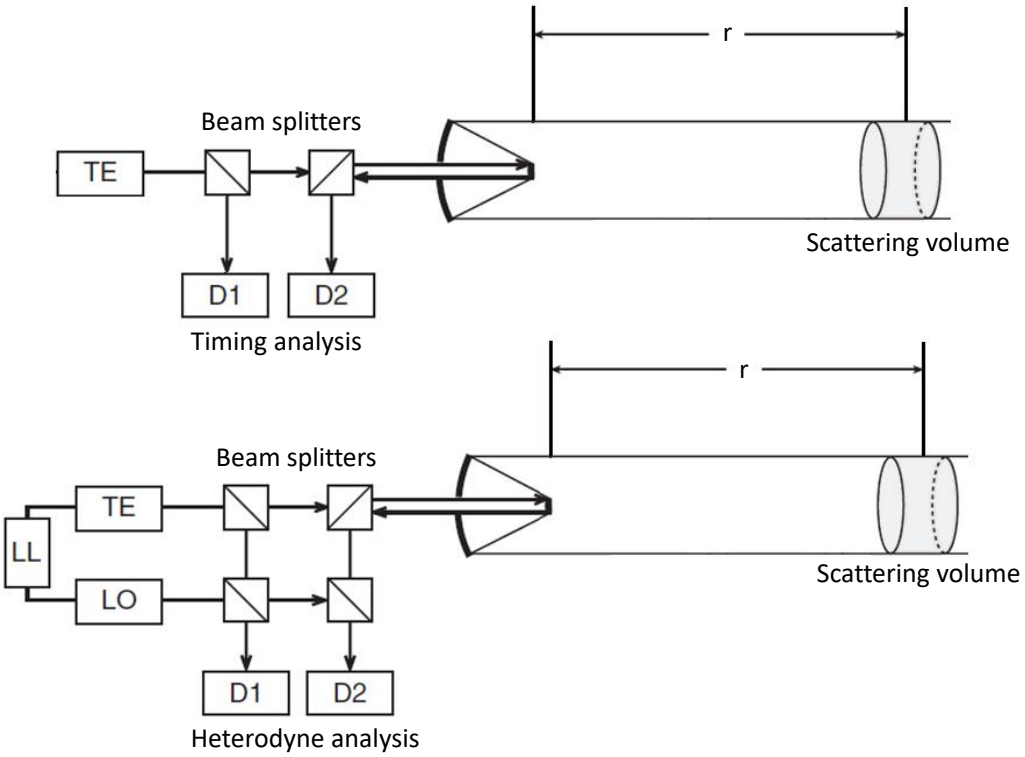

Figure 1.4: *Conventional LIDAR and heterodyne detection doppler LIDAR setups: TE is the laser emitter, LL is the locking loop, LO the local oscillator, D1 and D2 are the detectors. The quantity r is the range between the system and the target.*

1.4 LIDAR emitter requirements

LIDAR laser emitters can differ significantly depending on the applications. Pulse energy, spatial, spectral qualities and repetition rates are the typical quantities used to address a system. In Tab. (1.1) it is possible to compare how laser emitters can require drastically diversified laser pulses characteristics.

LIDAR Application	Pulse energy	Pulse duration	Wavelength region	Operational distance	Repetition rate
Automotive	<1 μJ	<1 ns	905,1550 nm	0.1-100 m	5-250 kHz
Volcanic emission	4 μJ	1 ns	355,532,1064 nm	6 km	1 kHz
Forest canopy	<1 μJ	5 ns	1538,1064 nm	100 m	1-5 kHz
Wind motion	100 μJ	50 ns	1538,1064 nm	60-100 m	15 kHz
Airborne particles	100 mJ	10 ns	532,1064 nm	40-100 km	20-100 Hz
Vegetation map	<100 μJ	1 ns	600,700,1064 nm	1 km	1-100 kHz

Table 1.1: *Examples of laser pulses characteristics for different LIDAR applications.*

1.5 DPSS Single Longitudinal Mode Laser

In the previous sections we pointed out the necessity of narrow bandwidth laser sources. The DPSS technology enables to achieve high energies laser pulses generation with specific performances, usually relying on the Master Oscillator Power Amplifier (MOPA) architecture. DPSS lasers have typically long lifespan of thousands hours [51]. MOPA architectures are very attractive because they enable to distribute complexity among several laser stages. In order to emit the narrowest pulse spectrum, the laser oscillator has to operate in SLM regime, which is mandatory for high spectral resolution applications.

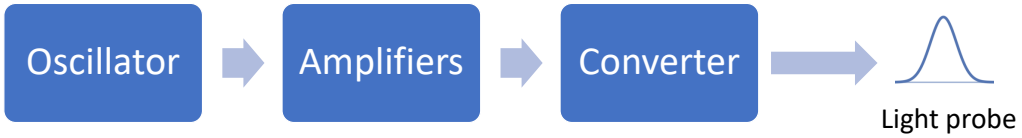

Figure 1.5: *Typical partition of a LIDAR emitter, it is not always required all three component to realize a LIDAR emitter.*

The design of a laser source operating in SLM is a challenging task, which typically requires complex architectures in order to force this regime. In a similar way, the wavelength extension is an other critical passage during the design of the emitter. In this Ph.D. thesis, DPSS laser solutions are investigated in order to design new attractive LIDAR emitter architectures, especially for HSRL and CDL systems as well nonlinear devices to extend wavelength operation. LIDAR systems do not require all the mentioned stages, illustrated in Fig (1.5). For example Doppler LIDARs operating at short distances require pulse energy of few tens or one hundereds μJ pulse energy, which is quite easily available directly out of the oscillator. In case of atmospheric HSRL systems hundreds of mJ for each pulse are typically required. This traduces in the use of one or even several amplification stages in order to reach the target pulse energy level. If wavelength conversion is also necessary to select specific physical phenomena, then the required amount of energy is increased to trigger nonlinear phenomena and to balance the nonlinear conversion inefficiencies. In this thesis it is investigated new attractive solutions for both the oscillator and converter components implementable in LIDAR emitters architectures.

Chapter 2

High spectral purity pulsed laser operation

Pulsed lasers can be obtained by means of several techniques: Q-Switching, Gain Switching and Mode Locking. The generation of pulses with spectrum bandwidths within the MHz region, which is required for LIDAR applications as explained in Sect. (2.1), imposes the use of Q-Switching or Gain Switching technologies. In this work we opted for Passive Q-Switching (PQS) technique for laser pulse generation. The PQS theory is described in Sect. (2.2) enabling to identify the most significant optical elements in order to design an optimized pulsed laser oscillator. The successive sections describe laser oscillator spectral properties (2.3), and the available techniques to access the SLM operation (2.4). Finally are discussed the seeding techniques, especially the self seeding approach exploiting the ring laser architecture in Sect. (2.5).

2.1 Optical requirements

Recalling Fourier analysis, a signal $s(t)$, which describes the time evolution of a laser pulse, can be decomposed into its spectral components by means of Fourier Transform (FT). The FT is defined as:

$$S(\nu) = \int_{-\infty}^{\infty} s(t) e^{-2\pi i t \nu} dt, \tag{2.1}$$

where $S(\nu)$ is the pulse spectrum, i the imaginary unit and ν the frequency. The spectrum $S(\nu)$ is continuous for a not-periodic signal. The function $S(\nu)$ is broader in the frequency domain for narrower signal in the original domain t and viceversa. The Inverse Fourier Transform (IFT) is:

$$s(t) = \int_{-\infty}^{\infty} S(\nu) e^{+2\pi i \nu t} d\nu \tag{2.2}$$

As first guesses, a laser pulse can be approximated by Gaussians, hyperbolic secant (Sech^2) or Lorentzian functions. All these mathematical shapes can be described by a Full Width Half Maximum (FWHM) for both the representation in the time and frequency domains. This will permit to quantify either the pulse duration Δt, or spectral width $\Delta\nu$. The FT relates Δt and

$\Delta\nu$ through the so called time-bandwidth product, which depends only on the specific shape of the pulse.

$$\Delta\nu\Delta t = K, \tag{2.3}$$

For the aforementioned mathematical shapes, we have the following values for the constant K: Gaussian pulse has $K = 0.441$, Sech^2 pulse has $K = 0.315$ and Lorentzian pulse has $K = 0.142$. In practice, more complex pulse shapes occurs. For higher accuracy, laser rate equations solutions enable to model more precisely pulses waveforms [52]. For example Q-Switching laser oscillators can exhibit asymmetric pulse shapes [53, 54]. The corresponding spetra can be practically obtained by means of Fast Fourier Transform (FFT). Nevertheless, in many situations, the Gaussian approximation is preferred since it simplifies significantly the calculations (the Gaussian is an eigenfunction of the FT), without a major loss of accuracy of the predictions.

For Doppler LIDARs and HSRLs, the FWHM pulse optical bandwidth has to be of the order few tens, or even, few MHz. Thus, laser pulses with duration of several tens of nanoseconds are required. The currently available, most successful optical technologies to access nanosecond laser pulses are Active Q-Switching (AQS), Passive Q-Switching (PQS) and Gain Switching. The laser design is strictly affected by the chosen technique, and the performance attainable in terms of available output energy, laser stability, reliability, complexity and costs, differs significantly either.

AQS and PQS rely on modulation of the resonator losses as the pulse formation mechanism. The active switches (electro-optic, acousto-optic and mechanical modulators) enable to achieve a certain amount of control on pulse-to-pulse time jitter, output energy, repetition rate and pulse duration. Typically electro-optic modulators are preferred for their limited switching time, that can be as fast as few nanoseconds or even below. The drawback of active modulators is the more complex laser design and an higher cost if compared to passive optical switches. The high voltage required by electro-optic modulators is a significant additional disadvantage, also due to the associated electronic noise.

Passive switches, i.e., Saturable Absorbers (SA) and SEmiconductor SAturable Mirrors (SESAM), allow compact, simple and robust laser design. The passive switches operate autonomously depending on the laser design realized, without any external signal/trigger. The involved inferior complexity traduces in lower costs and higher reliability. AQS and PQS systems can generate laser pulses with energies ranging from few μJ to several tens of mJ [55, 56], mostly depending on the laser repetition rate.

MOPA architectures are widely employed to amplify laser pulses produced by the oscillators to hundreds of mJ energies, permitting a simplification of the oscillator design at a cost of an increased number of stages.

Gain Switching technology is very attractive for applications requiring very high repetition rate (from hundreds of kHz, up to MHz [57]), which are not easily reachable by PQS and especially by AQS systems. Gain switching pulses are generated by quickly modulating the gain by means of the pump power. From a laser material point of view, the long fluorescence lifetime τ_f, which is a major advantage in Q-Switching regime, is a drawback in case of gain switching. For this reason, the best performance in terms of high pulse repetition rate are more easily obtained from semiconductor lasers with respect to DPSS lasers. Nevertheless, it is possible to generate nanoseconds pulses in very short and compact laser cavities. The

use of such cavities enable gain switching lasers to emit pulses with high spectral purity, easily achieving FT limited bandwidths (SLM operation). A great limitation to gain switching technology is the extremely low output pulse energy attainable, typically in the range of pJ or few nJ. Low energy pulses are not easily amplified: complex pre-amplifiers architectures and high gain amplification chains, usually prone to self-lasing and parasitic Amplified Spontaneous Emission (ASE) issues, are required. Thus, the overall system complexity is shifted to the amplification stages [58, 59, 60].

Any laser oscillator based on the aforementioned AQS, PQS or Gain Switching technologies must operate in SLM to generate transform limited laser pulses that satisfy Eq. (2.3) with the proper value of K.

A laser oscillator is composed by two fundamental components, the active medium and the cavity or resonator. The gain bandwidth of the active medium identifies the optical frequencies which can be amplified by stimulated emission. Depending on the material the gain bandwidth can differ significantly [59]. For earth ions doped crystals the gain bandwidth (FWHM) can be of few hundreds of picometers, corresponding to few hundreds of Ghz at 1 μm wavelength. Narrow gain bandwidths are consequential to ions isolation. Indeed, dopant atoms act similarly to isolated atoms thanks to the electronic shielding. On the contrary, transition metal ions doped crystals exhibit very large gain bandwidth, because of the strong interaction between electronic transitions and phonons.

The resonator has several eigenfrequencies, which are the resonant frequencies of the laser cavity.

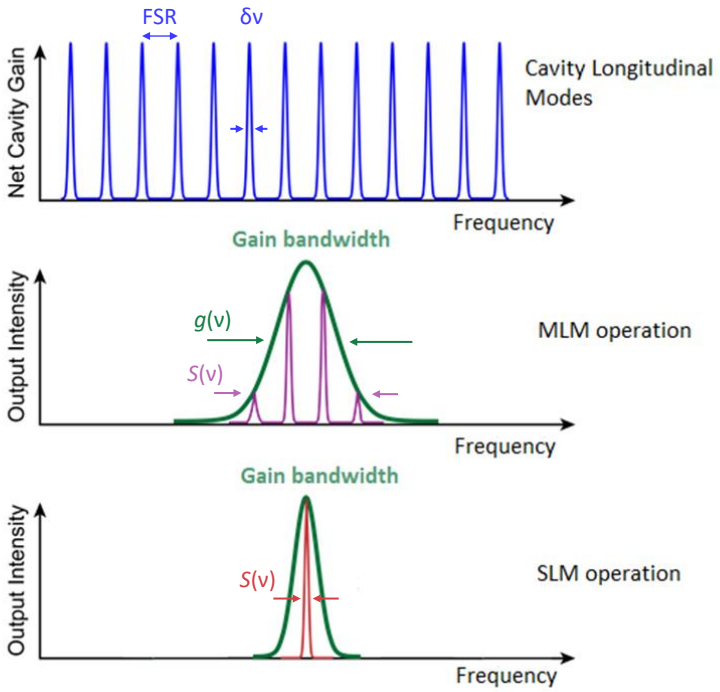

Figure 2.1: *Cavity longitudinal modes, Multi Longitudinal Mode (MLM) operation and Single Longitudinal Mode (SLM) operation.* $S(\nu)$ *is the output laser spectrum.*

These frequencies are called longitudinal modes or axial modes. Longitudinal or axial modes must not be confused with transverse modes, which describe the intensity distribution of the laser radiation in the plane orthogonal to the propagation axis.

A laser oscillator emits a laser radiation whose spectrum is the superimposition of all the modes experiencing enough gain to balance the roundtrip losses. The competition between several longitudinal modes to saturate the stored gain is usually identified as ”mode competition” or ”gain competition”. If during the oscillation build-up, one longitudinal mode is able to dominate over all the other axial modes, then the laser will operate in the SLM regime. Laser oscillators do not operate easily in SLM due to numerous factors, which will be described in detail in Sect. (2.3).

A part from the considerations about the spectrum, there are a series of side requirements to take into account to develop a LIDAR optical source, firstly the spatial beam quality. The laser beam quality is extremely important to access transform limited pulse generation and for correct imaging as well. Beam quality is usually quantified with the parameter M^2. The divergence, the Rayleigh range and the focusing power of a lens are directly affected by this parameter:

$$\Theta = M^2\theta_0, \tag{2.4}$$

$$z_R = \frac{\pi W_0^2}{M^2\lambda}, \tag{2.5}$$

$$d = M^2\frac{\lambda f}{\pi D}, \tag{2.6}$$

Where Θ is the multimode beam divergence compared to the fundamental mode beam divergence θ_0. W_0 is the optical beam waist, λ the laser wavelength, f the lens focal length, D and d the beam diameter respectively on the lens and in the focus. Then, a diffraction limited laser output is required to maximize the laser performance, i.e. $M^2 = 1$. Beam quality is usually very difficult to preserve during power scaling, especially in laser amplifiers. High power laser oscillator can maintain very low M^2 factor exploiting unstable cavities. Although, misalignment tolerance is smaller compared to stable resonators and large beam modes are achieved sacrificing the mode quality because of the Fresnel fringes [59]. The laser stability is an other critical aspect. The system must be able to deliver pulses without excessive pulse-to-pulse time and energy jitters. Mechanical and thermal perturbations should be tolerable for the laser application. PQS and AQS systems are highly vulnerable to pulse-to-pulse jitters, respectively PQS for time jitter and AQS for energy jitter. Thus, careful laser design is necessary to mitigate noise. For LIDAR applications time jitter can be bypassed relying on an optical reference instead of the electronic trigger. Although, this approach adds more complexity to the LIDAR emitter, which can be critical for airborne or spaceborne applications. Sources with low jitter allow to enhance system reliability, simplicity and enable more complex measures. Lastly, laser complexity, weight, volume, cost and reliability should be carefully evaluated in order to develop an attractive and competitive laser design. The technological challenge undertaken in this thesis is the investigation of a new SLM laser oscillator design, suitable for the generation of laser pulses of few MHz bandwidths, exploiting PQS technology.

2.2 Passive Q-Switching

Q-Switching allows to obtain short (from hundred of nanoseconds to hundred o picoseconds) pulses from a laser by modulating cavity losses (Q factor) of the laser resonator. This technique is mainly applied for the generation of nanosecond pulses of high energy and peak power with solid-state bulk lasers.

For what concerns the dynamics of the pulse generation, AQS significantly differs from PQS. In case of AQS, the generation of a Q-switched pulse can be described as follows: initially the resonator losses are at high level and the pump stores population inversion density in the gain medium. The amount of available energy is limited by spontaneous emission or ASE, and, obviously, by the maximum loss per roundtrip guaranteed by the optical switch. Then the losses are suddenly decreased to a small value through a proper Electro-Optical or Acousto-Optical device, allowing the laser radiation to build up quickly in the resonator (few roundtrips). In this case, the pulse repetition rate is under control and the pulse energy/duration will typically depend on the pump power level.

In case of PQS, the modulation of the losses is obtained through a proper saturable absorber (SA). In this case, the pulse buid-up is "slow", requiring several hundreds of roundtrips. The net gain per roundtrip in the resonator is, indeed, very small, until the bleaching of the SA is obtained.

For both techniques, the process typically starts with noise from spontaneous emission. When the gain (saturated) equals the remaining resonator losses the peak of the pulse is reached. The energy extraction occurs on a time scale depending on the photon cavity lifetime.

If the resonator is well designed, the pulse presents a symmetric temporal shape, i.e., the energy extracted after the pulse maximum is similar to the one contained in the initial part of the pulse. Because of the peculiar pulse formation mechanism, in PQS, the pulse energy and duration are almost fixed by the resonator design and SA properties, and an increase of the average pump power only influences the pulse repetition rate.

In the following paragraphs, I will present a detailed model of the PQS regime that takes into account parasitic effects taking place in the SA, such as Excited State Absorption (ESA) [61]. This is a typical parasitic loss present, e.g., in Cr:YAG, which is the most commonly used SA crystal for PQS lasers at 1 μm, and is incidentally the SA used in the PQS lasers I developed in this thesis. The model was developed to aid the design and to better interpret the experimental results obtained with PQS lasers at 1 μm in general and can be applied also to the PQS lasers developed in this thesis.

As usually occurs, the modeling starts from the laser rate-equations. The dynamics of the photon flux inside the cavity and the populations densities of the gain medium and saturable absorber, considering also ESA are:

$$\begin{cases} \dfrac{dP}{dt} = [g - q - \beta(q_0 - q) - l)]\dfrac{P}{t_R}, \\ \dfrac{dg}{dt} = -\dfrac{(g - g_0)}{\tau_L} - g\dfrac{P}{E_L}, \\ \dfrac{dq}{dt} = -\dfrac{(q - q_0)}{\tau_A} - q\dfrac{P}{E_A} \end{cases} \tag{2.7}$$

Where t_R is the roundtrip time, P is the circulating intracavity power, g and l the round-trip gain and linear losses $l = l_0 + l_p$ respectively (l_0 as the output coupling and l_p round-trip as passive linear losses). Initial unsaturated round-trip loss from passive Q-Switch is q_0, whereas g_0 is the unsaturated round-trip gain provided by the pump laser. τ_L and τ_A are the fluorescence and SA recovery time respectively.

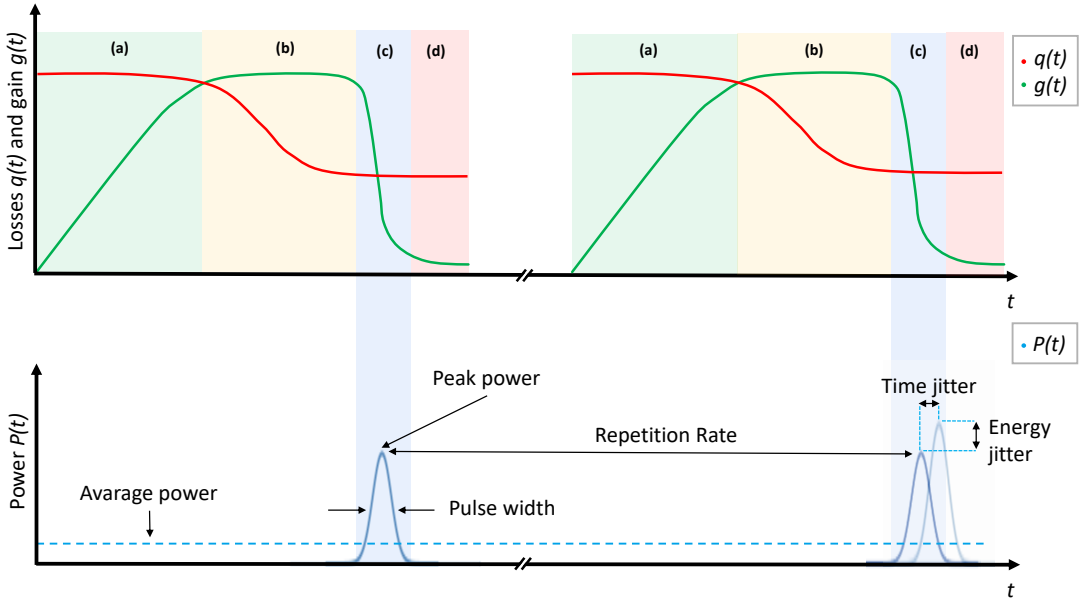

Figure 2.2: *Passive Q-Switching mechanism showing losses, gain and pulse power dynamics. Energy accumulation inside the active medium (a), intracavity losses decrease (b), pulse formation occurs (c), system recovers the saturable losses for next pulse cycle (d).*

Saturation energy for modulation loss q and gain g is:

$$E_A = \frac{h\upsilon A_A}{\S \sigma_A}, \tag{2.8}$$

$$E_L = \frac{h\upsilon A_L}{\S \sigma_L}, \tag{2.9}$$

Where σ_L and σ_A are the stimulated emission cross section for a four-level laser and the absorption cross section of saturable absorber, A_A and A_L are the modal areas in the absorber and laser medium. The coefficient §, is equal to 2 for standing wave cavities and equal to 1 for unidirectional ring cavities.
The use of Cr^{4+}:YAG as saturable absorber instead of SESAM (SEmiconductor SAturable Absorber Mirror) requires to enhance the mathematical model by including the ratio of ESA cross section of the absorber and ground state absorption cross section:

$$\beta = \frac{\sigma_E}{\sigma_A}, \tag{2.10}$$

This additional factor β allows to describe more accurately pulse energy and pulse duration for Cr^{4+}:YAG at 1 μm wavelength, leading to longer and less energetic pulses than modelling with $\beta = 0$. The gain and losses equations (second and third relation of system (2.7) evolve faster than fluorescence and loss recovery times, these terms can be considered negligible, leading to:

$$\frac{dg}{dq} = \alpha \frac{g}{q}, \tag{2.11}$$

The term α equal to the ratio between E_L and E_A. Then it can be written:

$$q = q_0 \left(\frac{g}{g_i}\right)^{\alpha}, \tag{2.12}$$

Then we can rewrite the first equation of system Eqs. (2.7) based on the above assumptions:

$$\frac{dP}{dg} = \frac{-E_L}{t_R}\left\{1 - \frac{q_0}{g}\left(\frac{g}{g_i}\right)^{\alpha} - \beta\left[\frac{q_0}{g} - \frac{q_0}{g}\left(\frac{g}{g_i}\right)^{\alpha}\right] - \frac{l}{g}\right\}, \tag{2.13}$$

Integrating Eq. (2.13) from $g_i = l + q_0$:

$$P(g) = \frac{E_L}{t_R}(g_i - g) + q_0 \frac{E_L}{g_i^{\alpha}} \frac{(g^{\alpha} - g_i^{\alpha})}{\alpha t_R}(1 - \beta) + \frac{(\beta q_0 + l)E_L}{t_R} ln\left(\frac{g}{g_i}\right), \tag{2.14}$$

Assuming $\alpha \gg 1$, which can be acceptable for Neodymium lasers (where $\alpha > 10$ typically), then the second term of Eq. (2.14) can be neglected. g_i is the initial gain, then it can be define g_f as the final gain respectively. Considering $\Delta g = g_i - g_f$ and requiring $P(g_f) = 0$ then:

$$\Delta g + (l + \beta q_0) \ln\left[\frac{l + q_0 - \Delta g}{l + q_0}\right] = 0, \tag{2.15}$$

An asymptotic solution exists for Δg relying on numerical or graphical arguments, in the limit of $l/q_0 \to \infty$.
Furthermore for $l/q_0 \sim 1$ the error is only $\sim 15\%$ and this condition corresponds to optimum output coupling. The asymptotic solution can be derived by Eq. (2.15):

$$x + (\zeta + \beta) ln\left[\frac{1 + y - x}{1 + y}\right] = 0, \tag{2.16}$$

$$x = \frac{\Delta g}{q_0} \quad ; \quad \zeta = \frac{l}{q_0} \tag{2.17}$$

Expanding the logarithm term in Eq. (2.15) to the second order:

$$\Delta g = 2q_0(1 - \beta), \tag{2.18}$$

Then energy, repetition rate and, most importantly, pulse duration can be forecast, allowing to design the PQS for the desired pulse properties. The output energy is calculated as the useful extracted fraction of stored energy $E_s = E_L g$:

$$E_0 = -\Delta E_s \frac{l_0}{l_0 + l_p}, \tag{2.19}$$

$$E_0 = E_L 2q_0(1-\beta)\frac{l_0}{l_0 + l_p}, \tag{2.20}$$

Eq. (2.16) indicates the maximum possible energy extracted in the asymptotic condition. Numerical solution allows to deduce a correction factor $\eta(\zeta)$, allowing to better describe the gain depletion for $\zeta < \infty$. Then it is possible to write a more accurate value for the output pulse energy.

$$E_0^{'} = \eta(\zeta)E_0, \tag{2.21}$$

For the pulse duration a rectangular pulse shape can be initially assumed $\tau = E_0/P_0$, recalling that the peak power is reached for $g = l + \beta q_0$, then using Eqs. (2.14) and (2.20):

$$\tau_p = \frac{E_L 2q_0(l_0/l)(1-\beta)}{(E_l/t_R)[q_0(1-\beta) + (l+\beta q_0)ln((l+\beta q_0)/(l+q_0))]l_0}, \tag{2.22}$$

The pulse duration can be rewritten for the asymptotic solution:

$$\tau_p = \frac{2ut_R(1-\beta)}{q_0(1-\beta) + l(1+\beta u)ln((1+\beta u)/(1+u))}, \tag{2.23}$$

where:

$$u = \frac{1}{\zeta} = \frac{q_0}{l} \tag{2.24}$$

The resulting asymptotic pulse width (FWHM) is

$$\tau_p = \frac{4t_R}{q_0(1-\beta)} \tag{2.25}$$

Sech^2 pulse shape is an accurate an realistic assumption. Hence, the numerical coefficient in the previous equation can be refined, assuming the same pulse energy and peak power, which are the results from rate equations:

$$\int_{-\infty}^{\infty} P_0 sech^2(t/T)dt = P_0\tau \tag{2.26}$$

Thus, the FWHM for Sech^2 pulse shape is defined as

$$sech^2(\tau_p^{(sech)}/T) = \frac{1}{2}, \tag{2.27}$$

Then $\tau_p^{(sech)} = 0.88\tau_p$, which leads to the factor 3.52:

$$\tau_p^{(sech)} = \frac{3.52t_R}{q_0(1-\beta)}, \tag{2.28}$$

As for pulse energy, pulse duration can be improved using:

$$\Psi(\zeta) = \frac{(1-\beta)}{2\zeta\left[1+\frac{(\zeta+\beta)}{1-\beta}ln(\frac{\zeta+\beta}{\zeta+1})\right]}, \tag{2.29}$$

Then it can be modelled more accurately pulse duration:

$$\tau_p^{'(sech)} = \Psi(\zeta)\tau_p^{(sech)}, \tag{2.30}$$

It must be observed that although $\eta(y)$ cause slightly energy output variation, the factor $\Psi(y)$ leads to significantly longer pulses. For $y = 1$, for example, energy is only 15% lower, whereas the pulse duration is 65% longer with respect to the asymptotic prediction. It is also worth noticing that pulse symmetry is lost for $y < 1$ and Sech^2 shape may be no longer a reliable assumption.

Repetition rate is strictly related to the pump power, for higher power and longer pumping interval more energy can be stored in the active medium leading to higher repetition rate.

$$f_{rep} = \frac{g_0 - (l + q_0)}{\Delta g \tau_p}, \tag{2.31}$$

Thus to achieve the required pulse duration and energy with Passive Q-Switching technique, the key design-parameters to work with are:

- *Cavity length:* increasing the roundtrip time, directly affects the pulse duration, without significant modification of the output energy, as long as diffraction losses in the resonator are not significantly increased Eq. (2.20). Unfortunately, when SLM selection is of concern, cavity length can not be stretched arbitrarily because of the consequent reduction of FSR, that makes SLM selection harder.

- *Saturable losses:* Greater saturable losses allows to store more energy, then allowing to increase output pulse energy Eq. (2.20). On the contrary pulse duration shortens for greater saturable losses as stated by Eq. (2.23).

The trade-off between the cavity length and saturable absorber is a crucial aspect of PQS laser design, in order to maximize energy output preserving SLM operation.

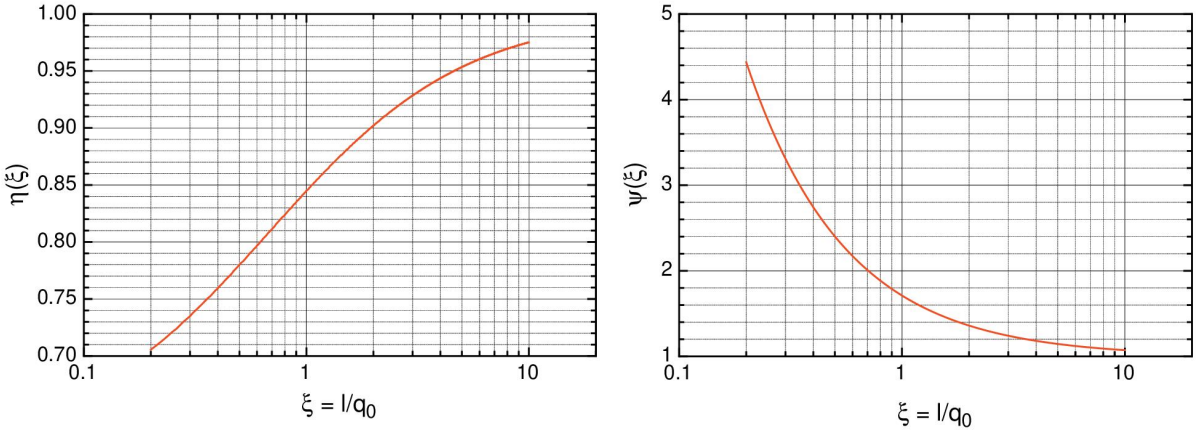

Figure 2.3: *Corrective functions $\eta(y)$ and $\Psi(y)$ for more precise PQS performance modelling*

2.3 Laser oscillator modes

The electromagnetic field has to experience constructive interference in order to be sustained in a laser cavity. The laser radiation must circulate in the resonator several roundtrips. Thus, the wave phase shift must be constant for each resonator roundtrip and consistent with the constructive interference condition. For two plane waves with the same wavelength, constructive interference can be expressed as:

$$\Delta\phi = \frac{2\pi d}{\lambda} = 2n\pi, \tag{2.32}$$

$\Delta\phi$ is the phase shift between waves, d is the distance between the two waves and λ is the wavelength. The total shift along the optical path or closed loop must equal an integral number of 2π. The quantity d is determined in practice by the cavity mirrors distances. Two fundamental classes of cavities exit, Standing Wave cavities (or linear resonators) and Travelling Wave cavities (or ring resonators). For linear resonators feedback loop is obtained by superimposing the forward and backward laser radiations, whereas ring resonator permits laser wave to propagate in a circular path. In both cases the cavity eigenfrequencies are fixed by the wave phase requirement Eq. (2.32):

$$\nu_q = q\frac{c}{\xi L}, \tag{2.33}$$

Where ν is the resonant frequency, c the light speed in the vacuum, q is an positive integer number, ξ is equal to 2 for linear resonator or to 1 for ring resonator and L is the cavity optical length. In standing wave cavities, constructive interference also requires the field amplitude to be zero at cavity end mirrors. On the contrary, travelling waves can be achieved in ring resonators due to the absence of any amplitude constrains on the cavity mirrors. The distance in frequency between two adjacent longitudinal modes is called "Free Spectral Range" (FSR)

$$\Delta\nu = FSR = \frac{c}{\xi L}, \tag{2.34}$$

To quantify the longitudinal mode FWHM linewidth, it is necessary to introduce the finesse F of the resonator, which is determined by the resonator losses.

$$F = \pi\left[2\arcsin\left(\frac{1-\sqrt{\rho}}{2\sqrt[4]{\rho}}\right)\right]^{-1} \approx \frac{2\pi}{1-\rho}, \tag{2.35}$$

The quantity ρ is the remaining power after each roundtrip, i.e. $1-\rho$ is the power loss at each roundtrip. Then, the laser linewidth can be expressed as:

$$\delta\nu = \frac{c}{\xi LF}, \tag{2.36}$$

Finally, a useful concept derived by the electronics and microwave resonators, is the Q factor. For a laser cavity, the Q factor quantifies the damping strength of the resonator oscillations. The Q factor can be defined by energy (2.37) or by resonance bandwidth (2.38).

$$Q = \nu t_r\frac{2\pi}{l}, \tag{2.37}$$

$$Q = \frac{\nu}{\delta\nu}, \tag{2.38}$$

where t_r is the roundtrip time and l are the power losses for each roundtrip. Both definitions are valid in the limit of weakly damped oscillations. If the Q factor is rapidly modified, an intense laser pulse is generated, from this the Q-Switching technique.

The laser spectral behavior can be described by comparing the above mentioned quantities to the gain function $g(\nu)$, as showed in Fig. (2.1). Laser dynamics as Continuous Wave (CW), QS and gain switching do not enable SLM operation easily. For standing wave cavities SLM operation is very difficult because of Spatial Hole Burning (SHB). This phenomenon is consequential to the spatially inhomogeneous gain saturation caused by the standing wave patterns. The unexploited energy regions stored in the active medium allows to secondary modes under the gain bandwidth to experience enough gain to balance the cavity losses, thus oscillating. Recalling the formulation of electromagnetic wave $E = E_{max}cos(\omega t - kz + \phi)$, then the intensity function of two counterpropagating waves is:

$$I(z) = I_1(z) + I_2(z) + 2\sqrt{I_1 I_2}\cos[(k_2 - k_1)z + \phi], \tag{2.39}$$

Where I_1 and I_2 are the intensities of the two waves, the $k_1 - k_2$ identifies the spatial periodicity of the interference. ϕ is the relative phases between the two E fields. Then, for a given longitudinal mode (or cavity eigenfrequency) the intensity interference spatial pattern exhibit a sinusoidal oscillation between a maximum and a minimum: [58]

$$I_{max} = |E_1 + E_2|^2 \;\; \& \;\; I_{min} = |E_1 - E_2|^2, \tag{2.40}$$

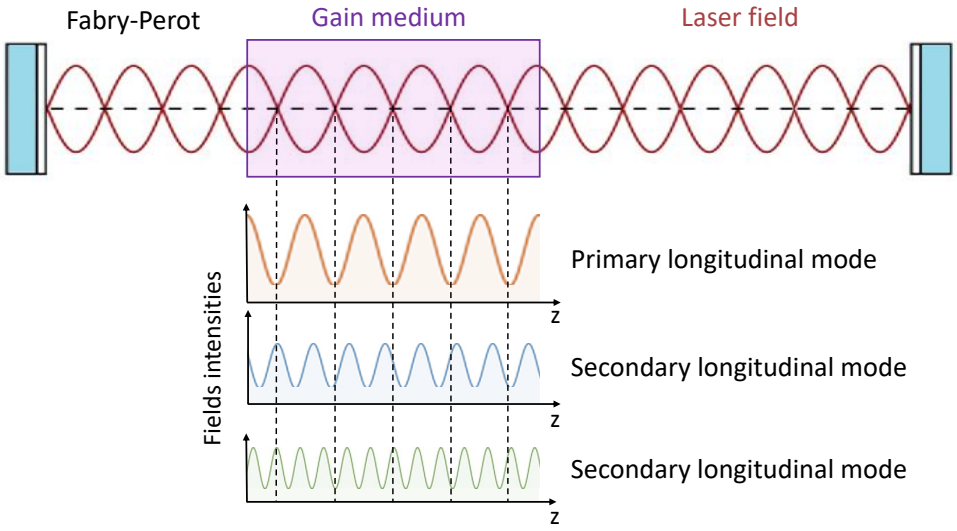

Figure 2.4: *Standing wave cavity and Spatial Hole Burning, the undepleted gain is exploited by secondary modes with suitable interference patterns.*

Ring resonators are extremely appealing to suppress SHB, because they sustain travelling waves. If unidirectional laser propagation is achieved inside a ring laser cavity, it is possible

to avoid the interference radiation wave pattern. Thus, mode competition allows one longitudinal mode to deplete all the stored energy, effectively preventing secondary modes to start oscillating. Ring laser oscillators architectures are widely employed in several single frequency lasers designs, exploiting several techniques to force unidirectional propagation. Mathematically a standing plane wave and a travelling plane wave can be described as:

$$E_{SW}(z,t) = E_{max} \sin\left(\frac{2\pi z}{\lambda} \pm \omega t\right), \tag{2.41}$$

$$E_{TW}(z,t) = E_{max} cos(\omega t - kz + \phi), \tag{2.42}$$

The transverse modes are the pattern of the laser radiation in the plane perpendicular (i.e., transverse) to the radiation's propagation direction. The transverse modes are identified by the term TEM_{mn} for Cartesian coordinates or TEM_{pl} for cylindrical coordinates. Transverse modes are particular field configurations which reproduce themselves each roundtrip. In cylindrical coordinates the radial intensity distribution with circular simmetry is given by the expression:

$$I_{pl}(r,\theta,z) = I_{max}\zeta^l [L_p^l(\zeta)]^2 (\cos^2 l\theta) exp(-\zeta), \tag{2.43}$$

Whereas for Cartesian coordinates the intensity distribution of a generic mode can be expressed by Eq. (2.44)

$$I_{m,n}(x,y,z) = I_{max}\left[H_m\left(\frac{x(2)^{1/2}}{w(z)}\right) e^{\left(\frac{-x^2}{w^2(z)}\right)}\right]^2 \times \left[H_n\left(\frac{y(2)^{1/2}}{w(z)}\right) e^{\left(\frac{-y^2}{w^2(z)}\right)}\right]^2, \tag{2.44}$$

Where $\zeta = 2r^{(2)}/w^2(z)$, z is the propagation direction, r and θ are the polar coordinates in the plane transverse to the beam propagation. The radial intensity is normalized to the Gaussian spot $w^2(z)$. The spot radius is calculated for the intensity drops to the $1/e^2$ of its peak value on the axis. L_p is the generalized Laguerre polynomial of order p and index l. The functions $H_m(s)$ and $H_n(s)$ are Hermite polynomial at a given axial position z. [59]

Transverse modes are not described individually during laser build-up, because they can coexist. This leads the generation of very complex shapes. In order to identify the beam quality, as already mentioned, it is usually introduced the parameter $M^2 \geq 1$, which quantifies the beam quality degradation. The fundamental transverse mode TEM_{00}, which has a Gaussian intensity profile, is used as beam quality reference with $M^2 = 1$. Lasers with $M^2 \simeq 1$ are referred to as "diffraction limited", enabling to maintain beam collimation along large distances and to obtain smaller beam waists in the focus of a lens. One fundamental aspect of higher order transverse modes is their influence on the longitudinal modes. The transverse modes to be fully described should have a third index, i.e., TEM_{mnq} or TEM_{plq}. Thus, the index q identifies an additional effect of higher transverse modes in the spectral domain:

$$\nu = \nu_0 + q\Delta\nu + (m+n)\sigma\nu, \tag{2.45}$$

Where the quantity $\sigma\nu$ is the transverse mode spacing:

$$\sigma\nu = -\Delta\nu\frac{\phi_G}{2\pi}, \tag{2.46}$$

The term ϕ_G indicates the Gouy phase shift. Modes with n=m=0 are called Gaussian modes or fundamental mode, whereas all other are called higher-order modes or higher-order transverse modes. The presence of the Gouy phase shift causes that the optical frequencies depend not only on the axial mode number, but also on the transverse mode indices n and m. The magnitude of that Gouy phase depends on the resonator design. Thus, to generate transform limited laser pulse, it is necessary to realize a laser oscillator operating on one longitudinal mode and with a diffraction limited beam quality (i.e., $M^2 = 1$). The diffraction limited beam output condition, i.e., $M^2 = 1$, can be more easily achieved in end-pumped laser oscillators by exciting the fundamental mode longitudinally [59]. For high power TEM_{00} laser outputs, architectures based on zig-zag active material [62] or large volume oscillators [63, 64] can be considered.

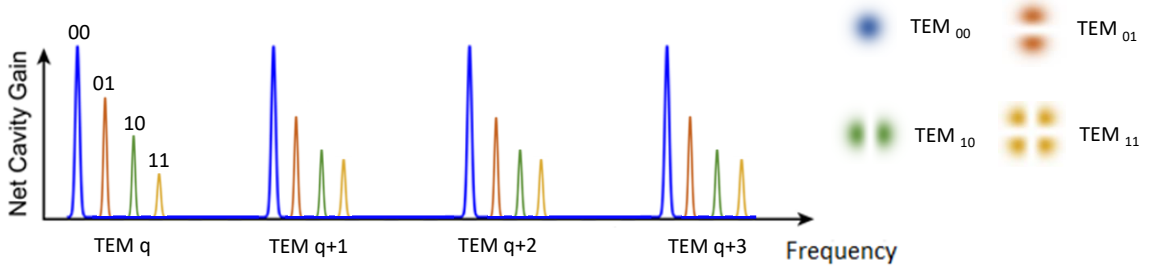

Figure 2.5: *Mode frequencies of an optical resonator. Gaussian modes and higher modes display different resonant frequencies.*

2.4 Practical techniques to select SLM operation

Numerous techniques exist to operate a laser oscillator in SLM regime, negating the effect of spatial hole burning or directly suppressing it, by avoiding inhomogeneous gain depletion. The following list describes possible techniques, that can be used either alone or in combination, depending on the laser design:

- *Compact laser oscillator:* One of the most robust approach to ensure SLM operation is to use a very short laser cavities to reach FSR comparable or possibly larger than the gain bandwidth, thus avoiding any adjacent longitudinal mode to experience significant gain [65]. Compact laser cavities are successfully used for CW low power lasers [66] and gain switching oscillators [67], which allows transform limited nanosecond pulses generation. This technique can not be easily applied to AQS and PQS architectures, because cavity length drastically affects pulse durations. Thus, microchip QS oscillator are chosen for very short pulse, usually of the order or below the nanoseconds duration [68].

- *Bragg grating mirrors:* Using special mirror with extremely sensitive wavelength depending reflectivities (0.1 nm or 0.01 nm reflective bandwidths) it is possible to select the operative longitudinal mode. Bragg grating allows to achieve high spectral and beam qualities with high energies involved [69]. Bragg grating mirrors can be also realized for several wavelengths by properly design the step of the grating, enabling to produce tunable reflectors called reflective Volume Bragg Gratings (VBG) [70]. The high performance offered by these mirrors comes at the price of a high unitary cost, especially if compared to conventional mirrors.

- *Mode Twisting technique:* this architecture uses two quarter-wave plates at both ends of the gain medium in a standing wave cavity. The linearly polarized light at the end of the laser resonator becomes circularly polarized when going through a quarter-wave plate, the axis of which is oriented at 45° to the linear polarization axis. After the gain medium, the polarization is transformed back to a linear state again. On the way back, the light becomes circularly polarized once again for the second passage in the active medium. The interference pattern for each linear polarization component is out of phase, allowing that the total optical intensity is constant along the propagation direction. This technique allows to suppress in standing wave cavities spatial hole burning. This technique has a significant downside, because it can be employed only for isotropic gain media such as Nd:YAG [71, 72, 73, 74, 75].

- *Spatial filtering:* The Exploitation of spatial discrimination to select different optical propagation paths is a possible approach to design SLM laser oscillators. Spatial discrimanation can be obtained with diffraction gratings in Littrow configuration at the cost of relatively high intracavity losses [76, 77]. Diffraction gratings are also beneficial to drastically reduce mode hopping between axial modes [78] and they enable to realize tunable laser systems. Another technique exploiting spatial filtering, is the use of oscillators based on wedge crystals [79]. Introducing a sufficient angular dispersion is possible to force SLM operation. However, laser oscillators can be spatially discriminated to enforce SLM operation only if the laser FSR is within the resolution of the spatial filter or technique.

- *Intracavity intereferometers:* A flexible approach to force SLM operation is to introduce additional phase constrains by means of intracavity interferometers such as etalons. An etalon is a transparent plate with parallel reflecting surfaces. When inserted into a laser beam, an etalon operates as an optical resonator, with periodical resonant frequencies. Etalon can be used in transmission, by applying a certain degree of tilt respect to beam propagation direction. In this case the etalon acts as a filter, exhibiting a periodic spectral resonant pattern. Transmitting etalons cause additional losses for all cavity modes out of the etalon resonance bandwidths. It is possible to tune the laser output operating on the etalon tilt angle [80, 81]. If the etalon is used with orthogonal alignment and the etalon surfaces are partially reflective, then a composite cavity is realized. Etalon used in this configuration are called Gires–Tournois Interferometers [82]. Gires–Tournois Interferometers allow to modify the spectral behaviors of the overall composite resonator, preventing the conventional periodic resonances. The use of intracavity interferometers has the disadvantage of higher cost required for high quality etalons. Another downside is represented by the losses introduced by the

intracavity interferometer and the increased risk of optical damages, due to the high intensities reached by the laser beam inside the resonator.

- *Unidirectional ring laser oscillator:* unidirectional laser propagation in a ring laser is almost completely a traveling-wave (depending on the cross path extinction ratio achieved) rather than standing-wave, thus eliminating spatial hole-burning effects. The increase of mode competition between adjacent axial modes makes possible to achieve single-frequency operation for greater pump powers. In addition the absence of spatial hole burning allows to extract more power by the gain medium during SLM operation. Ring laser allows to achieve increased cavity design flexibility and alignment insensitivity. Another useful design property is that the light wave operating in CCW or CW can be differentiated through the order of the optical elements encountered. The primary disadvantages are the additional cavity complexity and structural requirements, but expecially the gain medium is traversed only one time for each oscillator roundtrip. There are numerous technique to unbalance the CW and CCW propagation paths such as nonreciprocal optical diodes, nonplanar structure and laser seeding.

  By nonreciprocal optical diode: This technique exploits the nonreciprocal effect on the polarization state realized by a Faraday rotator. An optical isolator is composed by a nonreciporcal Faraday rotator, an Half-Wave Plate (HWP) and a Polarization dependent Beam Splitter (PBS) in order to discriminate CW and CCW propagation directions. A linearly polarized wave going in the CW direction through the system can pass through the PBS (or some other type of polarization-sensitive elements) without experiencing any attenuation or propagation path changes. On the contrary a wave going in the opposite direction, because of the net polarization rotation, will experience additional losses on each round trip. The extinction ratio achieved by this technique between CW and CCW intracavity power, called unidirectionality ratio, can reach around 30 dB and even 45 dB [83, 84]. Depending on the laser wavelength and the amount of induced polarization rotation required, the Faraday rotator can be a bulky optical element inside the cavity and it can introduce additional moderate cavity losses.

  By bounce-amplifier geometry: Suppressing the ring symmetry allows to enhance drastically the extinction ratio between the two propagation path. This approach allows to achieve extremely high value 1200:1, relying on the position and orientation of polarization sensitive optical elements. [85]

  By nonplanar architectures: Non Planar Ring Oscillator (NPRO) is a monolithic design, which is extremely stable and compact. The light propagating inside the crystal experience several internal total reflection which cause a rotation on the polarization state. This polarization rotation is balanced by the presence of a static magnetic field in order to prevent losses for the privileged laser propagation path. The undesired radiation propagating in the opposite direction experiences higher losses thus leading to its suppression. The attractiveness of this technique is the extremely reliable single frequency operation, the architecture compactness and mechanical reliability. The NPRO design allows effective frequency tuning by means of thermal control (e.g., by using peltier modules) or by means of mechanical control (e.g., by exploiting piezoelectric transducer). The disadvantages of this technology are laser radition reabsorption, which can be avoided altering the dopant concentration in the crystal structure at the cost of

higher fabrication complexity and harder quality control. Eventually the crystal geometrical layout must be developed for the desired application shifting the overall laser oscillator complexity to the crystal geometry design and realization process.[86, 87, 88]

By laser seeding: Laser seeding is an active approach to force unidirectional laser propagation in ring oscillator architectures, by means of injecting laser radiation inside the cavity during mode competition. In absence of seeding, axial modes experience an optical gain of comparable magnitude and no discrimination exist between CW and CCW propagation and MLM operation is highly likely to happen. It is possible to start gain competition with an already dominant mode amplifying with a seeding narrow bandwidth radiation close to one longitudinal mode. The seeding radiation allows to achieve unidirectional propagation and strong SLM operation by actively selecting the desired laser propagation path and longitudinal mode oscillating. The advantage of seeding technique is the absence of intracavity optical elements (no additional losses) and the high performance achievable. Laser frequency can be selected, thus tunable output can be also achieved. Active seeding with a second laser system is a rather complex technique, because it is required that the seeding radiation match the resonant frequencies of the slave oscillator. For this purpose active control is typically present in order to lock the seeder frequency to the laser slave oscillator [89]. The overall system complexity can be avoided resorting to self seeding. This technique is more sensitive to noise. Self seeding allows a far simpler design for SLM operation at the cost of less robust seeding, due to the lower power compared to a possible master laser.

Laser oscillators designs can exploit more than one of the aforementioned techniques in order to realize a reliable SLM laser systems.

2.5 Unidirectional ring lasers and Seeding techniques

Injection seeding allows to control the spectral property of the seeded (slave) laser. A moderate power signal with optimal spectral bandwidth is injected during pulsed slave laser build up time. If the injected signal is strong enough, the pulse growing from the seed will dominate and saturate the gain, preventing any other axial mode to oscillate. This is achieved in a ring cavity, which enables to suppress spatial hole burning. Then, the high power slave laser output will mimic the seed spectral properties. The seeding signal has to sufficiently amplify the target slave resonant mode for mode competition, thus some moderate mismatch of frequencies is acceptable. The frequency of the generated pulse may deviate from the seeded frequency. On the contrary in injection looking the seeding laser is locked to the slave laser resonant mode by a feedback loop. Injection looking can be achieved by several methods, e.g. using error signal to adjust the slave cavity length, minimizing the build up time or resorting to the ramp fire technique. For effective seeding, the mode of the injected signal must match the mode of the slave oscillator. The coupling coefficient between the seeding modes and the slave laser mode over a plane perpendicular to the propagation direction can be expressed:

$$c_{overlap} = \frac{\int_{-\infty}^{\infty}\int_{-\infty}^{\infty} E_1 E_2 dxdy}{\left[\int_{-\infty}^{\infty}\int_{-\infty}^{\infty} E_1 E_1 dxdy \int_{-\infty}^{\infty}\int_{-\infty}^{\infty} E_2 E_2 dxdy\right]^{1/2}}, \tag{2.47}$$

Where the electric fields E_1 and E_2 are related to Gaussian beams, which can be expressed in cylindrical coordinates:

$$E_i(r,z) = E_{max}\hat{u}\frac{w_0}{w(z)}exp\left(\frac{-r^2}{w(z)^2}\right)exp\left(-i\left(kz + k\frac{r^2}{2R(z)} - \phi_G(z)\right)\right), \tag{2.48}$$

$$I_i(r,z) = I_{max}\left(\frac{w_0}{w(z)}\right)^2 exp\left(\frac{-r^2}{w(z)^2}\right), \tag{2.49}$$

Where $\hat{u}$ is the polarization direction, r is the distance from the optical axis, z the distance from the beam focus w_0, R the wavefront curvature radius, $k = 2n\pi/\lambda$ the wave number, ϕ_G is the Gouy phase and $w(z)$ is the beam waist function, which comprises the Rayleigh range Eq. (2.5):

$$w(z) = w_0\sqrt{1 + \left(\frac{z}{z_R}\right)^2}, \tag{2.50}$$

If the two beam are not of the same dimension, a beam radii mismatch coefficient can be introduced:

$$c_{waist} = \frac{2w_{01}w_{02}}{w_{01}^2 + w_{02}^2}, \tag{2.51}$$

For equal beam radii, the coefficient is trivially equal to one. If equal beam have the same transverse positions, but a different longitudinal waist positions, then the longitudinal coefficient $c_{longitudinal}$ can be introduced.

$$|c_{longitudinal}| = \left[1 + \left(\frac{\lambda(z_1 - z_2)}{2\pi w_{01}^2}\right)^2\right]^{-1/2}, \tag{2.52}$$

Transverse coefficient $c_{transverse}$ is:

$$c_{transverse} = \frac{2w_{01}w_{02}}{w_{01}^2 + w_{02}^2}exp\left(-\frac{\Delta x^2}{w_{01}^2 + w_{02}^2}\right), \tag{2.53}$$

If the seed laser suffers from astigmatism a new coefficient has to be taken into account, i.e. the $C_{astigmatism}$.

$$c_{astigmatism} = 2\left(\frac{w_{01}^2 w_{x2}w_{y2}}{(w_{01}^2 + w_{x2}^2)(w_{01}^2 + w_{y2}^2)^{1/2}}\right), \tag{2.54}$$

The penalty for astigmaic beams is relatively small unless the astigmatism is severe. If the two beams have different propagation direction, but same waist positions (transversally and longitudinally), then the angular coefficient $c_{angular}$ can be defined as:

$$c_{angular} = \frac{2w_{01}w_{02}}{(w_{01}^2 + w_{02}^2)^{1/2}(w_{01}^2\cos^2\theta + w_{02}^2)^{1/2}}exp\left[-\frac{\pi^2 w_{01}^2 w_{02}^2 \sin^2\theta}{\lambda^2(w_{02}^2 + w_{01}^2\cos^2\theta)}\right], \tag{2.55}$$

For beam with same radii and for small of θ, the coefficient $c_{angular}$ becomes:

$$c_{angular} = exp\left[-\frac{\theta^2}{2\theta_0^2}\right], \tag{2.56}$$

where $\theta_0 = \lambda/(\pi w_{01})$ is the beam divergence. Good coupling requires to achieve a good matching between the two direction compared to the beam divergence. Typically the critical coupling parameters are the transverse and angular alignment of the injected beam in the slave laser. The seed signal has a power coupling equal to the $T_R c_{overlap}$, where T_R is the power transmission exploited to enter the slave laser. The quantity $c_{overlap}$ can be described by the product of the all mentioned coupling coefficients. The laser beam waist $w(z)$ of a ring laser resonator can be described by ABCD ray matrix method. This approach is extremely useful considering the complexity of ring resonator compared to the well known linear cavities (i.e. plano-plano, confocal, plano-concave cavities). Ring laser resonator can have several shape. ABCD matrix modelling allows to design a stable ring cavities controlling the fundamental mode TEM_{00} sustained by the resonator. The paraxial approximation is always required for ABCD matrix simulations, i.e., the involved divergence angles must stay small in order to achieve accurate modelling. A ray can be described with a vector [2x1], containing the distance from the optical axis r and the beam divergence θ. The beam propagates through an optical element described by a matrix [2x2] (ABCD), the product between the input ray and the optical component matrix returns an output ray.

$$\begin{bmatrix} r' \\ \theta' \end{bmatrix} = \begin{bmatrix} AB \\ CD \end{bmatrix} \begin{bmatrix} r \\ \theta \end{bmatrix}, \tag{2.57}$$

An entire laser oscillator can be described utilizing the right overall ABCD matrix:

$$\begin{bmatrix} A_r B_r \\ C_r D_r \end{bmatrix}_{roundtrip} = \prod_{i=1}^{k} \begin{bmatrix} A_i B_i \\ C_i D_i \end{bmatrix}, \tag{2.58}$$

From Eq. (2.58) it can be easily derived the stability of the laser oscillator, composed by k optical elements. Resonator stability is guaranteed if the following relation is true:

$$-1 < \frac{A_r + D_r}{2} < 1, \tag{2.59}$$

The second important parameter to control during seeding in addition to the spatial overlap is the spectral overlap. The seeding radiation must be tuned to the slave laser eigenfrequencies. In order to be effective, the mode amplified by the seed must extract the stored energy before any other mode grows spontaneously. If the seed pulse exactly matches the frequency of the resonan mode, it is a special case of seeding referred as injection locking. The seed electric field E_s can be compared to the slave natural electric field E_n. In one round trip the seeded electric field is altered by the following power factor:

$$E'_s = E_s[(R_{oc}l)^{1/2} exp(g_0 L_{gain}/2 + jkL_{cavity})], \tag{2.60}$$

Where P'_s is the amount of seed power after one round trip and R_{oc} is the output coupler reflectivity. In addition the seeded laser radiation is augmented by the field coupled into the resonator E_c. The time evolution of the intracavity seeded radiation is:

$$E'_{sc}(t+t_r) = E_{sc}(t)[(R_{oc}l)^{1/2}exp(g_0L_{gain}/2 + jkL_{cavity})] + E_c(t+t_r), \tag{2.61}$$

For a continous wave seeding the coupled seed field can be expressed:

$$E_{sc}(t) = E_c\frac{(exp(st)-1)}{(exp(st_r)-1)}, \tag{2.62}$$

$$s = -\frac{1}{2t_{ph}} + \frac{g_0L/2}{t_r} + j2\pi(|\nu_n - \nu_s|), \tag{2.63}$$

The quantity t_{ph} is the photon lifetime in the resonator. For a pulsed seeding, the field can be described in the following way if the pulse is short compared to the round trip time interval, i.e., interference is absent.

$$E_{sc}(t) = E_c(exp(st)), \tag{2.64}$$

Eqs. (2.62) and (2.64) describe the evolution of continuous wave and pulsed electric seeding fields within the laser resonator. Without injection seeding a laser pulse would evolve from noise (the natural electric field E_n) with a evolution time τ_e and showing a natural pulse width τ_p. Injection seeding to be successful requires the following relation to be true: [90]

$$E_s * E_s|_{t=\tau_e-\tau_p} \geq E_n * E_n|_{t=\tau_e}, \tag{2.65}$$

Eq. (2.65) indicates that the slave pulse has to deplete the stored energy before the natural time τ_e. This requirement means that the seed laser radiation must be able to anticipate enough the pulse dynamic (around the pulse duration τ_p) preventing any secondary natural mode to experience amplification, thus starting to oscillate. A stronger seeding signal will be detrimental. Tens of mJ pulse SLM laser output can be achieved by seeding power slave oscillator with CW DP laser oscillators of moderate power (few tens of mW) [91].

A particular case of seeding is the self injection seeding technique. This approach is appealing because it allows to combine unidirectional propagation and seeding at the same time in a ring resonator. A ring oscillator without any optical diodes or peculiar intracavity elements order exhibits a standing wave regime, emitting two, equally intense, separate laser beams. If one of the two laser output is redirected back into the cavity as a seed, the laser oscillator starts to operates in unidirecional propagation [92]. The clockwise and the counter clock wise traveling waves compete for the laser gain. By placing an additional mirror, one of the travelling wave grows at the expanse of the other. Then the additional mirror acts a very low amplitude, self triggered injection seeding. This is valid for homogeneously broadened active materials, for inhomoegenously broadened gain media the two travelling waves do not compete with the same frequency.

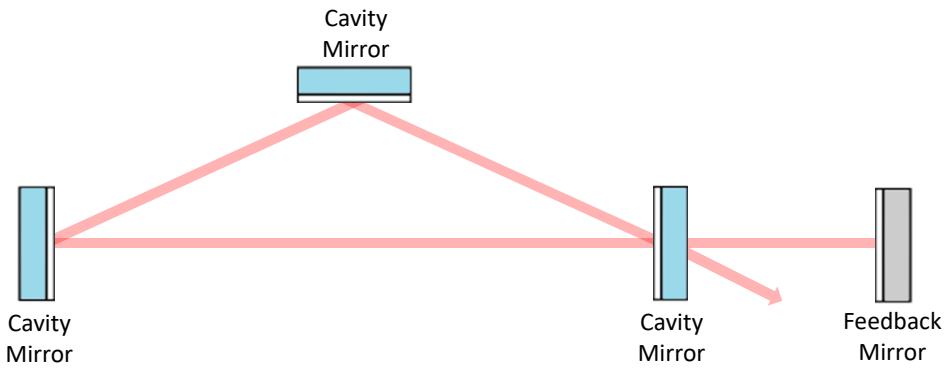

Figure 2.6: *Unidirectional ring laser architecture with external feedback mirror*

The typical extinction ratio achievable with this technique is around 100:1 [58]. It has been reported also cases with higher unidirectional ratio around 2500:1 [93]. The unidirectional extinction U ratio can be expressed as:

$$U = \frac{P_{CW}}{P_{CCW}}, \tag{2.66}$$

Self seeding is extremely attractive because of the optimal spectral overlap and the easily achievable spatially matching by means exploiting re-imaging in the feedback arm. This technique is deeply investigated in the next chapters, yielding to the Self Injection Seeding Ring Oscillator (SISRO).

Chapter 3

SISRO technology SLM investigation

Three bow-tie ring laser oscillators operated in PQS regime based on Nd:YVO_4 and Nd:YAG have been designed and characterized in terms of output energy, spatial laser beam quality, pulse duration and spectral behaviour. These systems have been realized in order to investigate the self-injection seeding technique for SLM operation, analyzing the effectiveness for suppressing spatial hole burning thus allowing the onset of one dominant axial mode.

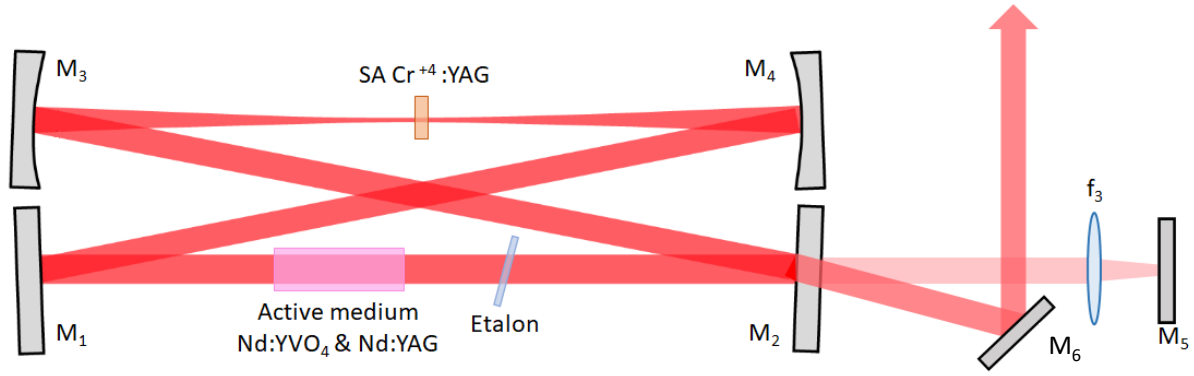

Figure 3.1: *SISRO laser design*

The oscillators realized have a "Bow-tie" layout, differing for the cavity length, mirrors curvature radius and active medium (Nd:YVO_4 or Nd:YAG). The bow-tie ring cavities layouts share the same mirror disposition: two flat mirrors M_1 and M_2 and two curved mirrors M_3 and M_4 for cavity optical stability and also to realize a beam focus in the SA material to facilitate PQS operation. Referring to Fig. (3.1), the pump mirror M_1 is a dichroic mirror with high transmittivity for pump wavelength at 808 nm and high reflectivity at the laser wavelngth of 1064 nm. The mirror M_2 is the output coupler, with reflectivity R at 1064 nm. The mirrors M_3 and M_4 are two concave, high reflective mirrors at 1064 nm, with curvature radius r_3 and r_4, respectively. The active medium, as well the etalon, are placed between M_1 and M_2, whereas the SA, a Cr^{4+}:YAG crystal, is positioned in the proximity of the resonator focus between mirrors M_3 and M_4.

Here I list the main features of the three different resonators I studied in details.

- *The first oscillator* is based on $3\times3\times8$-mm^3, 0.3%-doped, a-cut Nd:YVO_4 crystal and has a resonator length of 731 mm, which results in a $FSR = 410$ MHz. The folding angle of the mirrors is 9.6°, mirror M_2 has a reflectivity R=90%, $r_3 = r_4 = 100$ mm.

- *The second oscillator* is based on the same Nd:YVO_4 crystal, the resonator length is 452 mm ($FSR = 660$ MHz) and the folding angles are 8°. M_2 has a reflectivity R=90%, $r_3 = 100$ mm and $r_4 = 50$ mm.

- *The third oscillator* is based on a $3\times3\times12$-mm^3 0.8%-doped, Nd:YAG crystal and has a resonator length of 540 mm ($FSR = 540$ MHz). The folding angle is 7.5° and curved mirrors have curvature radii of 100 mm. The output coupler, as in the previous cases, is a partially reflective mirror with R=90%.

As already mentioned, we used an intracavity etalon (intracavity Fabry Perot interferometer) placed between the two flat mirrors M_1 and M_2. The fused silica etalon is 1 mm thick, coated with $\sim$ 50% reflectivity at 1064 nm. It acts as a low-finesse Fabry Perot filter with 103 GHz free-spectral range. As displayed in fig (3.1) the correct use of the etalon requires to tilt the filter in order to avoid optical feedback, thus preventing parasitic cavities.

3.1 Ring laser oscillators models

The design of complex cavities, such as ring oscillators, requires specialized simulation in contrast to simple linear cavities based on two reflectors. The laser stability and beam radius are described by means of ABCD matrix, allowing to determine the optimal position of the optical elements and their properties as well. For a ring architecture, exactly as it happens for standing-wave resonators, the use of curved mirrors allow to achieve cavity stability. One of the drawbacks of the bow-tie layout (3.1), is the astigmatism between the tangential and sagittal planes introduced by the tilted curved mirrors. The three bow tie laser oscillators realized are modelled and described in the following Figs. (3.2), (3.3) and (3.4). The target is to realize a strong focus inside the cavity, in order to ease the fulfilment of the second threshold condition for PQS operation [55].
The simulated cavities by means of ABCD matrix are:

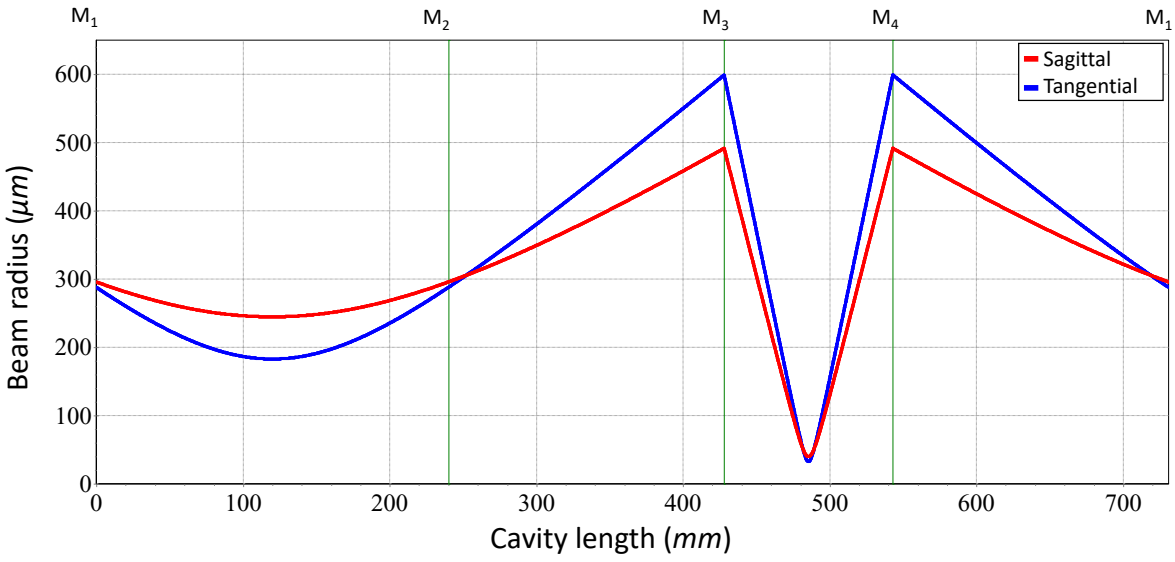

Figure 3.2: *731mm long bow-tie (FSR=410.1 MHz) ring laser oscillator ABCD modelling*

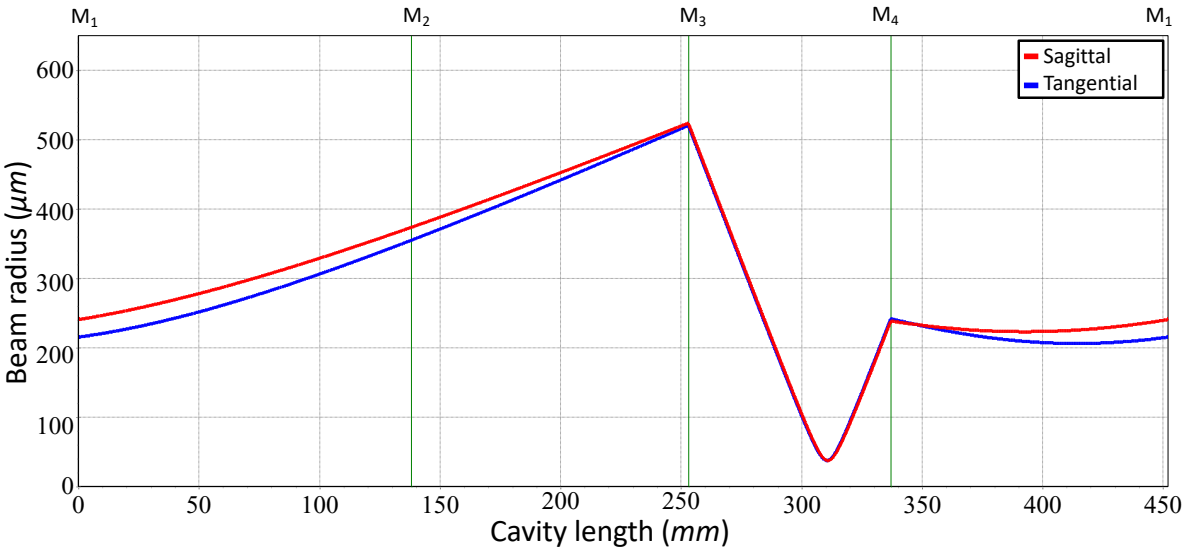

Figure 3.3: *452mm long bow-tie (FSR=663.2 MHz) ring laser oscillator ABCD modelling*

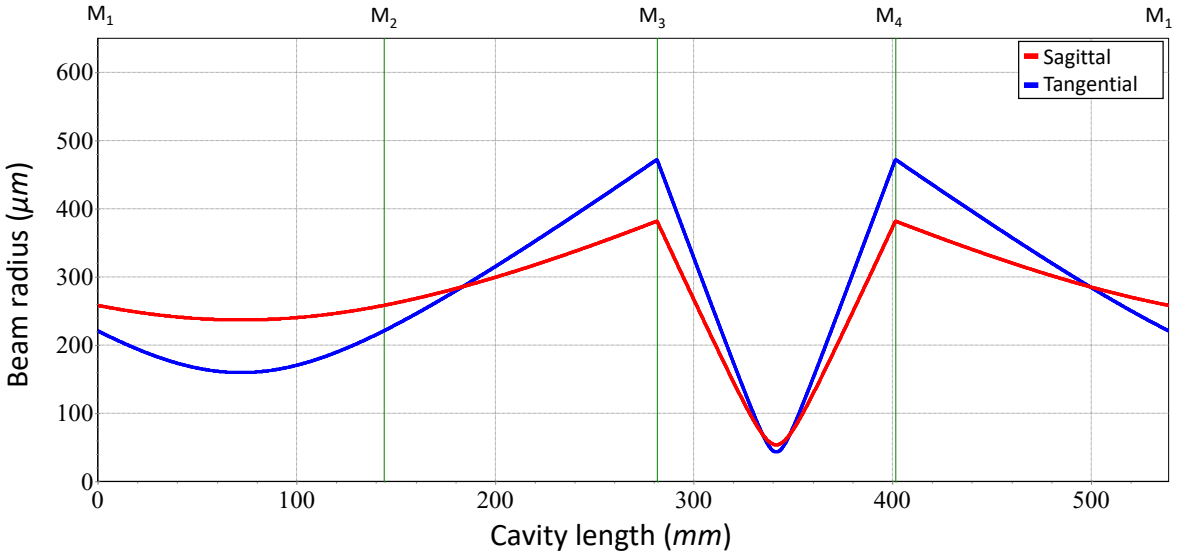

Figure 3.4: *540mm long bow-tie ring (FSR=555.1 MHz) laser oscillator ABCD modelling*

Placing the saturable absorber in the focus region enables to guarantee a PQS condition:

$$\frac{A_s}{F_{sa}} > \frac{A_l}{F_{sl}} \tag{3.1}$$

Where A_s and A_l are the cavity mode area on the SA and laser medium, F_{sa} and F_{sl} are the saturation fluence of SA and the active medium. Eq. (3.1) indicates that the saturable absorber must be saturated prior the gain medium, in order to realize a PQS laser oscillator. Condition (3.1) can be recasted as:

$$A_s \sigma_{sa} > A_l \sigma_{sl} \tag{3.2}$$

To extract higher energies, laser architecture with larger effective mode areas in the active medium should be pursued. Although, working closer to the laser instability in order to maximize energy output means higher sensitivity to misalignment and vibrations of optical components. In this work it has been privileged a moderate output energy signal, trading off pulse energy for a better pulse stability and optimized spectral property. This approach is extensively used in DPSS MOPA laser engineering, where an high quality signal is amplified to the desired power level.

3.2 Pump laser diodes

The ring oscillators I built are pumped with fiber coupled laser diodes provided by Bright Solutions s.r.l. (BFP models [94]). The wavelength emitted by BFP diodes ranges between 803 nm and 807 nm, depending on the pump current and temperature set point of the thermal control, with a spectral width of about 2 nm (FWHM). As typically occurs with this class of devices, once the temperature is fixed, there is a residual current-dependent wavelength shift. This is what should be expected from a laser diode, if no special wavelength stabilization technique is used. However, this is not an issue thanks to the relatively broad absorption spectrum of Nd:YVO_4 and Nd:YAG as well, which relaxes the pump wavelength stabilization requirements.

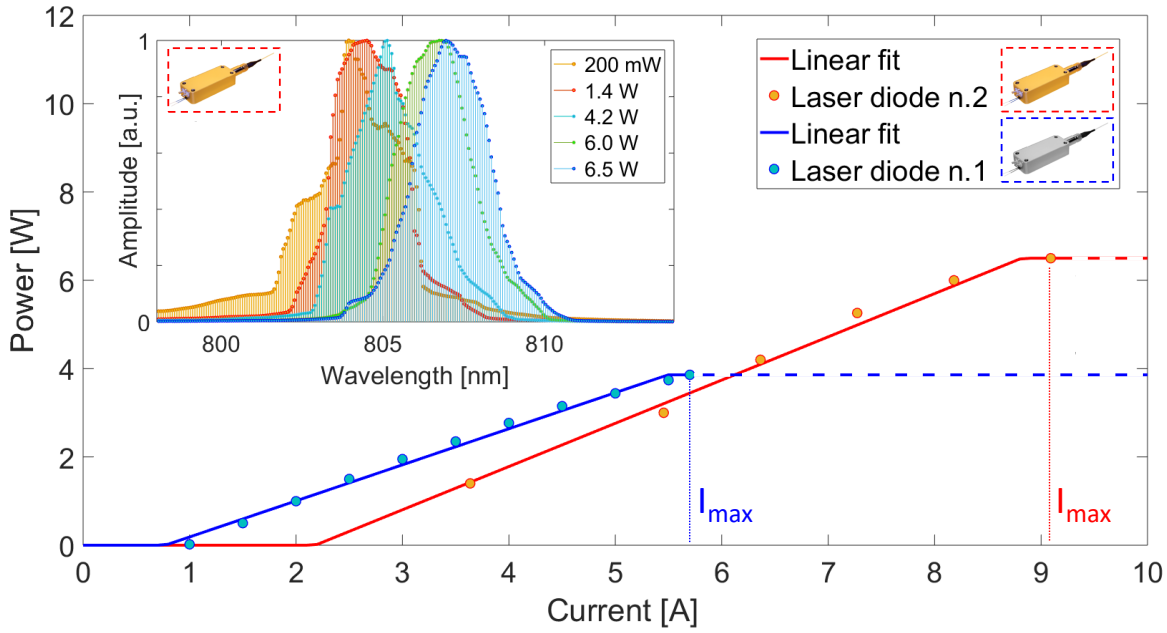

Figure 3.5: *Diodes output power characterization versus input current, inset shows the wavelength drift for different output powers.*

- *BFP Diode n°1:* This diode, employed for the 731-mm-long Nd:YVO_4 oscillator, can deliver a maximum CW (Continuous Wave) power of 4 W. The pump diode fiber has a core diameter of about 60-µm and the measured beam quality M^2 is about 20. The optimal diode temperature to maximize absorption is 32 °C.

- *BFP Diode n°2:* This diode, employed for the 540-mm-long Nd:YAG and 452-mm-long Nd:YVO_4 ring oscillators, can deliver a maximum power of 6 W. It can be driven in both CW and Quasi-CW (QCW) regime, with adjustable pulse duration and peak power. The diode laser fiber has a core diameter of about 105-µm (NA=0.22) with a $M^2 \approx 34$.

The ring oscillators are end-pumped. This approach allows to quite easily generate a close-to-diffraction-limited laser output beam. Fundamental TEM_{00} mode is selected by means of mode overlap in the gain medium. The pump beam is focused in the active medium for the entire crystal length, according to Rayleigh range condition, superimposing to the cavity laser mode. The telescope realized to fulfill this condition are respectively:

- *Pump telescope for diode n°1:* Spherical lenses with focal lengths of f_1=20 mm and f_2=150 mm are employed for the 731 mm long ring oscillator, realizing a magnification factor of 7.5. Both lenses are Anti-Reflection (AR) coated at 808 nm (Achromatic spherical lenses).

- *Pump telescope for diode n°2:* Spherical lenses with focal lengths of f_1=40 mm and f_2=150 mm are employed for the 452 mm and 540 mm long ring oscillators, resulting in a magnification factor of 3.75. Both are Anti-Reflection (AR) coated at 808 nm (Achromatic spherical lenses).

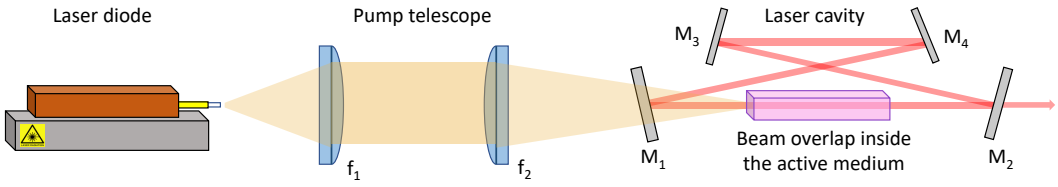

Figure 3.6: *End-Pump imaging in the active medium for SISRO architecture.*

The active medium (Nd:YAG or Nd:YVO_4) is wrapped in indium foils and inserted in a aluminium or copper case for heat dissipation. Considering the maximum power delivered to the active medium, and the overall typical optical-to-optical lasers efficiency, it was not deemed necessary any active thermal control on the gain medium.

3.3 Experimental results

The SISRO characterization started by the CW regime characterization of the 731-mm-long cavity. The laser oscillator operated with several longitudinal modes both with and without the self-injection. The external feedback mirror enforced nearly unidirectional operation, achieving an unidirectionality ratio of 99%. The use of the etalon resulted in bidirectional stable SLM operation if no self-injection was present. With careful alignment of the etalon it was possible to achievie SLM and high contrast unidirectional propagation, but this regime

was highly unstable and the laser randomly switched between the two ring directions. However, in presence of the self injection seeding, even with the purest unidirectional regime obtained in our experiments (extinction ratio close to 99%, as aforementioned), the laser ran consistently with two adjacent longitudinal modes.

The laser spectrum was measured by means of a Fabry Perot Scan interformeter (Thorlabs Inc., Model SA200) with FSR=1.5 GHz and resolution of 7.5 MHz. The use of the intracavity filter, i.e. the etalon, while enhancing the spectral properties of the laser oscillator, lowers the system power efficiency, as illustrated in fig. (3.7):

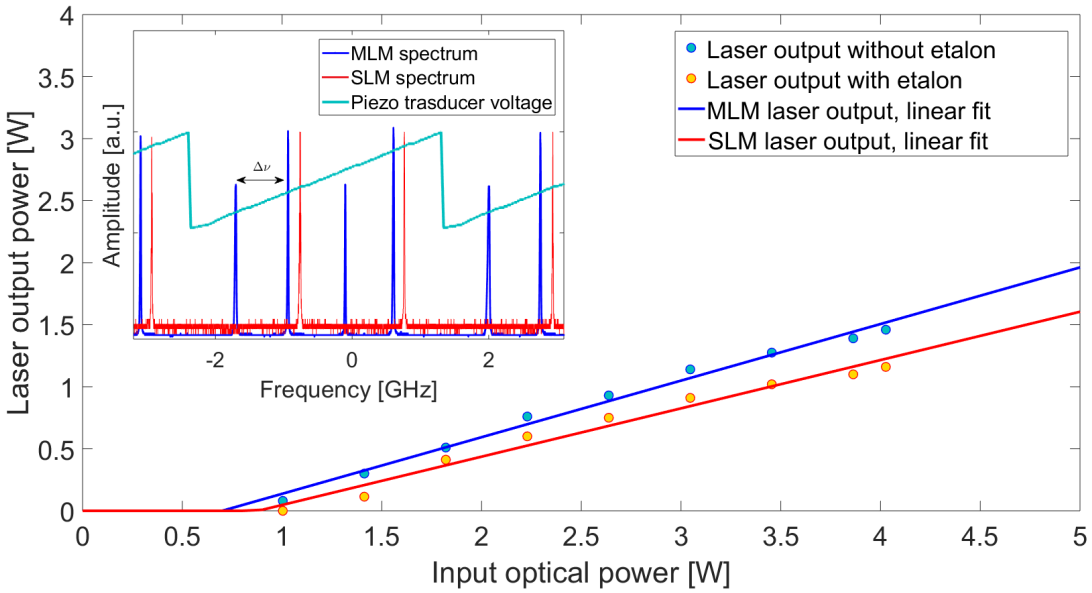

Figure 3.7: *CW (SISRO 731 mm) output power characterization versus input power, $\Delta\nu$ is the cavity Free Spectral range, i.e. 410 MHz.*

Switching to PQS regime, with the insertion of Cr^{4+}:YAG, the SISRO architecture exchange the aforementioned behaviors. In presence of Self Injection seeding, the laser oscillator is able to emit clean SLM pulses. The seeding power circulating in the low-power arm is slightly higher, 1.5% for $T_{SA} = 88\%$ and 2.7% for $T_{SA} = 79\%$ instead of only 1%. The use of SA with initial transmission of 90% and 81% allowed to generate pulses with duration of 148 ns, 96 ns and with energies of $51\ \mu$J, $37\ \mu$J respectively. If self injection seeding was not ensured, MLM operation always occurred, in particular the alignment of the etalon and the mechanical stability of the feedback mirror were fundamental to emit SLM pulses. Despite the system tends to privilege the SLM operation, mechanical perturbations, expecially on the feedback mirror, traduced in poor overlap during pulse build up time preventing SLM operation, (2.47). The etalon also required frequent tuning for SLM pulses generation on relatively large time of scale, (units to tens of seconds). This behaviour can be motivated due to the etalon placing. It was positioned after the active medium due to the cavity spatial constrains. The etalon was placed in an aluminium holder with poor thermal exchange and exposed to pump residual power transmitted through the active medium. Both the gain bandwidth and the etalon resonance bandwidth were thermally shifted, allowing SLM operation for only short amount of time intervals of tens of seconds.

The small FSR (hundreds of MHz order) allows to easily monitor the spectral purity by ob-

serving the beat modulation on the oscilloscope trace. The oscilloscope used in the laboratory has a 1.5 GHz bandwidth, allowing to detect multiple oscillating modes.

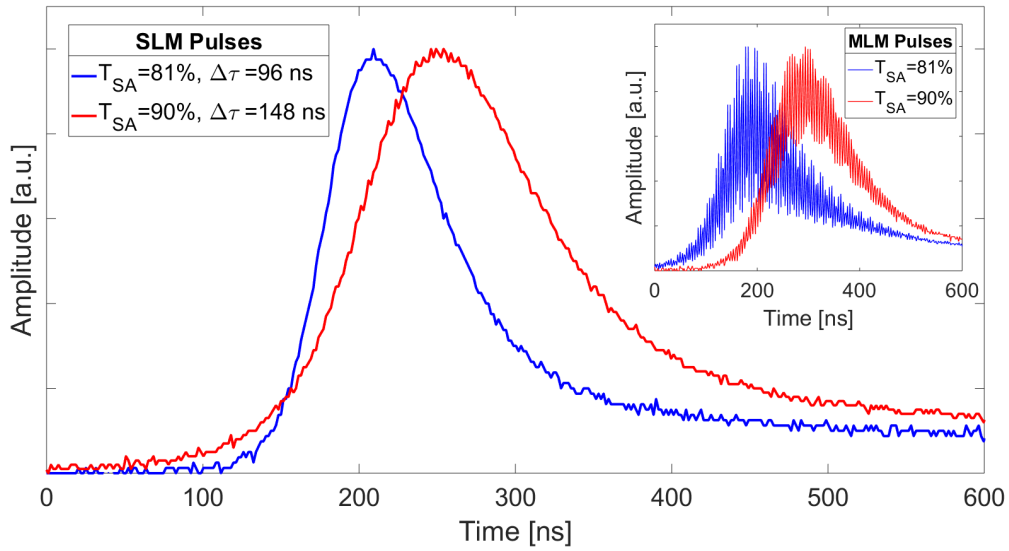

Figure 3.8: *Laser pulse oscilloscope traces, in the inset is showed MLM pulses.*

The use of the Fabry Perot scan interferometer allows to check mode hopping, and to quantify the linewidth of the emitted laser pulses Fig.(3.9). It was observed that no mode hopping happened and the measured pulse bandwidth FWHM was below 8.2 MHz. Considering transform limited pulses, the oscillating SISRO laser has narrower emitted bandwidths compared to the scanning interferometer. Then it can be stated only that the pulse linewidth is < 8.2 MHz. The pulse spectrum measured with the FP scan interferometer is discrete due to pulsed operation. The low quality of the shape observed with the FP scan interferometer is due to the high pulse-to-pulse time jitter.

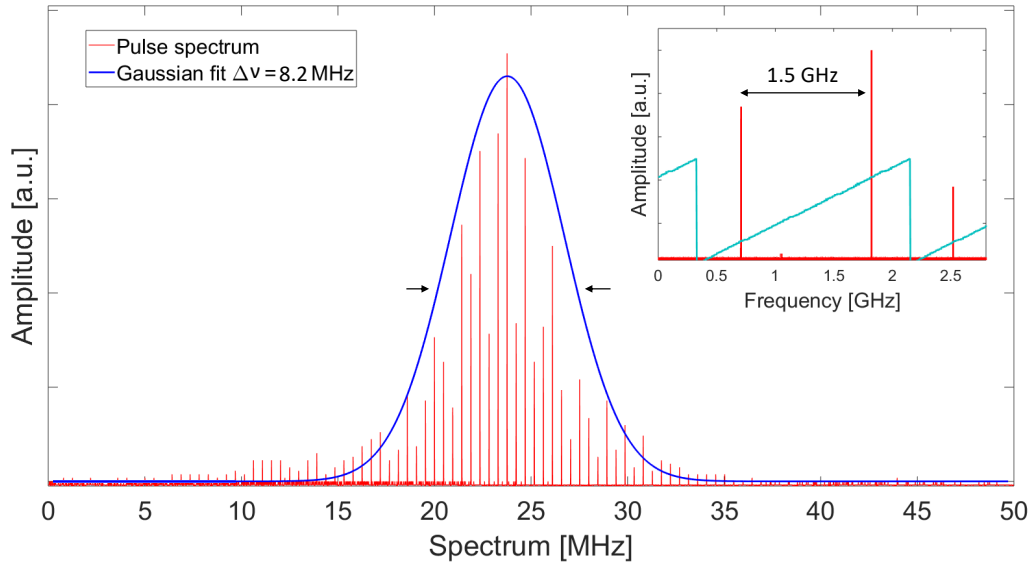

Figure 3.9: *731 mm long SISRO 148 ns pulse spectrum measured by means of the SA200 FP scan interferometer, in the inset it is showed nearly SLM operation.*

The pulse repetition rate depends on the incident pump power: above the threshold, a further increase of the pump power results in an increase of the pulse repetition rate, as it shown in Fig. (3.10). However, any pump power increment does not alter the pulse energy and temporal performance. If the repetition rate is several times higher the $1/\tau_f$, then the previous statement does not hold true. Then, it should be considered the low frequency regime and the high frequency regime. In this work, the SISRO design operates in the low frequency regime (<10 kHz for the Nd:YVO_4 and <5 kHz for the Nd:YAG).

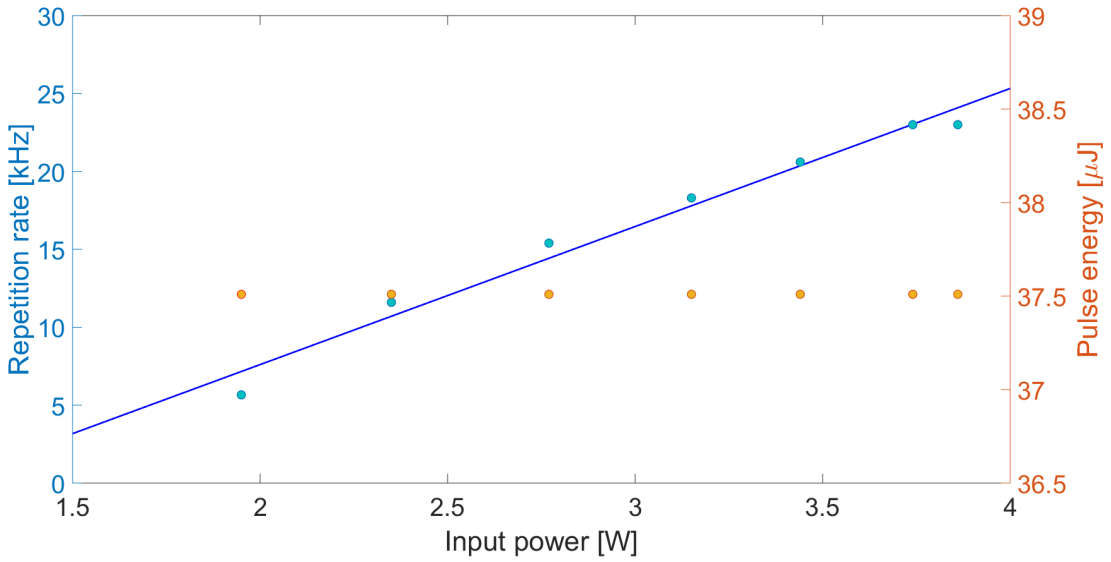

Figure 3.10: *Laser pulse repetition rate and pulse energy for 150 ns pulses.*

The peak power reached by the ring laser with $T_{SA} = 88\%$ and $T_{SA} = 79\%$ are respectively 0.5 kW and 1.1 kW. Recalling that the output coupler has a reflectivity of 90%, in the ring oscillator, we can estimate the peak power of the pulse intracavity as 5 kW and 11 kW, respectively.

The results obtained confirmed SLM operation with small FSR (only 440 MHz) compared to the gain bandwidth of 265 GHz ($\sim$1 nm). This motivated further investigation of shorter ring resonators in order to enhance SLM operation stability.

A cavity long 452 mm, i.e. a FSR of 630 MHz, was realized employing the same active medium Nd:YVO_4 crystal. The cavity employed the same mirrors, excepted for one curved mirror, which had a curvature radius of r =50 mm (M_3). For this system laser diode n°2 in pulsed regime was employed in order to reduce pulse-to-pulse time jitter. The aimed improvement was to reduce SLM instabilities with the combination of a shorter cavity and smaller thermal load (due to pulsed pumping at lower repetition rates). Pump pulse duration could be varied in the range of few tens of microseconds. The new pulsed pump was expected to decrease the amount of jitter by modulating the laser gain at well defined frequencies. The power efficiency is similar to the previous design, showing a slope efficiency of $\sim$ 55% without and $\sim$ 45% with the etalon inserted. The spectral behavior is the same regarding the CW and PQS operation, i.e., self injection seeding aids SLM operation for pulsed operation. To improve alignment tolerance for the feedback mirror, it was placed close to the focal plane of a $f = 50$ mm spherical lens. The misalignment tolerance of the feedback mirror increased by an order of magnitude, and this improvement was crucial to obtain a more reliable SLM

operation. When the etalon was finely aligned off-axis and the feedback mirror was in action, the PQS laser operated unidirectionally in SLM regime from 100 Hz to 10 kHz repetition rate. Laser pulses of 72 ns, 47 ns and pulses energies 45 μJ, 80 μJ for $T_{SA} = 88\%$ and $T_{SA} = 79\%$ were observed.

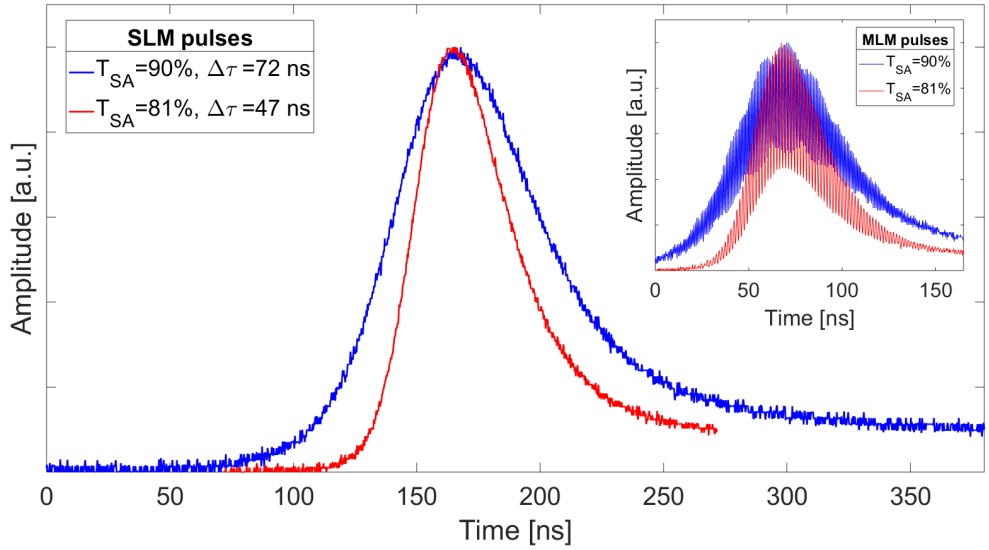

Figure 3.11: *SLM pulses emitted with SISRO (452 mm) employing PQS by mean of Cr:YAG.*

The pulsed pump enables to emit laser pulse with drastically lower pulse-to-pulse time jitter, decreasing the standard deviation rise time delay between the pump square signal and the optical pulse from μs order to few hundreds of ns. The reduced pulse-to-pulse time jitter compared to CW pumping, allowed to improve the spectrum analysis by mean of the scan interferometer.

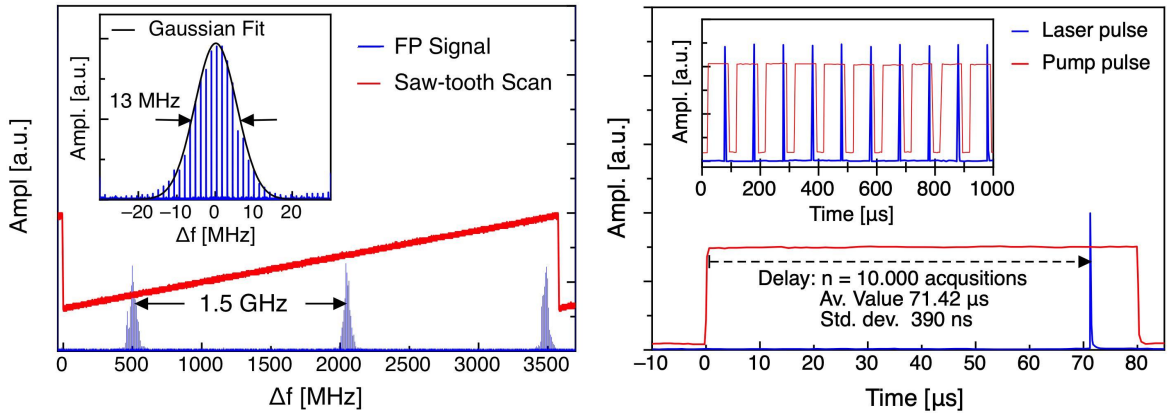

Figure 3.12: *Pulse spectrum obtained by means of scan inteferometer, in the inset it is displayed the pulse linewidth. In the picture on the right it is shown the pulse-to-pulse time jitter measured with respect to the pump pulse leading edge.*

In this case, the spectrum obtained is more reliable. In order to extract a more precise data, a de-convolution has to be used. Indeed the convolution between two Gaussians (i.e. the

scan interferometer resonance bandwidth and the pulse spectrum) is still a Gaussian, with a resulting variance equals to:

$$\sigma_{measured} = \sqrt{\sigma^2_{intereferometer} + \sigma^2_{pulse}}, \tag{3.3}$$

Recalling that the Gaussian Variance is related to the FWHM bandwidth, then the effective laser spectrum measured with the FP scan interferometer can be derived:

$$\Delta\nu_{pulse} = \sqrt{(\Delta\nu_{measured})^2 - (\Delta\nu_{interferometer})^2}, \tag{3.4}$$

Then, the effective pulse bandwidth emitted by the system is 10.6 MHz for the 48 ns long pulses, yielding a time-bandwidth product of 0.51. For the previous configuration the pulse linewidth is 3.3 MHz, meaning a time-bandwidth product of 0.488, which is extremely close to the transform limit.
The pulse stability, most notably the drift of build-up time, was confirmed to depend critically on the temperature stability of the laser diode. When this was stabilized within around 1%, the PQS pulse delay with respect to pump leading edge was stable within 400 ns for 10.000 acquisitions at 10 KHz repetition rate. This was the intrinsic jitter of the PQS pulse in our optimized setup. The pulse width and amplitude were also stable within 1%. The cyclically changing of absorbed power (and laser crystal temperature) as the diode wavelength oscillates near the controller set-point, produces a shift of the longitudinal mode pattern within the etalon transmission spectrum as observed for the previous ring laser design. After one longitudinal mode is tuned close to the gain peak, thermal drifts cause to lose the SLM operation. Such thermal (or power) sensitivity has been calculated from the temperature rise due to pump absorption, averaged along the crystal length.

$$< \Delta T >= \frac{\eta_h P_{abs}}{4\pi k_0 l_x} \ln\left(\frac{R}{r_p}\right)^2, \tag{3.5}$$

Where $\eta_h = 0.24$ is the fractional heat load (due to quantum defect), $k_0 = 8.9$ $\mathrm{Wm^{-1}K^{-1}}$ the thermal conductivity , $l_x = 8$ mm the crystal length, $r_p = 0.2$ mm the pump radius (assumed flat-top profile), $R = 1.5$ mm the crystal radius (assumed cylindrical in the model, not a critical limitation due to logarithmic dependence). The thermal change of cavity optical length, mostly due to heating, is:

$$\delta(nl_x) = \left[\alpha + \frac{1}{n}\frac{dn}{dT}\right] nl_x \delta T, \tag{3.6}$$

Where $\alpha = 1.910^{-6}K^{-1}$ [95] is the linear expansion coefficient along the direction of crystal length, $n = 2.17$ the refractive index and $dn/dT = 810^{-6}K^{-1}$ [95]. Stable SLM operation requires $|\delta(nl_x)|$ to be less than one half FSR of the cavity, corresponding to a shift allowing two modes to oscillate with the same strength. In practice, it is observed that 1% pump threshold oscillation (measured at the oscilloscope as the periodic drift of pulse delay from pump trailing edge) is sufficient to ensure long term stable SLM operation. The maximum fluctuation of absorbed power $\delta P_{abs} \sim 20$ mW, corresponds to $\delta T \sim 0.03$ °C and $|\delta(nl_x)| \sim \lambda/350 \ll \lambda/2$. This is the temperature stability requirement of the laser crystal. Furthermore, the etalon tilt had to be slightly adjusted when changing the pump power. This can be understood since the

peak wavelength of the cross section drifts with temperature by 0.2 pm/°C or 530 MHz/°C [96]. However this was not very critical since the gain spectrum is much broader than cavity FSR and etalon spectral width.

Spatial beam quality was was measured using a CCD camera, scanning along the focus of a $f = 75$ mm lens the laser radiation. Even at the maximum pulse repetition rate, the beam quality was excellent $M^2 < 1.1$.

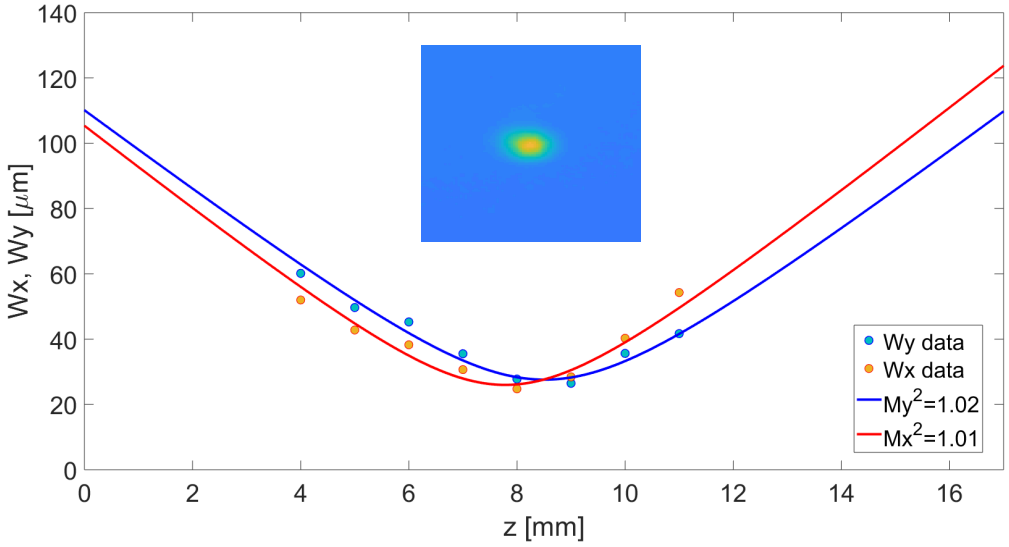

Figure 3.13: *Laser beam quality obtained with 452 mm long SISRO.*

We also tested the cw pumping regime, i.e., without pump moudulation, in order to compare the PQS pulse-to-pulse time jitter. After a few minute, necessary to reach steady-state thermal condition of the laser crystal, and with a slight etalon re-alignment, the pulse were still SLM. Although the temperature controller of the laser diode was performing with the same stability level as in the previous tests on the 731 mm long laser, the jitter increased significantly up to a few %. This suggest that pump modulation is effective in reducing the pulse-to-pulse time jitter.

The external feedback mirror was essential for SLM operation of the PQS ring laser, either with cw or pulsed pump. The focusing lens L for improving the misalignment tolerance of such mirror was also essential, since the angular tolerance reduced from 3 mrad to 0.15 mrad for PQS with respect to cw operation.

The third Bow-Tie SISRO laser oscillator was realized to investigate the Nd:YAG as active medium. This material is more attractive for SLM operation because of the narrower gain bandwidth (around half the Nd:YVO_4 bandwidth) and the better thermal conductivity. The higher thermal conductivity reduces the possibility of mode hopping and thermally induced instabilities. The resonator length was 540 mm, meaning a FSR of 450 MHz. The laser behavior in both CW and PQS is consistent with the performance observed with the Nd:YVO_4 based SISRO lasers. The pulse generated were SLM but shared the same instabilities for comparable time of scale. Pulses of 95 ns, 55 ns delivered energies of 70 μJ and 135 μJ respectively obtained with SA initial transmissions of 88% and 79%. It was observed that modifying the Cr:YAG position along the propagation axis of few mm, it was possible to slightly change the pulse duration of tens of nanoseconds and output energy of tens

of microjoules, without altering the other system performance. The measured laser slope efficiency is 41%. The measured laser bandwidth of 55 ns pulses was of 13 MHz, which traduced in effective pulse bandwidth of 10.6 MHz, recalling (3.4). Then, the time-bandwidth product is 0.583. The overall system performance and SLM stability were comparable to the 452 mm long laser oscillator for the frequency range between 100 Hz and 2 kHz, allowing higher energy output. For repetition rate higher than 2 kHz, the laser struggles to achieve SLM operation.

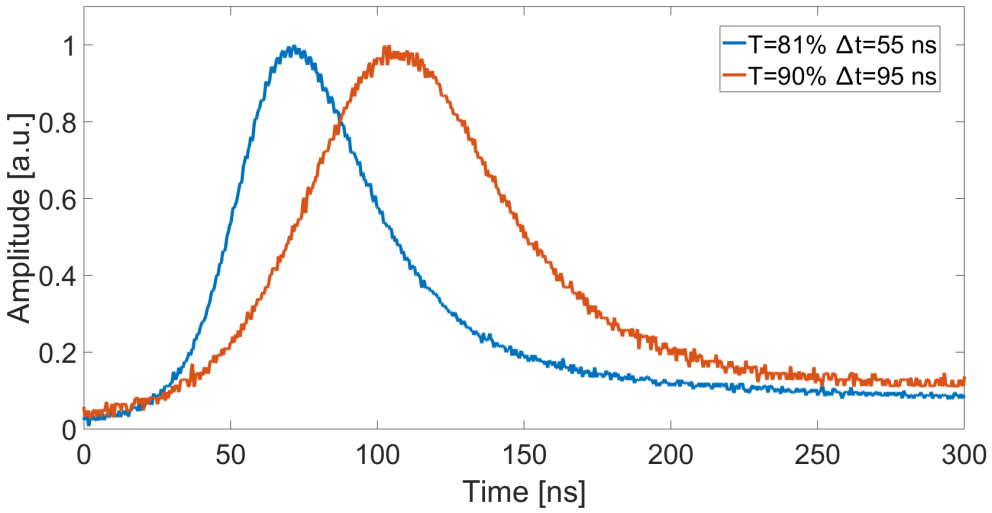

Figure 3.14: *SLM pulses emitted with SISRO (540 mm) employing PQS by mean of Cr:YAG.*

A table summarising all the optical properties of the SISRO laser tested is reported below:

Crystals	L [mm]	FSR [MHz]	T_{SA} [%]	P_f/P_i [%]	E_p [μJ]	t_p [ns]	S [MHz]
Nd:YVO_4	741	410	88	1-2	36	148	<8.2 (3)
Nd:YVO_4	741	410	79	2-3	51	96	<11 (4.5)
Nd:YVO_4	492	630	88	1-2	45	73	<12 (6)
Nd:YVO_4	492	630	79	2-3	80	48	<13 (9)
Nd:YAG	540	540	88	1-2	70	95	<11 (4.6)
Nd:YAG	540	540	79	2-3	135	60	<13 (7.3)

Table 3.1: *SISRO lasers performance*

The first three columns indicate crystal material, the cavity length and the free spectral range. The T_{SA} is the initial transmission of the saturable absorber. P_f and P_i are respectively the feedback power and the intracavity power. E_p and t_p are the pulse energy and time width. S indicates the measured pulse linewidth by means of Fabry Perot scan interferometer, within the brackets it is indicated the theoretical transform limit spectrum bandwidth. All the data have been obtained with an output coupler with R=90% and in the low frequency regime (i.e. $f_c<1/\tau_f$). The number of modes under the gain curve can be estimated dividing the optical gain bandwidth $g(\nu)$ with the cavity FSR. The three cavities exhibit hundreds of modes:

$$n°_{modes} = g(\nu)/FSR, \tag{3.7}$$

From Eq.(3.7) the number of mode under the gain curve are respectively: 646, 398 and 286 for the Nd:YVO_4 cavities and Nd:YAG cavity. These numbers indicate the challenge for a laser oscillator to operate on one axial mode for small FSR values.

3.4 Lesson learned

Mode selectivity in CW and PQS regime for SISRO architecture was investigated experimentally. For SLM pulses generation SISRO architecture is extremely attractive for both simplicity and performance. The role of the external mirror for self injection seeding was essential for ensuring unidirectional SLM in the PQS laser. The narrow angular tolerance could be increased by placing the mirror near the focal plane of a short focal lens, the positioning of the mirror was not critical. Temperature stability of the laser crystal requires a proper diode temperature control to a few 0.01 °C, allowing the absorbed pump power stabilization within 1%, leading to stable tuning between the longitudinal modes of the cavity and the etalon resonance peak. Also a temperature control over the crystal medium could be beneficial for high power oscillator design. Commercial electronics are able to achieve these requirements. Pump modulation was very effective in reducing pulse jitter to $< 0.1\%$ of the pulse period. Longer pulses up to 100 ns could be generated with this laser architecture, possibly with different gain media or stronger filters in order to satisfy the temporal criterion for SLM PQS lasers [97]. It should be noticed that it is also expected that longer resonators will require higher accuracy in temperature control to maintain the axial modes locked to the gain and etalon peaks, due to the reduced FSR of the cavity. The comparison between Nd:YVO_4 and Nd:YAG showed that the two materials are well suited for SLM operation, performing with comparable pulse-to-pulse time jitter. The Nd:YVO_4 should be preferred for high repetition rate, low jitter applications, whereas for more resilient SLM operation Nd:YAG should be chosen, because of the higher thermal coefficient and narrower optical gain bandwidth. Nd:YAG also allows to achieve higher pulse energy at low repetition rate and PQS operation with Cr:YAG saturable absorber is achieved more easily, as it is well known from PQS theory.

Chapter 4

SISRO stabilization

A new square ring laser layout instead of the previous Bow-Tie architecture has been developed to employ the SISRO technology. The new mechanical components were designed with CAD software in order to build a modular laser platform. This approach allows to reduce mechanical instabilities, to enhance thermal management and to achieve higher alignment precision. A square ring laser layout has been preferred in place of the bow-tie for the easier space management and possible modifications. Indeed, multiple optical combinations can be assembled with this structure.

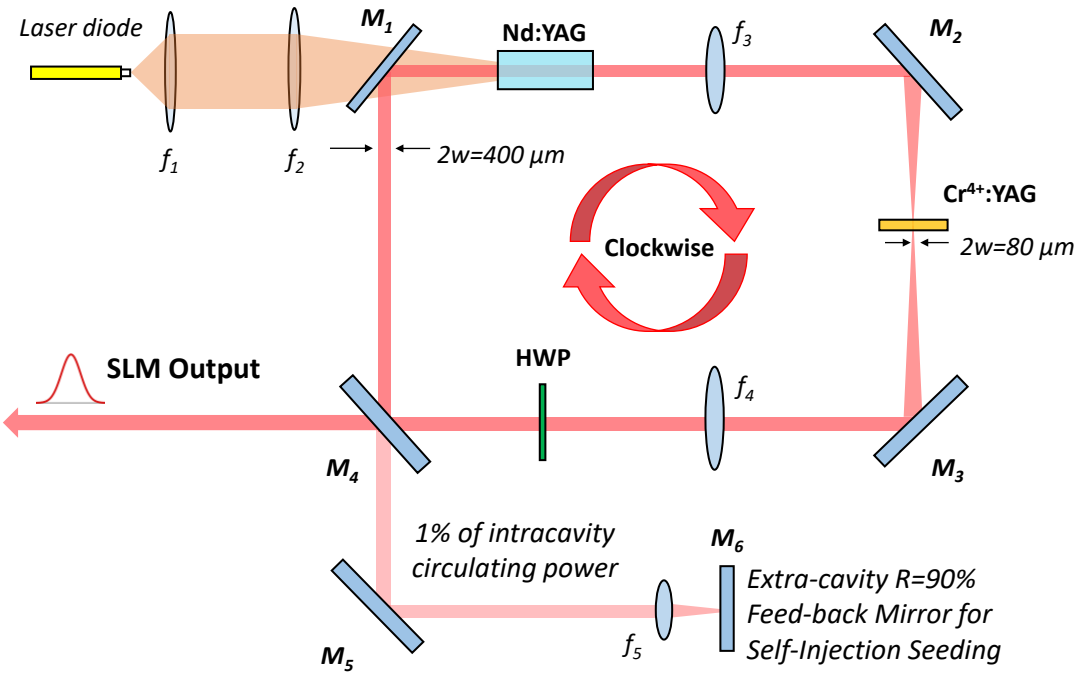

Figure 4.1: *SISRO 2nd architecture setup*

The laser cavity is composed by four flat reflectors. M_1 is the dichroic mirror for optical pumping, M_2 and M_3 are 45° HR mirrors and M_4 is polarizer beam splitter (which act as output coupler in combination with the half wave-plate or HWP). The pumping configuration is identical to the bow-tie laser SISRO. The laser diode n°2 output is coupled in the active medium by means of a achromatic telescope f_1 and f_2. Cavity stability is guaranteed by lenses

f_3 and f_4 instead of curved mirrors, but the focus is still reproduced in the saturable absorber in a similar fashion to the previous designs. The active medium chosen was the Nd:YAG due to the higher delivered energy, better thermal dissipation and a narrower gain bandwidth. The etalon has been removed for PQS operation. Self injection seeding is achieved by using a partially reflective mirror M_6, after folding and focusing by means of M_5 and f_5. The feedback mirror M_6 reflectivity is of R=90%.

4.1 ABCD matrix modelling and pump configuration

A cavity ABCD matrix simulation was performed for the square laser cavity, aiming to realize a collimated propagation region with a laser focus between the two lenses. This configuration was inspected for different lenses combinations and for different cavity lengths in order to guarantee laser stability and suitable mode areas for several possible cavity configurations allowed by the mechanical platform. The feedback mirror is a partially reflective mirror, enabling to monitor the unidirectional extinction power ratio (2.66). The cavity length chosen was ~ 200 mm employing a couple of 25 mm lenses.

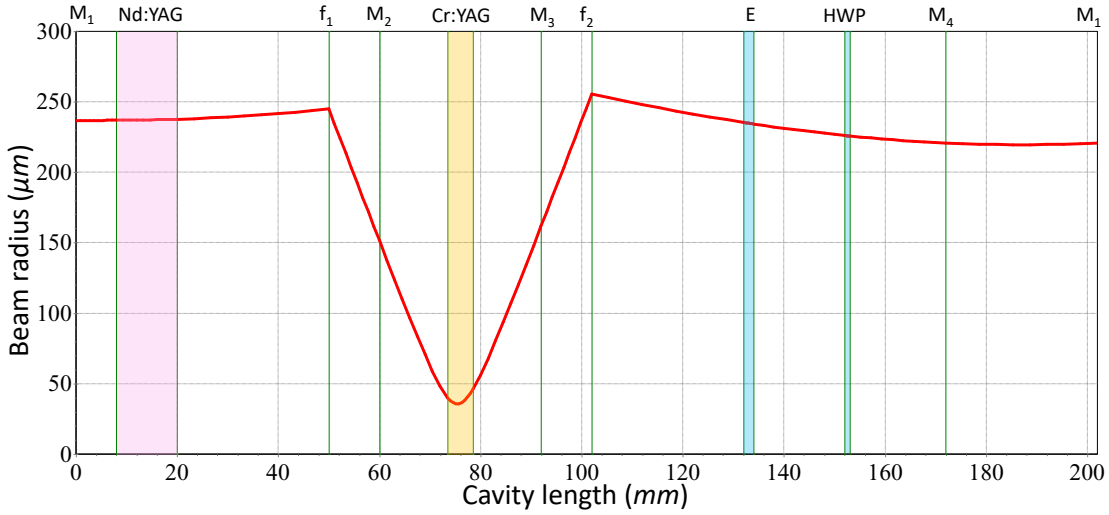

Figure 4.2: *Square ring (FSR=1.37) GHz ABCD simulation.*

The same pumping fiber laser diode for 540 mm Nd:YAG and 452 mm Nd:YVO_4 long ring oscillators have been used for this laser design. It is recalled that, the diode can deliver a maximum power of 6 W and it is able to operate in both CW and QCW regime. The fiber has a core diameter of about 105 µm (NA=0.22). The pump radiation is matched to the fundamental laser mode by means of a telescope with magnification factor 3.75, realized with two achromatic spherical lenses of 40 mm and 150 mm focal lengths.

The use of intracavity lenses instead of tilted curved mirrors enables to suppress any astigmatism and beam ellipticity, thus enhancing the beam quality output. The downside of this technique is the increase of intracavity optical losses, due to an higher number of optical elements and the residual losses of the AR coating of the lenses, which is typically higher with respect to the residual transmission of HR mirrors. After the ABCD description, the laser platform was designed in order to accommodate the square ring oscillators.

4.2 Laser platform

The laser platform has been developed using a Computer-aided design (CAD) software, which is the use of a computers software to design and test mechanical elements. Then, the 3D or 2D files are produced by CNC (Computer Numerica Control) machines such as millings for high quality mechanical objects. CAD software is used to increase the productivity, design quality and the visualization of the final product, allowing easy debug as well. CAD file output assumes different form of electronic files for print, machining, or other manufacturing operations. The most universal/portable 3D file extension is the ".stl", whereas for the 2D files it is the ".dwg" file extension. In my experience I operated with Autodesk Inventor CAD software [98], which allows both 3D and 2D mechanical drawing. The basement is a unique aluminium piece linked to a platform through a Peltier cell for thermal control. The smaller platform hosts several combination of slides on top of which the optical holders can be placed and assembled. Laser cavity lengths from 100 mm to 220 mm can be realized with this modular platform, enabling a wide variety of optical elements configurations, as in the examples illustrated in the figures below.

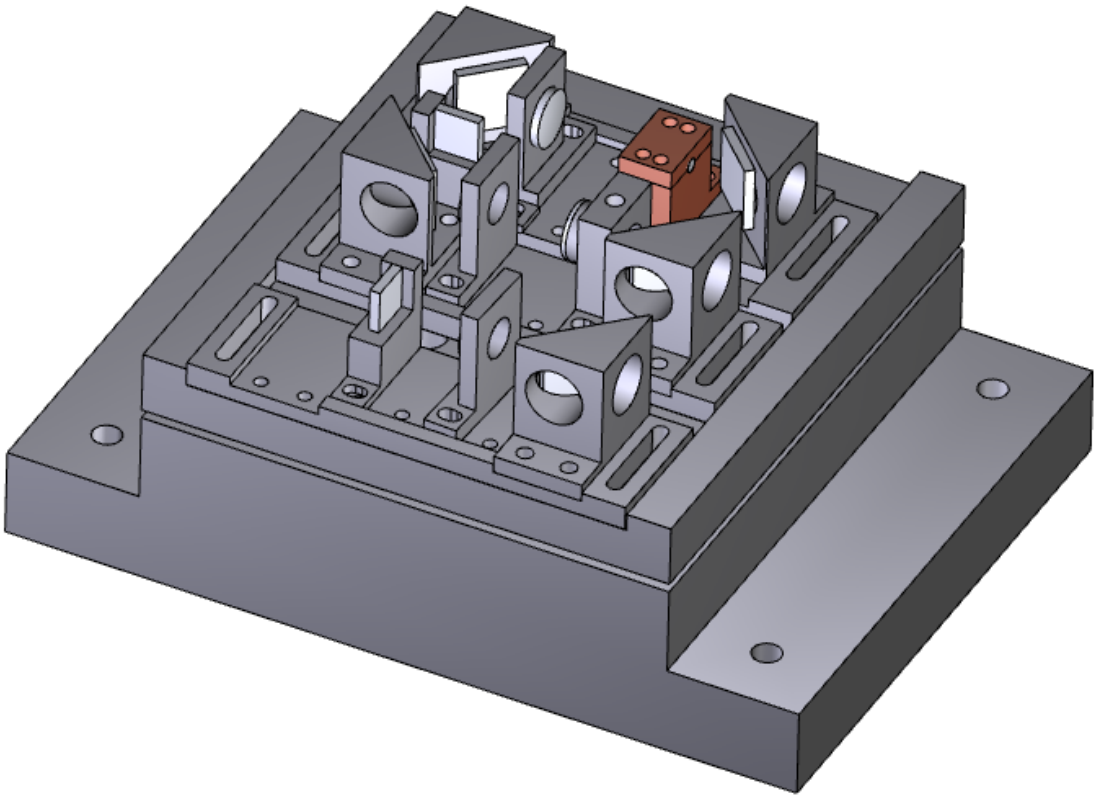

Figure 4.3: *CAD designed modular platform, example of a SISRO laser.*

The SISRO was assembled by positioning the four perimeter mirrors first. The active medium is placed in a copper holder wrapped in indium foils and a thermal conductive adhesive is used to interface the copper holder to the aluminium slit to guarantee maximum heat dissipation. Two spherical lenses with 25 mm focal length were placed as showed in Fig. (4.3), mounted on transitional stages for laser alignment. The small focal length enables to easily align the laser cavity due to the optical leverage. The HWP (Half Wave Plate) and the PBS

(polarizer Beam Splitter) were used as a variable output coupler. An additional slit could be placed for the etalon mount. Cavity alignment required only two spherical lenses, whereas all the other elements were pre-assembled, by gluing them on the mechanical mounts. The use of the two lenses allows to compensate the mechanical imprecision, thus effectively aligning only two optical elements to start laser oscillation.

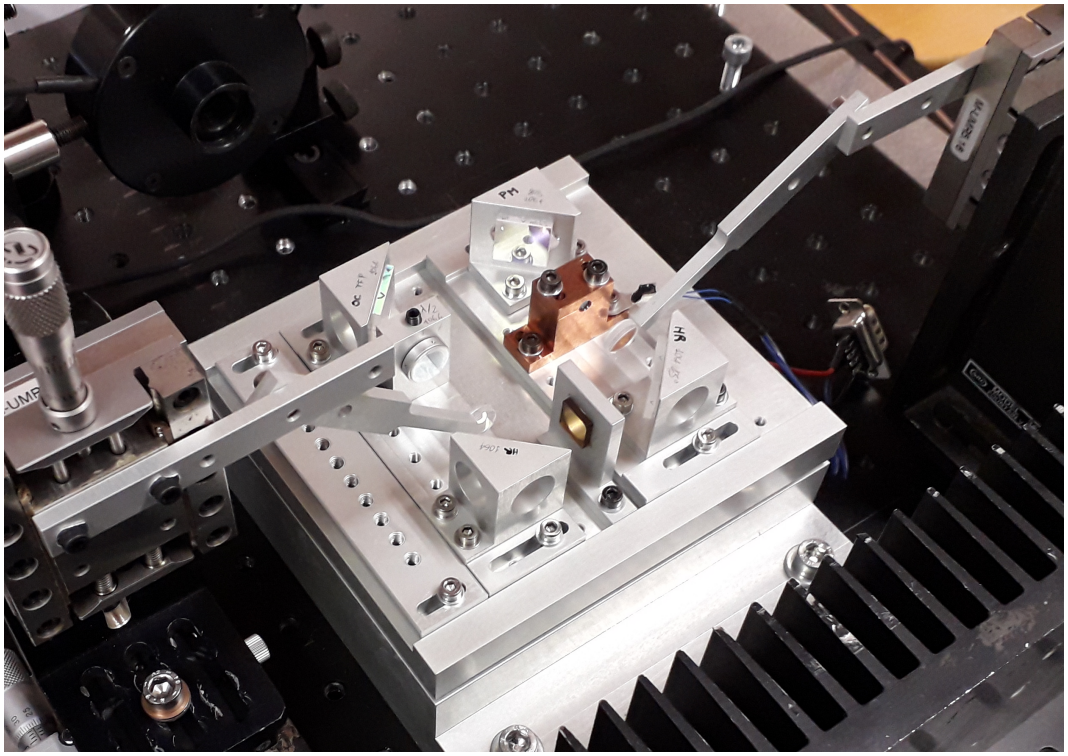

Figure 4.4: *SISRO Laser assembled on the platform, during aligning (top view).*

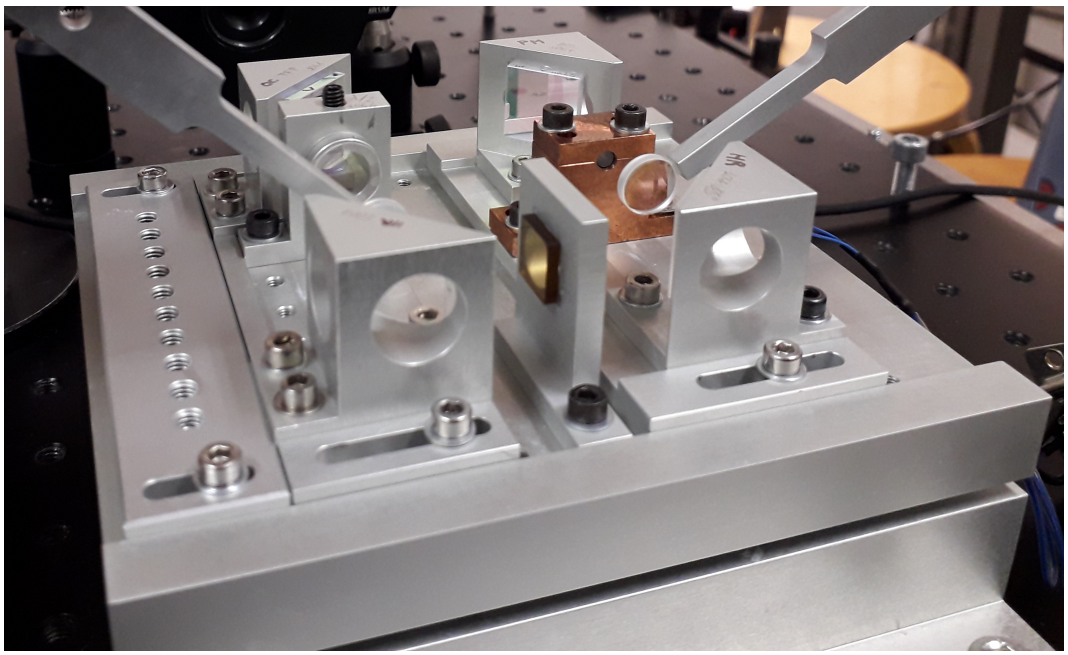

Figure 4.5: *SISRO Laser assembled on the platform, during aligning (side view).*

4.3 Experimental results

The laser oscillator operating in CW regime showed inferior performance with respect to the 4-mirror bow-tie resonator in terms of output power, because of the higher intracavity losses of the new configuration. To evaluate the intracavity losses, the Caird analysis [99] was performed, revealing around 3% of intracavity losses and 40% of system efficiency. The maximum slope efficiency of 30% was achieved for an equivalent output coupler of reflectivity R=93%. The square ring slope efficiency was lower if compared to the bow-tie; it was about 30% for optimum coupling against around 50% for R=90%, respectively.

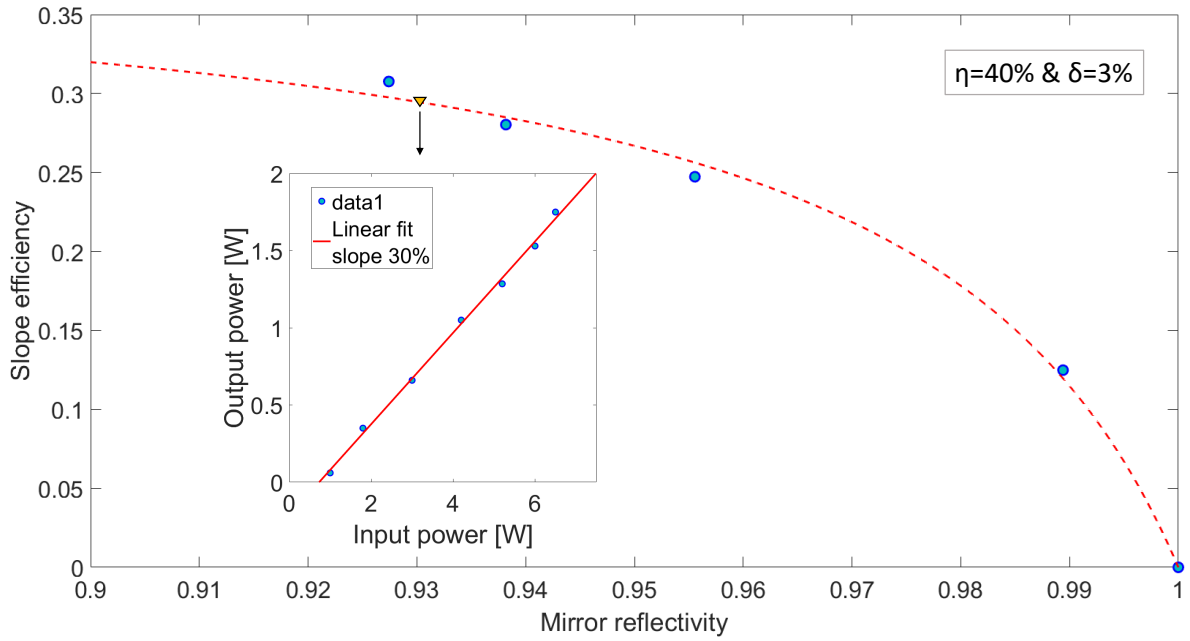

Figure 4.6: *Laser Caird analysis and power characterization.*

The laser spectrum displayed the same behavior of the previous designs. SLM operation was easily achieved without self injection seeding during CW operation with the etalon inserted in the cavity. SLM operation with self injection seeding could be achieved with fine alignment of the etalon, but this regime proved highly unstable, bi-modal operation was the most frequent regime. The system with the use of the etalon could be tuned in wavelength under the peak of the gain bandwidth, enabling this laser architecture for secondary seeding application where two spatially identical outputs are needed. Switching to PQS regime, the system operated stably on one axial mode with self-injection seeding without the need of the etalon. The system operated from low repetition rate (100 Hz) to moderate frequencies (8 kHz). The use of the FP etalon proved to be detrimental for SLM stability in this regime, requiring further aligning procedures. Without the etalon the system was reliable and insensitive to thermal pump changes and to mechanical perturbations. The saturable absorber initial transmissions T_{SA} were lower compared to previous designs, T_{SA}= 88% and T_{SA}= 93%. These SAs allowed to generate laser pulse of 35 ns, 50 ns and energies of 67 μJ, 34 μJ respectively. SLM operation was observed for repetition rates ranging from 100 Hz to 10 kHz for T_{SA}= 90% and from 100 Hz to 8 kHz for T_{SA}= 93%. Pulse-to-pulse time jitter showed a standard deviation of hundreds nanoseconds between rise time of the laser pulse and the end front of

the electronically controlled pump pulse, displaying a slightly better performance compared to the previous oscillators.

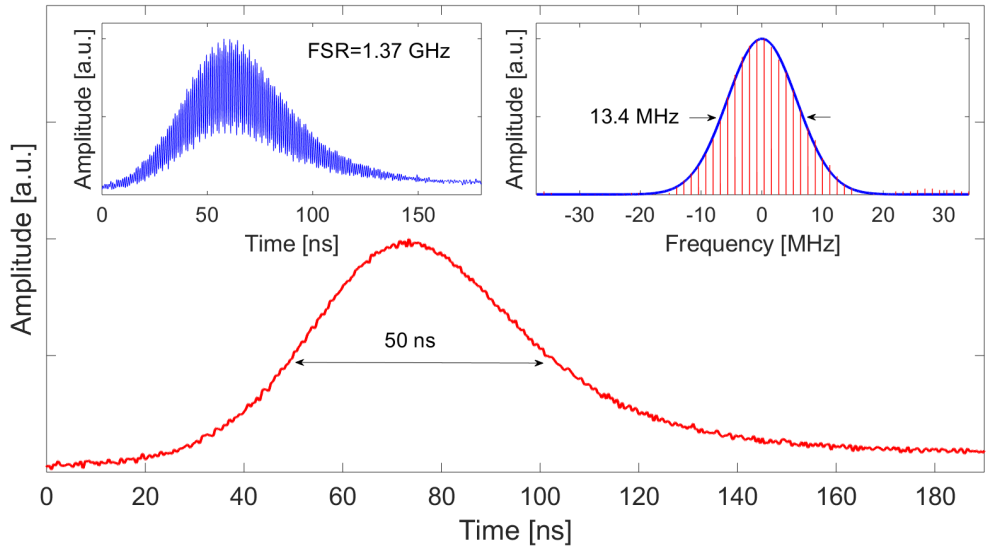

Figure 4.7: *Laser pulse traces for SISRO new square ring oscillator, left inset shows the pulse trace without self seeding and the right inset shows the spectral content of the SLM pulse.*

The laser pulse traces and the pulses spectrum have been recorded for several repetition rate configurations to observe SLM operation. The laser FSR = 1.37 GHz, can still be resolved by our oscilloscope, as it can be seen in the inset of (4.7).

The laser beam quality was measured by means of a CCD camera. Out of the laser oscillator a f_3=150 mm spherical lens was used to collimate the laser radiation and then beam quality was inspected in the focus of a f_4=75 mm spherical lens. The result is shown in Fig. (4.8) The beam quality was near to diffraction limited and no appreciable astigmatism was observed, thanks to the cavity configuration.

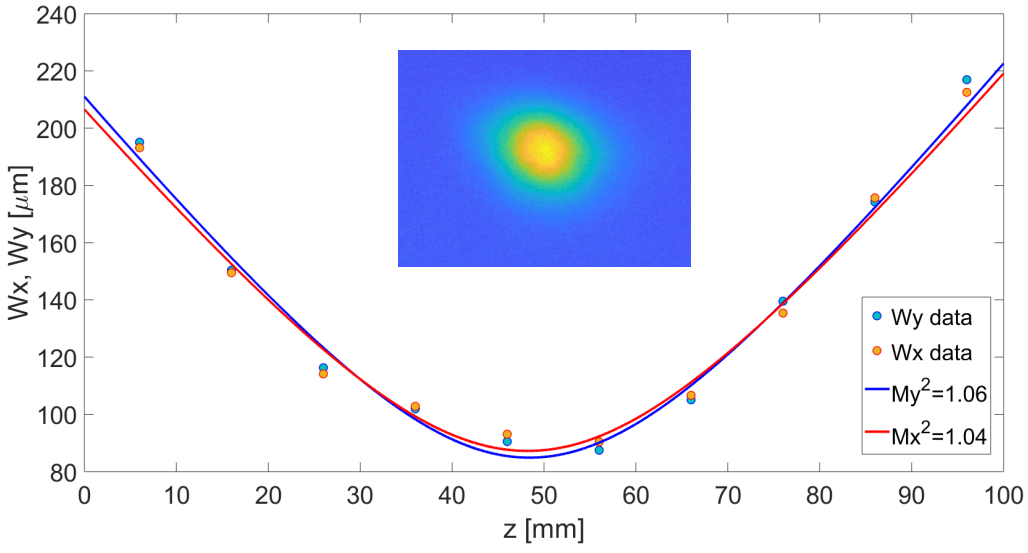

Figure 4.8: *Laser beam quality and profile of the square SISRO architecture.*

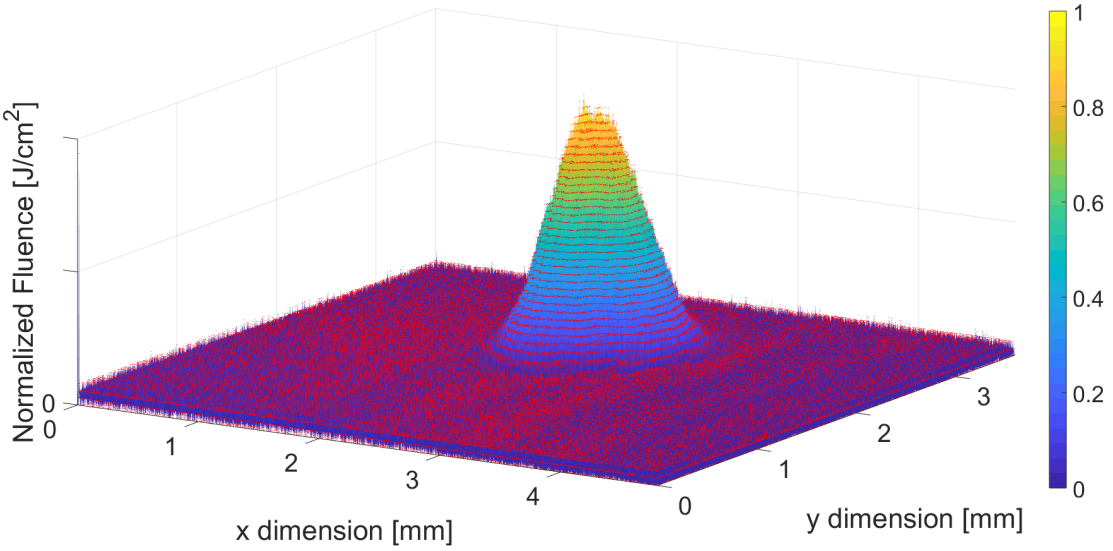

Figure 4.9: *Laser beam intensity profile in 3d.*

The beam waist measured in the focus of the telecope is consistent with the ABCD cavity model. The laser output wavelength for different repetition rates showed a drift of only 80 pm, from 1063.95 nm at 1 kHz to 1064.03 nm at 8 kHz, due to the different heating of the active medium at different thermal load.

Unidirectional propagation and SLM operation versus self seeding power were investigated to address the system sensitivity to seeding power instabilities. A quarter wave plate was placed in the feedback arm, allowing to modulate the re-entering power in the cavity by orientating the wave plate, as it is shown in Fig. (4.10)

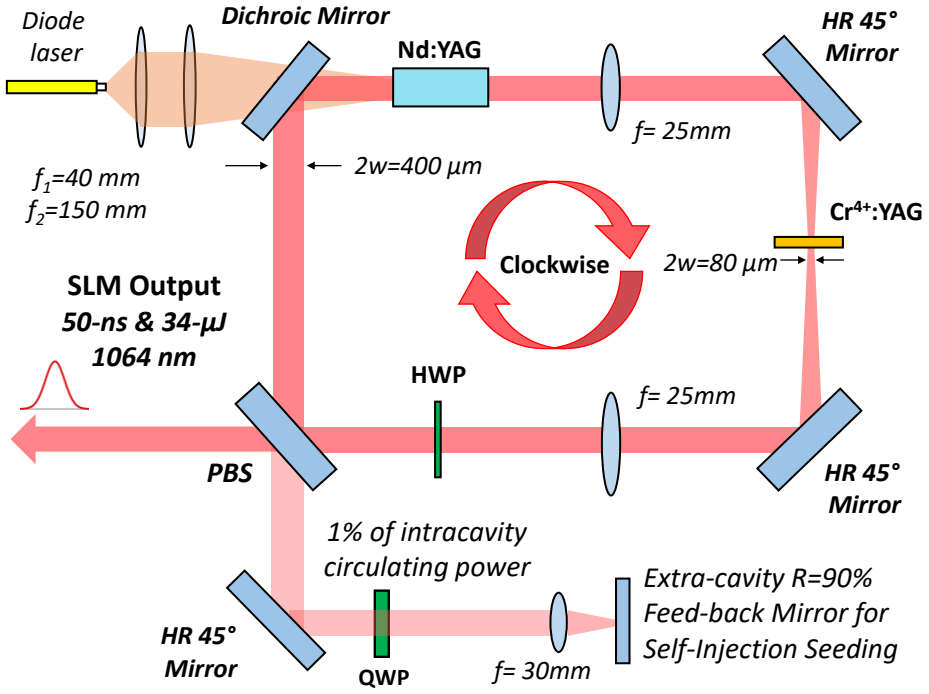

Figure 4.10: *Laser unidirecionality and SLM operation statistics versus self seeding power.*

By rotating the wave plate, it was possible to derive the unidirectional power ratio (2.66) and the energy ratio between secondary modes and the fundamental one by means of FFT.

$$C = \frac{2\int_{0}^{FSR/2} S(\nu)d\nu}{\int_{FSR/2}^{\infty} S(\nu)d\nu}, \tag{4.1}$$

It can be observed that for Re-entering power superior to 50%, the system is able to operate stably on one axial mode with a very high contrast ratio C for an average over 10 000 samples, with strong unidirectional radiation path inside the cavity. SLM performance starts to become unstable below 50% of seeding power, whereas the unidirectional extinction ratio has a monotonic behavior toward the 0% value. The minimum unidirectional ratio seems to be around 45%, but if the seeding beam is interrupted with a beam blocker, the unidirectionality ratio drop close to 0%. This indicates that a very weak seeding signal with a optimal beam overlap is sufficient to drastically affect the oscillator. It appears clear that SLM operation condition is an harder regime compared to travelling wave operation. Indeed for almost constant unidirectionality ratio the contrast ratio C worsened significantly earlier.

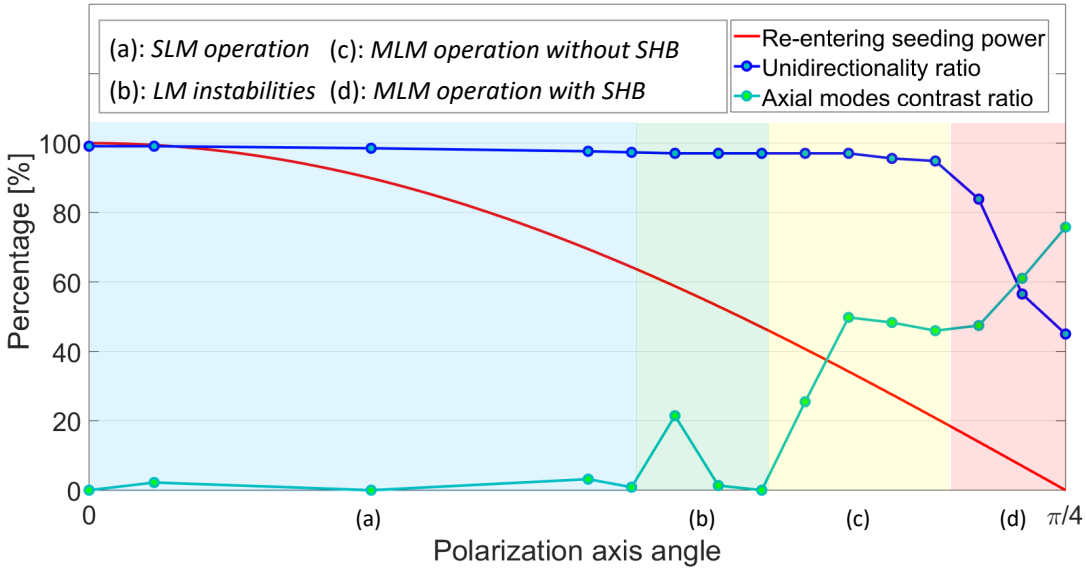

Figure 4.11: *Laser unidirecionality and SLM operation statistics versus self seeding power.*

4.4 Lesson learned

The new mechanical modular frame proved to be extremely beneficial for reducing thermal and mechanical instabilities. The system operated in SLM mode with high reliability, allowing at the same time to realize a more compact ring laser cavity fast to assembly and alignment. The system, although less energy efficient due to an higher intracavity number of optical elements, is very attractive for the wide range of feasible configurations. Thus, the system for PQS regime achieved significant improvements, considering that no etalon was needed. The 220 mm long SISRO enabled reliable SLM operation for repetition rates

between 100 Hz and 8-10 kHz. Beam quality was excellent, showing a nearly TEM_{00} transverse mode and no significant astigmatism. Unidirectionality, SLM operation and pulse-to-pulse time jitter compared to seeding power have been investigated, showing the sensitivity of SISRO technology regarding the seeding power. The remaining undesired behavior of the system is the relatively high pulse-to-pulse time jitter. The following research aimed to further reduce the temporal jitter, in order to enhance the SISRO technology.

4.5 PQS model validation

The numerical solution of the mathematical model proposed in Sec. (2.2) were compared to the experimetal values:

Laser Medium	$Nd:YVO_4$	$Nd:YVO_4$	Nd:YAG	Nd:YAG
Resonator type	Ring Bow-Tie	Ring Bow-Tie	Ring Bow-Tie	Ring square
Saturation fluence	0.12[J/cm^2]	0.12[J/cm^2]	0.57 [J/cm^2]	0.57 [J/cm^2]
Cavity length [mm]	741	492	540	220
Output coupler R	0.9	0.9	0.9	0.93
Saturable absorber T	0.88	0.88	0.88	0.93
Intracavity losses	4%	4%	4%	4%
Beam radius$[\mu m]$	240*	270*	200*	180*
Energy $E_{exp}[\mu J]$	36	45	70	34
Energy $E_{mod}[\mu J]$	28	35	91	39
Energy error	22%	22%	23%	13%
Pulse $\tau_{exp}[ns]$	148	73	95	50
Pulse $\tau_{mod}[ns]$	137	91	100	66
Pulse error	7%	19%	5%	24%

Table 4.1: *PQS model and experimental data. The values indicates with "*" are assumptions based on ABCD simulations.*

Saturation fluence is taken by [100] for $Nd:YVO_4$ and Nd:YAG. The cavity length is experimentally measured within 1 mm precision. The outcoupler reflecitivity R and Saturable absorber initial transmission T. The intracavity losses are set to few %. For the bow-tie ring oscillators the etalon losses must be taken into account and similarly for the square ring oscillator all intracavity optical elements such as lenses and the HWP are responsible of additional losses too. The beam radius is directly calculated for the square ring layout due to the absence of ellipticity. In the Bow-tie architectures an effective beam radius is derived because of the beam ellipticity. Beam radius can differ by ABCD simulations for several reasons such as gain/absorber apodization effects. In all cases, the agreement between experiment and model is satisfactory. While the energy depends mostly on the accuracy of mode radius, the pulse duration instead depends critically on the exact value of the induced losses by the saturable absorber. The model can be also successfully used in order to precisely identify the oscillator parameters by experimental data. This model has been tested also for other PQS oscillators in order to check its reliability [61].

4.6 Jitter reduction by SA bleaching

In order to decrease the pulse-to-pulse time jitter it was tested an optical diode to bleach the saturable absorber. It was decided to test a similar approach to transverse bleaching, described in [101]. The technique consists in triggering the bleaching of the saturable absorber with an external laser pulse. In this case, the technique has to be identified as longitudinal bleaching, in contrast to transverse bleaching. Since Cr:YAG has a broad absorption, this laser pulse can be produced by a laser diode at 808 nm, as the one at out disposal. This method is attractive because it allows in principle to control the optical switch in terms of intracavity optical losses and switch timing.

The optical diode employed for this purpose is a modified Bright Solution BFP diode laser, with a peak power of 10 W. The diode is fiber-coupled (NA=0.22, fiber core diameter of 105 µm) and emits at 808 nm. The modification regards the current driver, which enables to switch the optical laser diode with rise time and fall time of 50 ns. The bleaching laser beam is focused in the Cr:YAG by means of a achromatic lenses telescope. The two lenses focal lengths are respectively 100 mm and 80 mm, resulting in a beam waist in the focal plane of $w_{bl} \simeq 40$ μm, reasonably well matched to the cavity resonating mode inside the saturable absorber.

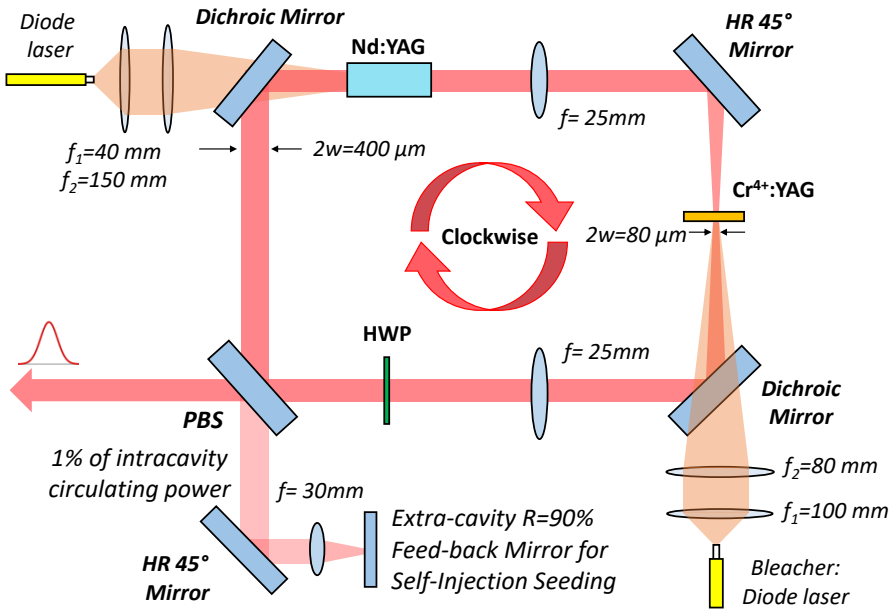

Figure 4.12: *Laser setup for pulse-to-pulse time jitter reduction by mean of SA bleaching.*

The bleaching laser was set in order to illuminate the saturable absorber with the maximum available peak power, hence permitting to minimize the bleaching pulse duration. The saturation fluence and recovery time of Cr^{4+}:YAG are 0.5 J/cm^2 and 8.5 μs, respectively [102]. Given the bleacher beam radius in the focus and maximum peak power, the peak intensity is about 180 kW/cm^2. Then, it is possible to reach Cr:YAG saturation energy with a $\sim$3 μs-long pulse width, significantly shorter than the recovery time of Cr:YAG. We tested the bleaching with different delays between the laser pump pulse and bleaching pulse. For the T_{SA}=90% without the bleaching pulse the SLM laser pulse would originate between 75 and 76 μs, measured from the raising edge of the pump pulse, with a standard deviation of few

hundreds of nanoseconds. With the bleaching pulse it is possible to anticipate the start of the SLM pulse to 72 μs, a condition achieved with a bleaching pulse delay of 66-68 μs. For shorter or longer delay time the pulse dynamics becomes less affected by the bleaching pulse. As expected, the anticipation of the laser pulse comes with a slight reduction of the pulse energy from $\sim$66 μJ without bleaching, to around 61 μJ.

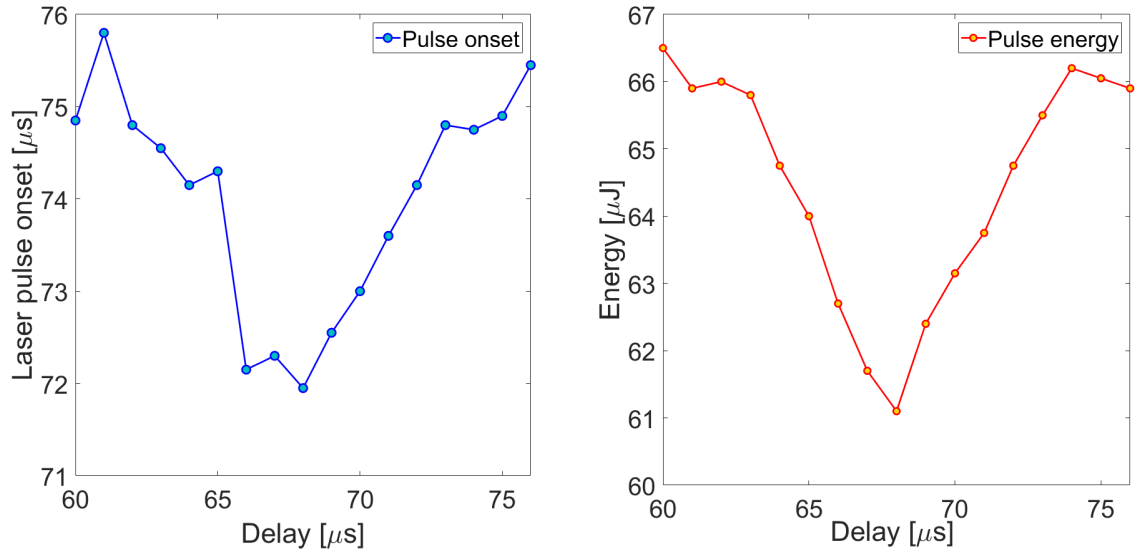

Figure 4.13: *SLM laser pulse start related to bleaching pulse timing.*

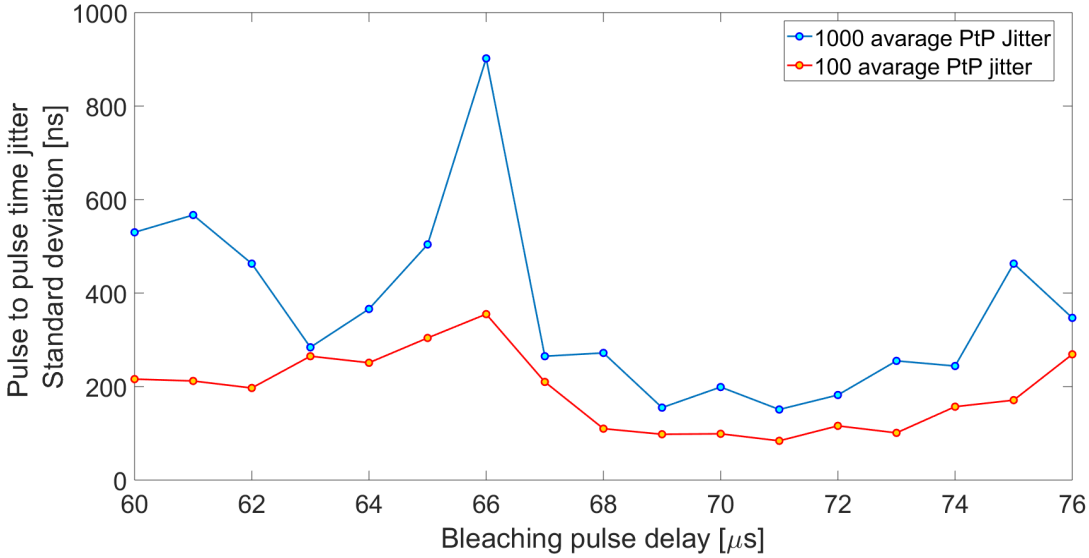

Figure 4.14: *SLM laser pulse to pulse time jitter related to bleaching pulse timing.*

Unfortunately, regarding the pulse to pulse time jitter, the results obtained were not satisfactory. The bleaching pulse was able to effectively anticipate the pulse onset, but did not significantly reduced the pulse to pulse time jitter. We may attribute this lack of performance, mainly to two reasons. Firstly, the available peak power of the laser diode used for the bleaching was barely sufficient to saturate the Cr:YAG. In this sense, a more powerful laser diode

would have definitely eased the process and permitted to use much shorter bleaching pulses. Secondly, and maybe more importantly, we suspect that in our operating conditions, if compared to [101] the intrinsic jitter of our source was already relatively small and the effect of the external bleaching is marginal. To better understand the possible sources of jitter and to develope a more succesful strategy for minimization of jitter, we decided to go back to the basics and try to model the behaviour of the PQS laser starting from the rate equations.

4.7 Jitter reduction by pumping pulses enhancement

Recalling the rate equation for population inversion density $n(t)$, laser pulse power $P(t)$ and SA losses dynamics $q(t)$ of a PQS system, [103]:

$$\begin{cases} \dfrac{dn}{dt} = W_P n_t - \dfrac{n}{\tau_f} - W_L n, \\ \dfrac{dp}{dt} = -\dfrac{(gP)}{t_R} - \dfrac{P}{\tau_c}, \\ \dfrac{dq}{dt} = -\dfrac{(q-q_0)}{\tau_A} - q\dfrac{P}{E_S A} \end{cases} \tag{4.2}$$

Where W_P, W_L are the pump absorption and laser emission rate, n_t is the dopant concentration-dependent active ions density, τ_f is the active medium fluorescence lifetime, g is the single pass gain coefficient, t_R and τ_c are the cavity roundtrip time and photon lifetime respectively, q_0 is the initial loss of the saturable absorber, τ_A is the SA recovery time and, E_{SA} is the SA saturation energy.

Describing the pulse "linear" growth until the onset of saturation, the loss dynamics are not relevant. Therefore, in (4.2), the loss is assumed to be constant and excited state absorption from the SA (e.g., in case of Cr:YAG) was also omitted. Then:

$$g = \int_0^l \sigma_L n(z) dz \tag{4.3}$$

The pump rate can be directly related to the absorbed pump power:

$$\sigma_L \int_0^l W_P(z) n_t dz = \eta \frac{\lambda_P}{\lambda_L} \frac{P_{abs}}{E_{SL}} \tag{4.4}$$

Where σ_L is the active medium emission cross section, λ_P and λ_L are the pump and laser wavelength, E_{SL} is saturation energy of the active medium and the coefficient η is accounting for quantum efficiency, pump/laser spatial overlap, Fresnel transmittivity. Then, with the proper substitutions:

$$\frac{dg}{dt} = \eta \frac{\lambda_P}{\lambda_L} \frac{P_{abs}}{E_{SL}} - \frac{g}{\tau_f} - \frac{gP}{E_{SL}} \tag{4.5}$$

In equation (4.5) during build-up after reaching laser threshold, the first term dominates since there will not be significant gain depletion due to stimulated emission and the build-up is much shorter than τ_f. Then:

$$g(t) \sim g_{th} + \eta \frac{\lambda_P}{\lambda_L} \frac{P_{abs}}{E_{SL}} t \tag{4.6}$$

Equation (4.6) represents a linear growth of the gain with time after the threshold value is reached. g_{th} can be expressed as:

$$g_{th} = \frac{t_R}{\tau_c} = L + q_0 - ln(R_{OC}) \tag{4.7}$$

Using equation (4.7) to recast the power equation (4.2):

$$\frac{dP}{P} = \eta \frac{\lambda_P}{\lambda_L} \frac{P_{abs}}{E_{SL}} \frac{t}{t_R} dt \tag{4.8}$$

Which can be easily integrated from t=0, which represents the instant of time in which g=g_{th} to the onset of laser pulse t_b.

$$ln\left(\frac{P(t_b)}{P_i}\right) = \eta \frac{\lambda_P}{\lambda_L} \frac{P_{abs}}{E_{SL}} \frac{t_b^2}{2t_R} \tag{4.9}$$

Eventually we can estimate the build-up time for the PQS pulse emission after the gain has reached threshold

$$t_b \sim \sqrt{\frac{\lambda_P}{\lambda_L} \frac{2E_{SL}t_R}{\eta P_{abs}} ln\left(\frac{P_{SA}}{P_i}\right)} \tag{4.10}$$

The choise of P_{SA} is not critical because of the logarithm, as well as a more precise estimation of starting noise (rather than the naive assumption of an initial "single photon" in the cavity round-trip time, i.e., $P_i \sim h\nu_L/t_R$). In particular, we can define a parameter $G = ln(P_{SA}/P_i) \sim$ 20-30 for a broad range of practical applications. Sensitivity (jitter) of build-up time from fluctuations of absorbed pump power P_{abs} or with respect to starting fluorescence noise P_i is readily obtained by differentiation of equation (4.10).

$$\frac{\delta_{b,1}}{t_b} = -\frac{1}{2} \frac{\delta P_{abs}}{P_{abs}} \tag{4.11}$$

$$\frac{\delta_{b,2}}{t_b} = -\frac{1}{2} \frac{\delta P_i / P_i}{ln(P_{SA}/P_i)} \tag{4.12}$$

The latter is going to be the main δt_b jitter contribution due to non-Poissonian (thermal) fluorescence photon statistics, predicting $\delta P_i/P_i \sim$1. It must be also considered the additional jitter from pump pulse rise front, i.e., fluctuations of the delay time t_0 at which $g = g_{th}$ starting from $g = 0$. Integrating equation (4.5) and neglecting the last term which is relevant only during gain saturation:

$$\int_0^{g_{th}} \frac{dg}{g - \eta \frac{\lambda_P}{\lambda_L} \frac{P_{abs}\tau_f}{E_{SL}}} = \int_0^{t_0} \frac{dt}{\tau_f} \tag{4.13}$$

Introducing the dimensions-less parameter x

$$x = g_{th} \frac{\lambda_P}{\lambda_L} \frac{E_{SL}}{\eta P_{abs} \tau_f} \tag{4.14}$$

Eq. (4.13) can be solved:

$$t_0 = -\tau_f ln(1-x) \tag{4.15}$$

PQS pulse generation from a single pump pulse requires that x <1. It is possible to estimate the $P_{abs,th}$ using the spectroscopic parameters of the active medium (emission cross section, fluorescence lifetime) with sufficient precision, the g_{th} by means of equation (4.7) and η, which can be obtained by Caird analysis. Practically, it can be observed by checking the peak pump power required to start PQS emission, or from measurement of pulse delay t_0 as a function of the absorbed pump power P_{abs} using best fit procedure. The jitter contribution arising from pump pulse rise front, can be determined as:

$$\delta t_0 = \tau_f \frac{\delta x}{1-x} = -\tau_f \frac{x}{1-x}\frac{\delta P_{abs}}{P_{abs}} \tag{4.16}$$

For a more accurate noise characterization, we need to consider that the pulse delay (or total build-up time) actually measured is:

$$\delta t_0^{rms} = \tau_f \sqrt{\left[\frac{x}{1-x} + \sqrt{\frac{\beta x}{2}}\right]^2 \left(\frac{\delta P_{abs}}{P_{abs}}\right) + \frac{\beta x}{2G^2}\left(\frac{\delta P_i}{P_i}\right)} \tag{4.17}$$

Where:

$$t_m = t_0 + t_b -> \delta t_m = \delta t_0 + \delta t_{b,1} + \delta t_{b,2} \tag{4.18}$$

$$\beta = \frac{t_R}{\tau_f}\frac{G}{g_{th}} \tag{4.19}$$

Equation (4.17) can be used to derive $\delta P_{abs/P_{abs}}$ and $\delta P_i/P_i$.

4.8 Experimental validation of the Jitter model

The new laser diode could be used as new pump laser diode. This diode laser is attractive because of the higher peak power with respect to the pump sources implemented in the previous designs described in Ch. (3). This property enables to investigate the reduction of the pumping time interval. Switching from a CW diode to a more powerful pulsed diode showed a significant improvement in terms of pulse-to-pulse time jitter. Thus, the new optical source was tested, prior to proceed with pump pulse compositing. Pump compositing is similar to the bleaching technique, but it operates on the gain of the active medium instead of the laser intracavity losses. The concept consists in reducing the amount of time to deliver the required energy in the gain medium necessary to trigger the passive Q-Switching. This is similar to a weak gain switching, shortening the total build-up time and inherent jitter. This must be done carefully if one needs to preserve SLM operation.

We performed several measurements on the SISRO PQS laser by varying the diode pump pulse peak power/ duration at a fixed pulse repetition rate of 1 kHz in order to investigate a “low-frequency” regime. At first, we characterized the delay time t_m between the pump pulse rise-front and the emitted laser pulse as a function of the absorbed pump diode peak power. In experimental conditions, given the relatively long pump pulse duration required

to reach the threshold (several tens of µs even at the maximum available pump peak power), it is reasonable to assume $t_m = t_0 + t_{b0}$. By fitting the measured data, it can be obtained a $P_{abs,th}$ of 1.15 W.

In order to caracterize the pulse-to-pulse time jitter and understand its dependance on the design parameters of the PQS laser, we performed a measurement of jitter as a function of absorbed pump peak power by varying the pump peak power and consequently adjusting the pump pulse duration to slightly exceed the total build-up time. Pulse timing jitter was measured as the standard deviation over 1000 recorded laser shots of the delay t_m between the pump pulse leading edge and the emitted laser pulse leading edge. This measurement was carried out for different laser diode peak power corresponding to different absolute values of t_m. This measurement was repeated several times for each pump pulse configuration.

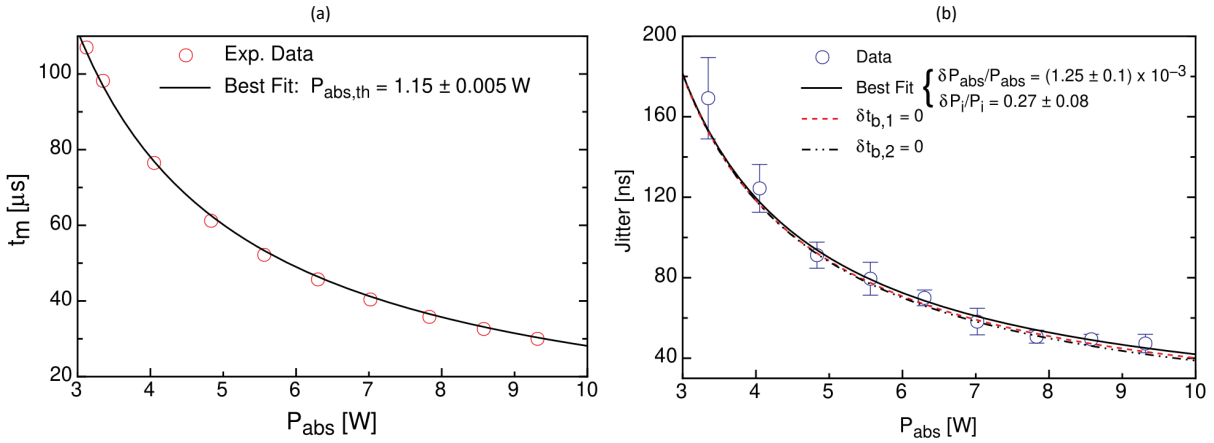

Figure 4.15: *Delay between pump pulse rise front and laser pulse emission as a function of the absorbed pump peak power (a) and Pulse-to-pulse time jitter as a function of the pulsed pump diode peak power. Red dots with corresponding error bars are the measured jitter (b).*

A remarkably low pulse-to-pulse time jitter of 47 ns, comparable to the pulse duration of 50 ns, was obtained at the maximum available absorbed pump peak power of 9.5 W (pump pulse duration of $\sim$ 35 µs). The measurements were fitted by means of equation (4.17). It turned out that the best fit procedure was very sensitive to $P_{abs,th}$ since understandably for low pump powers the logarithm function in (4.13) tends to diverge, however this parameter is independently and accurately determined as explained above. Eventually we can fit the data δt_m using only two independent parameters (noise sources): $\delta P_{abs}/P_{abs}$ and $\delta P_i/P_i$ (rms). Thus, increasing the pump power is clearly beneficial. It is also clear that the jitter contribution $\delta t_{b,1}$ and $\delta t_{b,2}$ are rather small, whereas δt_0 accounts for as much as 90% of pulse jitter in our experimental conditions.

Electronic feedback modulation of pump power, from time-to-current converter, or from pump power transmitted by laser crystal, should also help minimize pulse jitter which is presently mostly determined by $\delta P_{abs}/P_{abs} \sim 10^{-3}$ that is quite typical for commercial pump power supplies. Extrapolation from the fit curve suggests that doubling the pump pulse peak power should permit to further reduce the jitter of a factor about 2.5.

The model applies to low-frequency regime, where both laser pulse and gain dynamics complete before the next pump pulse, where everything restarts again in the new cycle.

However, we do observe a gradual jitter increase up to 150 ns for higher frequency than $1/\tau_f$ which we attribute to addition of noise from the previous cycle with that from the new pump cycle, thus offsetting jitter reduction allowed by high peak pump power.

4.9 SISRO laser achievements

The experiments on the SISRO and the related models derived were exploited to propose a novel single frequency laser source design, intended for both lidar (in particular HSRL and Coherent doppler lidars) and nonlinear optics applications. The SISRO technology for PQS SLM laser operation is an attractive design, emerging as an appealing and competitive laser source architecture. Summarizing the SISRO advantages:

- *System overall simplicity and all passive components:* The SISRO is composed by very few optical elements, excluding the pump system, are all passive. This design allows an overall system simplicity, leading to a higher reliability and lower overall unit system cost.
- *Reliable SLM operation and narrow bandwidth laser pulses generation:* SISRO technique has proven to be a viable way to stably produce narrow bandwidth, near Fourier transform limited pulses. It has been proven the generation of SLM pulses ranging from 30 ns to 150 ns, with relative laser spectra between tens of MHz and few MHz.
- *Sufficient seeding energy for MOPA systems:* The output pulse energy is between few tens and hundreds of μJ. These energies are suitable for easily seeding amplifiers in MOPA architecture, allowing to effectively boost laser signal, avoiding amplified spontaneous emission.
- *Pulse repetition rate:* SISRO design allows to reach pulse repetition rates relative to the inverse of gain medium lifetime, in accordance with SLM selective criterion. SLM operation with higher repetition rate can be still achieved, at expense of higher pulse-to-pulse time jitters.
- *Near diffraction limited laser beam:* Laser system is end pumped, meaning the superimposition between pump mode and cavity mode to achieve near diffraction limited beam quality.
- *Polarized laser output:* The use of birifrengent gain crystal or the implementation of PBS as output coupler are not strictly necessary for polarized laser output. Indeed the Cr^{+4}:YAG guarantees polarized laser operation, for anisotropic latency behavior.
- *Low Pulse-to-Pulse time jitter:* Passive Q-switching allows to emit laser pulses with stable energies. Using high peak power short pump pulse, it is possible to drastically reduce the pulse-to-pulse jitter.
- *Low Pulse-to-Pulse energy jitter:* Passive Q-Switching is intrinsically stable from a energy point of view due to its mechanism, if beam dimensions are kept constant in the active medium and the saturable absorber. Typically energy instabilities are lower than 1%.

Chapter 5

Infrared wavelengths extension through nonlinear optics

In this chapter it is described the access to infrared wavelengths by means of nonlinear optics light generation and amplification. This experience was conducted at KTH in Stockholm during a visiting period of 5 months. KTH is a renowned research center due to the vast experience for developing nonlinear complex systems and for design, growing and deploying the use of nonlinear periodically poled crystals. Conventional laser source are able to generate a set of discrete wavelengths relying on the transitions between energy levels of practically available active media, but the realization of specific crystal for desired wavelengths is not practically feasible. Instead of synthesizing new crystals, which possess opportune optical properties, the use of nonlinear device is far more appealing. It allows to use very well known high energy solid state laser source as pump systems to access new wavelengths through nonlinear devices. This allows to separate technological complexity in multiple stages, i.e., the pumping high energy system and the nonlinear device stage, with a possible nonlinear amplifier. This approach is appealing thanks to the possibility to tune nonlinear devices to multiple requirements. In this work it is investigated nonlinear parametric light generation by means of RPP-KTP (Rubidium Periodically Poled - KTP) crystals, to access 1.8-2.5 μm wavelengths in the nanosecond time domain. Optical source tunable in the 1.5–3.4 μm (SWIR) region are of interest for several fields such as spectroscopy [104], biology and medicine [105] and remote sensing [106, 107].

5.1 Nonlinear optics basics

Nonlinear effects can be divided into two categories: parametric and non-parametric effects. A parametric non-linearity is an interaction in which the quantum state of the nonlinear material is not changed by the interaction with the optical field. Then the process is ”instantaneous” and the energy as well as momentum are conserved in the optical field. The dielectric polarization density can be described by Taylor series expansion:

$$P(t) = P^L + P^{NL} = \epsilon_0(\chi^{(1)}E(t) + \chi^{(2)}E^2(t) + \chi^{(3)}E^3(t) + ...), \tag{5.1}$$

where the coefficients $\chi^{(n)}$ are the n-th-order susceptibilities of the medium, and the presence of such a term is generally referred to as an n-th-order nonlinearity. Note that the polarization

$P(t)$ and electrical field $E(t)$ are considered as scalar for simplicity. In general, $\chi^{(n)}$ is an $(n+1)_{th}$ rank tensor representing both the polarization-dependent nature of the parametric interaction and the symmetries (or lack) of the nonlinear material.

The P^L is the induced polarization with linear dependence on the electric field E. At low radiation intensity, the high order terms are negligible, on the contrary for growing intensities this is progressively not true.
The presence of an intense laser radiation causes the high order susceptibilities to become relevant. All optical phenomena involving $\chi^{(n)}$ of the n-th-order higher than 1 are identified as nonlinear phenomena P^{NL}.
The category of nonlinearities identified as "Parametric" is an instantaneous response based on the $\chi^{(2)}$ or $\chi^{(3)}$ of a medium. They give rise to effects such as frequency doubling, sum and difference frequency generation, parametric amplification and oscillation, and four-wave mixing. Parametric amplification and oscillation happen when two different radiations superimpose in the nonlinear medium. The two beams with different optical frequencies incident on the nonlinear crystal cause a polarization wave at the difference frequency. Provided that the polarization wave travels with the same phase velocity compared to the two incident waves, cumulative growth will be observed. The two incident beams are typically referred as "Pump" and "Signal", having frequencies ν_p and ν_s respectively. The radiation generated as difference frequency is called "Idler" with optical frequency $\nu_i = \nu_p - \nu_s$. Under proper condition (phase matching), the idler radiation and the signal radiation can grow at the expense of the pump wave, thus shifting pump energies $h\nu_p$ to Signal and Idler. Recalling energy conservation, it can be express:

$$h\nu_p = h\nu_s + h\nu_i \tag{5.2}$$

To achieve significant parametric amplification, it is required that each polarization wave travel at the same velocity as a freely propagating wave. This condition is met for refractive indices of the nonlinear material that satisfy the momentum conservation:

$$k_p = k_s + k_i \tag{5.3}$$

In case of collinear propagation, it can be described as:

$$n_p\nu_p = n_s\nu_s + n_i\nu_i \tag{5.4}$$

Where n_p, n_s and n_i are respectively the refractive indices at the three frequencies. It is referred as degenerate case when both idler and signal share the same optical frequency. Phase matching can be achieved by means of birefringence or periodic poling [108]:

- *birefringent phase matching:* is a technique for achieving phase matching of a nonlinear process by exploiting the birefringence of a nonlinear crystal. Phase matching can be divided in critical and non critical, depending on the position of the involved beams respect to the crystal axes of the index ellipsoid. Critical phase matching requires that the interacting beams are aligned at some angles respect to the crystal axes. The term critical indicates the sensitivity to misalignment of the beams. The acceptance angle is finite where critical phase matching works, thus it can be also referred as angular phase matching bandwidth. A intrinsic problem of critical phase matching is the spatial walk-off between the ordinary and extraordinary beams, which limits the

interaction length. Non critical phase matching, also referred to as temperature phase matching or 90° phase matching, is achieved when the two beams propagate along the same axis. The phase mismatch is minimized by adjusting the crystal temperature. The disadvantage of non critical phase matching is the need of relatively high temperature, which causes degradation of optical coatings and higher complexity compared to critical phase matching. Thus, the optical elements involved must be able to withstand the operation temperature.

- *Quasi-phase matching:* Firstly proposed in 1962 [109]. The use of a non homogeneous nonlinear crystal allows to periodically modulate the nonlinear properties of the nonlinear medium. Changing the nonlinear coefficient of the crystal allows to reverse the increasing mismatch during propagation. Thus, conversion is mainteined in the desired direction with an overall efficiency comparable to the birifringent phase matching. The small reduction in conversion efficiency (for the same nonlinear coefficient the d_{eff} is reduced of a factor $2/\pi$) allows to access to two important advantages. Firstly the beams involved in the process can share the same propagation and polarization, thus enabling to select the stronger nonlinear tensor. In second place, spatial walk-off is avoided.

5.2 Rubidium Periodically Poled KTP

The Potassium titanyl phosphate (KTP, $KTiOPO_4$) is the nonlinear material employed for wavelength extension. KTP belong to the ferroelectric materials category. Ferroelectrics are material which includes ferroics. In absence of applied fields the ferroics have a stable state. However the direction of such quantity describing the ferroics state can be reversed along the crystal axes if a sufficient strong field is applied. Ferroics can be exploited in multiple ways: for memory devices, sensores and for efficient nonlinear optical converter. KTP is a positive biaxial crystal. The crystal properties are [110]:

Nonlinear-optical coefficients (pm/V)	d_{31} = 6.5; d_{32} = 5.0; d_{33} = 13.7 d_{24} = 7.6; d_{15} = 6.1
Optical absorption (%/cm)	<0.6 (at 1064 nm)
Transmission range (μm)	0.35-4.5
Mohs hardness	~ 5
Melting point °C	~ 1150
Structure	orthorhombic

Table 5.1: *KTP crystal properties*

Due to the relatively high temperature, normal melt processes cannot be used to grow this material [110]. The most common technique to grow large single crystals of KTP are hydrothermal and flux techniques.

KTP has a combination of properties that makes it unique for nonlinear-optical applications, especially suited for Nd lasers pumping. KTP exhibit good mechanical and thermal properties, an high nonlinearity (d_{33}) and a high damage threshold. The combination of these properties with the high transparency makes it a optimal candidate for high energy and high average power nonlinear operation. For nanosecond pulses at 1 μm, the damage fluence is 10

J/cm^2 [111]. For nonlinear applications, it is useful to use the z-polarization, enabling to exploit the d_{33} nonlinear coefficient. The refractive index can be derived by Sellmeier equation [112]:

$$n^2 = A + \frac{B}{1 - C\lambda^{-2}} + \frac{D}{1 - E\lambda^{-2}} - F\lambda^2 \tag{5.5}$$

Where A, B, C, D, E, and F are specific to the material [112]. By applying an external electric field with opposite polarity to the natural polarization direction, if the electric field is greater tha $E_c \simeq 2kV/mm$ [113] then it is possible to invert the polarization. Periodically poled structures in KTP crystals with a thickness of up to 3 mm have been reported, but it has been also demonstrated that the limitations of KTP can be overcome by employing Rb-doping [114], enabling to access greater thickness. The rubidium ions can replace the potassium ions in the crystal structure. At low Rubidium concentration (<0.3%) the optical properties of the crystal are unchanged. The positive effect of Rubidium ions is the lowering of ionic conductivity, yielding to a reduction of domain broadening during electric field poling [115]. Rb-doped KTP crystals are also promising materials for fabrication of sub-μm periodically poled samples.

5.3 Optical Parametric Oscillators

The optical parametric generation is indicated as OPG. OPG differs from OPA because it is assumed no seeding, i.e., OPG is achieved when two laser radiation are totally generated by the pump field. Assuming a QPM nonlinear medium, the phase matching condition can be expressed as:

$$\Delta k = k_p - k_s - k_i - k_{QPM} \approx 0 \tag{5.6}$$

The signal and idler grow exponentially with the interaction length inside the nonlinear medium, if (5.6) is true. To increase the conversion efficiency the nonlinear medium can be placed inside an optical cavity, thus leading to a Optical Parametric Oscillator OPO. The cavity is resonant to one of the two generated/amplified waves at least. A parametric gain can be introduced [59].

$$g = \sqrt{\kappa I_p} \tag{5.7}$$

I_p is the pump flux and κ is a coupling constant:

$$\kappa = \frac{8\pi^2 d_{eff}^2}{\lambda_i \lambda_s n_i n_s n_p \epsilon_0 c} \tag{5.8}$$

The effective gain can be rewrote to consider a phase mismatch Δk_m:

$$g_{eff} = \left[g^2 - \left(\frac{1}{2} \Delta k_m \right)^2 \right] \tag{5.9}$$

For a singly resonant OPO (SROPO) the threshold condition is given by:

$$g^2 l^2 = 2\sqrt{1 - R_s}(1 - L) \tag{5.10}$$

Where R_s is the output coupler reflectivity for signal, l is the crystal length and L are the cavity intrinsic losses. The signal noise is amplfied in each transit meanwhile the pump radiation is still present in the nonlinear crystal with significant power. The pump flux required to reach threshold for a SROPO is: [59]

$$I_{th} = \frac{1.12}{\kappa g_s l_{eff}^2}\left(\frac{l_{cavity}}{t_p c} ln\frac{P_s}{P_n} + 2\alpha l + ln\frac{1}{\sqrt{R_s}} + ln2\right)^2 \tag{5.11}$$

The g_s is the signal spatial mode coupling coefficient, which indicates the overlap between the optical pump and the cavity mode supported:

$$g_s = \frac{1}{1 + (w_s/w_p)^2} \tag{5.12}$$

The signal and pump spot size are indicated by w_s and w_p respectively. The l_{eff} is the effective nonlinear crystal length. For QPM crystal the total length is equal to the effective length, because of no spatial walk-off. The first term in the bracket indicates the induced losses due to build up time to raise signal power from noise level. It is reported in literature that the best agreement between this model and experimental data is for a increase of 10^{14} times, i.e., $ln(P_s/P_n) = 33$. The logarithmic term is divided for the number of roundtrip necessary to reach P_s. Then, the use of a short cavity and a longer pump pulse lowers the threshold. The second term indicates the amount of absorption and the third term output coupling loss, which depends on R_s. The last term is due to SROPO operation. The pump intensity is a critical parameter, beacuse it determines the efficiency of the OPO. For plane waves model the efficiency can be described as:

$$\eta = sin^2 gl \tag{5.13}$$

Thus, the total conversion can be theoretically achieved for:

$$I_p/I_{th} = (\pi/2)^2 \tag{5.14}$$

Assuming a more realistic situation, with a gaussian shape for the pump beam, the maximum efficiency achievable is $\sim 71\%$ [59]. In order to enhance efficiency of a OPO it is necessary to increase the ratio P/P_{th}. After reaching the optimal ratio the efficiency drops slowly and damage threshold consideration become the most important upper bound limitation.

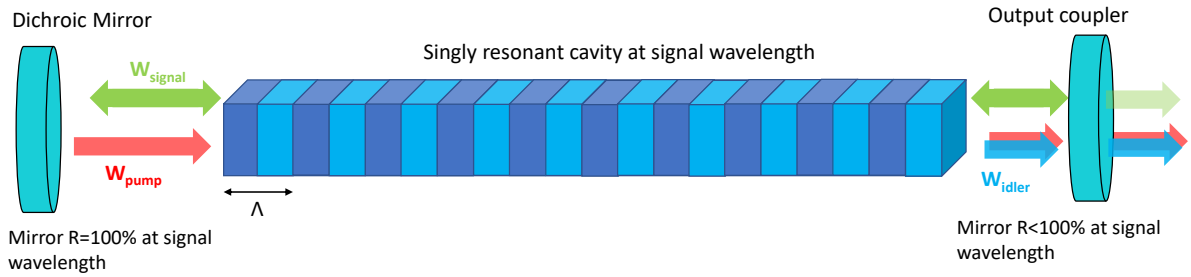

Figure 5.1: *SROPO strucure showing a plano-plano cavity layout.*

An important characteristic of OPO systems is that the frequency linewidth of the generated fields is broad (tens of nm). This is due to pumping very far above threshold which allows

several longitudinal modes to oscillate. In order to achieve narrow linewidths, OPOs require seeding or intracavity filtering. OPO technology is widespread in multi-stage laser systems, the advantages of this architecture is the possibility to enhance beam quality, efficiency and spectral behavior at the cost of higher complexity compared to Optical Parametric Generators (OPG). The main disadvantage of this technological is the overall complexity, the high cost of the optical elements required due to ad-hoc coating and optical damage resilience.

5.4 Backward-Wave Optical Parametric Oscillators

A special category of OPO is the backward-wave OPO (BWOPO) also referred as Mirrorless OPO (MOPO). In this typology of oscillators, one (signal or idler) of the two generated waves is counterpropagating respect to the pump wave. Then, the distributed feedback along the nonlinear medium allows to achieve a self seeding regime without the need of a cavity. The BWOPO also introduces other significant advantage, which is simplicity. The system does not require any cavity to operate, drastically enhancing system reliability and reducing the costs too. In order to realize a BWOPO, the phase matching imposes a strong constrain on the grating, indeed it is required to realize very short grating periodicities, on the order of the pump wavelength for first order QPM. To exploit correctly this technique the pump pulse must be two times longer than the required time to travel the crystal. Momentum and energy conservation relations are:

$$k_P = k_f - l_b + l_{QPM} \tag{5.15}$$

$$\nu_P = \nu_f + \nu_b \tag{5.16}$$

Where the indices p, f, b stand for pump, forward and backward respectively.

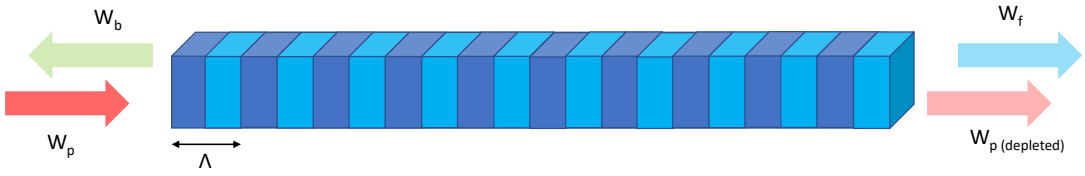

Figure 5.2: *BWOPO structure of the periodically domain-inverted ferroelectric crystal and vector diagram of counterpropagating waves.*

Indicating the ν_f and ν_b as the forward wave and backward wave, then the grating periodicity can be related to pump pump, signal and idler wavelengths and refractive indices.

$$\frac{1}{\Lambda} = \frac{(n_p - n_f)}{\lambda_p} + \frac{(n_b + n_f)}{\lambda_b} \tag{5.17}$$

For a periodicity $\Lambda > \lambda_p/n_p$ the backward wave is idler, whereas for $\Lambda < \lambda_p/n_p$ the backward wave is signal. The degeneracy case is for $\Lambda = \lambda_p/n_p$. BWOPO has very interesting spectral

properties. The forward field is a copy of pump wave at a different frequency whereas the backward wave is inherently narrowband [116]. Indeed considering the derivatives between the involved optical frequecies:

$$\frac{\partial \nu_f}{\partial \nu_p} = \frac{v_{gf}(v_{gb} + v_{gp})}{v_{gp}(v_{gb} + v_{gf})} = 1 + \epsilon \tag{5.18}$$

$$\frac{\partial \nu_b}{\partial \nu_p} = \frac{v_{gb}(v_{gp} - v_{gf})}{v_{gp}(v_{gb} + v_{gf})} = -\epsilon \tag{5.19}$$

Where $v_{gi} i = (p, f, b)$ is the waves group velocities, and ϵ is a dimensionless parameter which characterized the difference in group velocity. Considering the low dispersion and the temporal regime the $|\epsilon|$ is negligible, i.e. $\epsilon << 1$. The optical phases are linked by the following relation:

$$\phi_p - \phi_f - \phi_b = -\frac{\pi}{2} \tag{5.20}$$

Considering $\epsilon \approx 0$ the phase derivatives for the nonlinearly generated waves are:

$$\frac{\partial \phi_f}{\partial t} \simeq \frac{\partial \phi_p}{\partial t} \tag{5.21}$$

$$\frac{\partial \phi_b}{\partial t} \simeq 0 \tag{5.22}$$

Then the BWOPO exibiths astonishing spectral performance as optical parametric system, without any auxiliary radiation or filtering element. The forward radiation is a spectral copy of the pump wave, whereas the counter propagating radiation is transform limited. For the BWOPO the pump threshold is [117]:

$$I_{P,th} = \frac{c\epsilon_0 n_p n_f n_b \lambda_f \lambda_b}{2L^2 d_{eff}^2} \tag{5.23}$$

where c is the speed of light in vacuum, ϵ_0 is the permittivity of free space, n_i are the refractive indices, λ_i are the backward and forward wavelengths, L is the crystal length and d_{eff} is the effective quadratic nonlinearity. The BWOPO represents a suitable substitute for the relatively complex OPO. In this work it is investigated a BWOPO system in the nanosecond domain, in order to compare the advantages and disadvantages compared to a conventional OPO.

5.5 Experimental setups

The project realized at KTH (Stockholm-Laser Physics department) consisted in the realization of two different MOPA systems based on RPP-KTP crystals. The stages were respectively two parametric seeders, amplified by means of parametric amplification, exploiting the same high energy optical pump source. THz generation is an additional stage of the project, which it is considered to be developed in the near future. The THz gap is the spectral region between 0.3 THz and 10 THz. This region is extremely hard to access due to the lack of efficient sources and receivers, but it is of great interest for several applications. [118, 119, 120, 121]

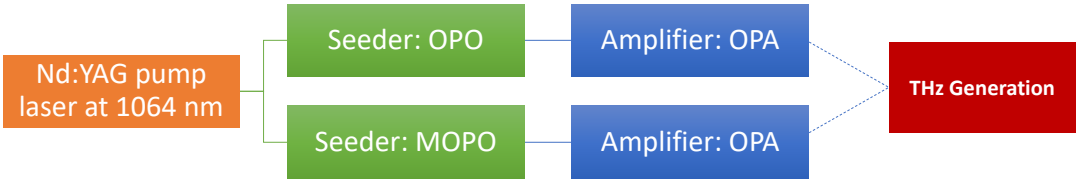

Figure 5.3: *Optical setup scheme.*

The Nd:YAG Q-Swtiched laser is used as optical pump for all the nonlinear devices. The system is able to generate high energy pulses of 170 mJ, at 1064 nm with pulse duration of 11-12 ns. The pump radiation is filtered in polarization, enabling a reasonable beam quality for 150 mJ pulses. The two seeders realized are an OPO standing wave architecture and a MOPO device. The two system are compared in terms of conversion efficiency, stability, complexity and emitted spectra. The two amplifiers enable to boost energy to tens of mJ energies. In the future the two parallel MOPAs are meant to realized a THz wave by means of nonlinear Difference Frequency Generation (DFG) in suitable materials. The optical elements which compose the OPO, BWOPO and OPAs are shown in the Fig. (5.4).
The setup is complex, but it can be easily decomposed in 6 blocks:

- *Pump system:* An unstable Nd:YAG Q-Switch laser, which longitudinally pump all the nonlinear devices. The output beam is $\approx$ 5x5 mm^2, enabling a very long Rayleigh range or collimated beam path.
- *Splitter:* The firt series of optics are used to enhance the polarization ratio between the two beam axis and to divide the pump radiation in separate independently channels.
- *OPO seeder:* The OPO is composed by optics for pump imaging, the cavity (Plano-Concave, Standing Wave architecture). The nonlinear crystal is a 5x7x12 mm^3 KTP crystal AR coated, with poling period of 38.85 μm. After the cavity dichroic mirrors are used to separate the desired radiation.
- *BWOPO seeder:* The BWOPO hosts a series of optics for both pump and signal imaging, due to the counterpropagating nature of the signal radiation. The BWOPO similar to the OPO uses dichroic mirrors to separate the desired radiation. The BWOPO crystal is 3x1x7 mm^3 KTP crystal uncoated, with poling period of 500 nm.
- *OPO amplifier:* A longitudinal optical parametric amplifier uses KTP crystals with AR coating and poling period of 38.85 μm to amplify the OPO seed radiation.
- *BWOPO amplifier:* A longitudinal optical parametric amplifier uses KTP crystals with uncoated surfaces and poling period of 38.5 μm to amplify the BWOPO seed radiation.

Seeders and Optical Parametric Amplifier do not include delay stages because of the layout, the spatial walk-off between seeder and amplifier was limited to few cm. Operating with pulse in the nanosecond regime (1-10 ns), the pulse spatial length ranges from 30 cm to 3 m.

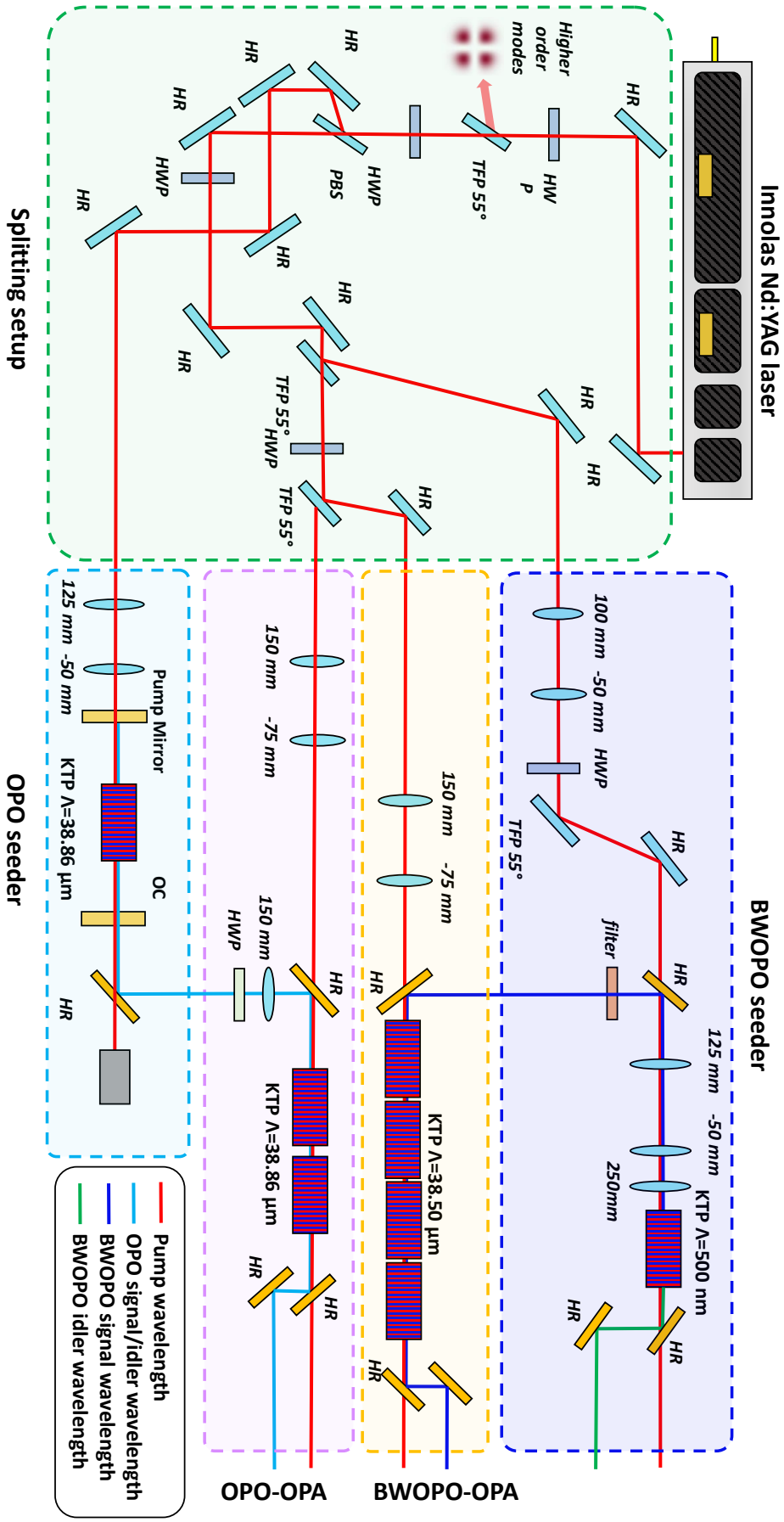

Figure 5.4: *Optical setup displaying any elements.*

5.5.1 Nd:YAG High energy pump laser

The optical pump laser is an actively Q-switched Nd:YAG laser, emitting at 1.064 µm. The laser is a Innolas Spitlight produced by InnoLas Laser GmbH. The laser delivered Gaussian pulses with an available energy of 170-180 mJ with repetition rate of 100 Hz and a pulse duration of 11-12 ns (FWHM). The laser was injection-seeded with a distributed feedback fiber laser in order to strengthen single longitudinal mode operation and to secure wavelength stabilization. The power stability of the laser was measured to have an rms value of 0.3%. Exploiting a polarized beam splitter, 15 mJ of pulse energy is separated from the useful radiation. The splitted component shows a strong multimodal beam quality, a Hermite-Gaussian mode $\mathrm{TEM}_{(1,1)}$. The filtered radiation is then measured. The beam quality is obtained by means of the 4-Sigma Diameter method with the aid of a camera. The analysis revealed a $M_x^2 = 6.14$ and a $M_y^2 = 2.80$, for an overall average of $M^2 = 4.14$. The intensity distribution has been deeply investigated during each imaging procedure in order to determine the maximum peak intensity in each critical device. Between the sagittal and tangential plane there is a relatively small focal plane shift of 10 mm.

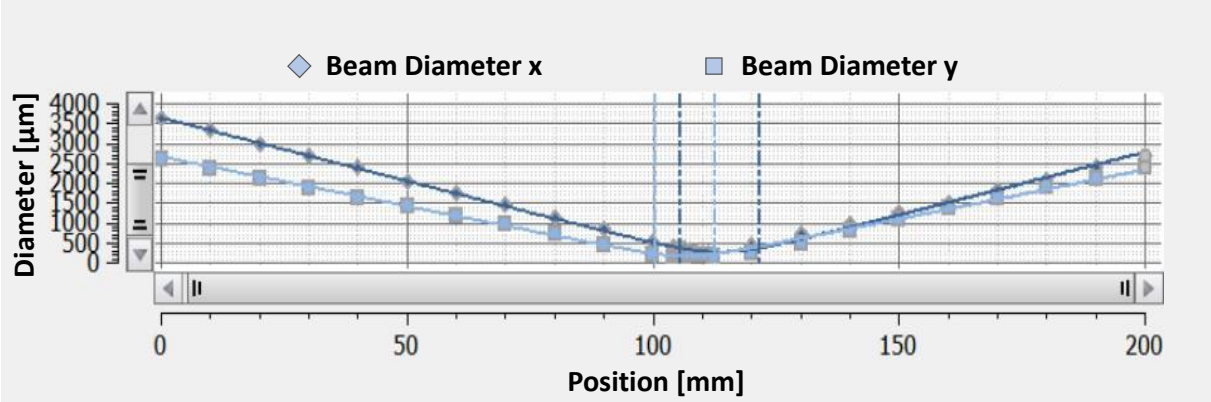

Figure 5.5: *Pump laser beam quality.*

The beam point stability and the beam shape were sensitive to temperature. Then, after polarization filtering the useful pulse energy amounts to 150-155 mJ. The beam shape exhibits a strong center with hot spots. Considering the high energies involved, optical induced damage must be experimentally or numerically obtained.

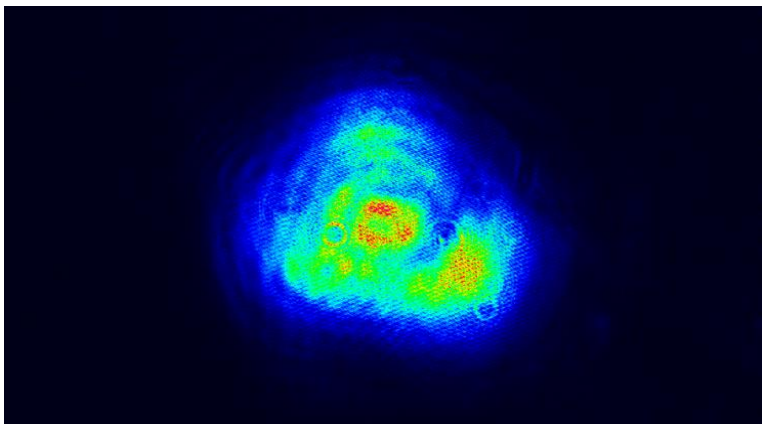

Figure 5.6: *Pump laser beam shape.*

5.5.2 Singly Resonant Optical Parametric Oscillator

In order to design an OPO, a good beam overlap between pump and cavity mode should be achieved. An high intensity is also a important parameter to enhance conversion efficiency. The good beam overlap between the pump laser mode and the cavity mode enables to extract from the cavity a signal/idler radiation with high spatial quality. Achieving high intensities allows to access higher conversion efficiency, though too high intensities can lead to severe optical damages. A trade-off must be realized, because in order to increase energy extraction, the cavity mode should be enlarged, but this action requires to extend the laser cavity, decreasing the conversion efficiency. It can be exploited a larger volume at expense of the output beam quality as sub-optimal approach to boost energy scaling. Energy extraction scaling can be ideally enhanced exploiting longer crystals (to avoid any non-converting region inside the OPO) and suitable curved mirrors to optimize the pump beam overlap with the fundamental mode. Practically, the pump mirrors operating at exotic wavelengths (especially dichroic mirrors) are expensive and require several weeks if not months to be delivered, making the optimization of the cavity challenging in practice.

The cavity realized was 3.5 cm long; the nonlinear crystal was a 5x7x12 mm^3, AR coated Rubidium doped PPKTP, the poling period was 38.85 μm to achieve degenerate type-0 down-conversion from 1.064 μm. The dichroic mirror is a HT at 1064 nm and HR at 1800-2600 nm with curvature radius r=150 mm. The output coupler was reflective at 1800-2600 nm with R=50% and R=1% for 1064 nm. The simulated OPO cavity reveals around 200 μm mode radius in the nonlinear material, as shown in Fig.(5.7).

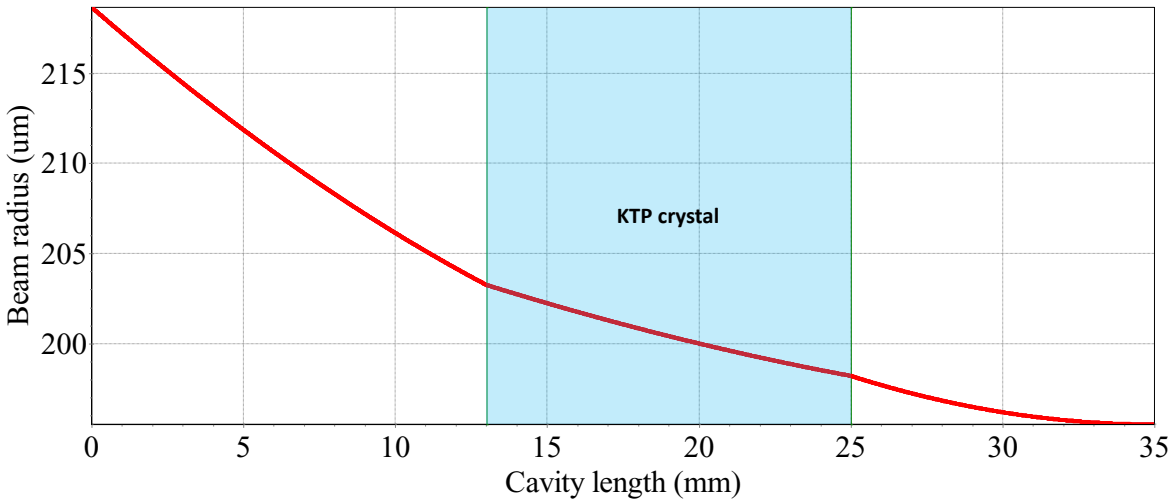

Figure 5.7: *OPO ABCD simulation, red line describes for the fundamental mode, the colorized region indicates the KTP region.*

The pump beam must be matched to the cavity mode in the crystal in order to excite the fundamental mode. In this regards a beam telescope and a CCD have been employed to observe the effective pump waist and quantify pump fluence in the crystal region. The optics employed for the telescope are two spherical lenses because the pump radiation shows a relatively small astigmatism. A small tilt of the lenses was sufficient to introduce an effective asymmetrical focusing action, enabling to avoiud cylindrical lenses. The focal lengths employed are f_1=125 mm and f_2=-50 mm, yielding a telescope reduction of 40% for the

incoming pump beam. The pump beam is collimated inside the cavity crystal region. The beam is directly inspected after the OPO dichroic mirror to observe the intensity profile and to quantify the peak intensity achievable. This technique is mandatory to prevent optical damages and optimize the pump beam for the OPO. The beam shape is quite structured, requiring a deep analysis to be described. Indeed the use of different filters allows to identify the ”wings” and the ”head” of the pump beam. The camera saturation indicates that the largest amount of energy is contained in the central peak. Indeed, the pump radiation has a very sharp energetic center with a complex surrounding pattern.

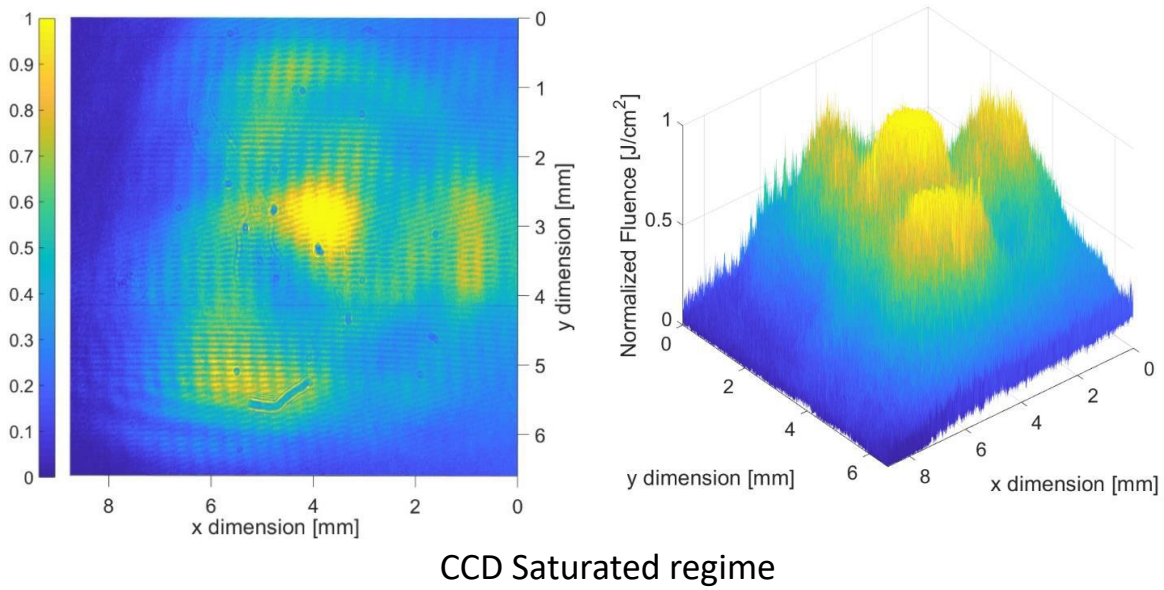

Figure 5.8: *Pump beam before the optical telescope, the CCD is saturated in the center. On the left the 2D image of the beam and on the right the 3D replica.*

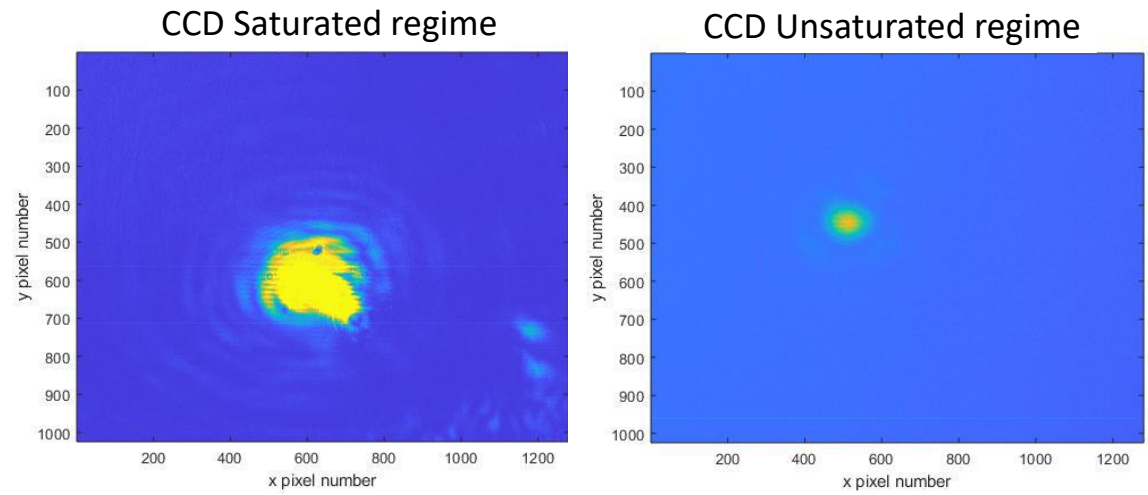

Figure 5.9: *Pump beam after the optical telescope. On the left the CCD saturated regime to describe the ”wings”, whereas on the right the beam hot spot is revealed.*

In order to define the damage threshold we considered that the central spike of the pulse observed with the CCD (camera DCC1545M) contains all the measured energy. Each pixel corrdisponds to 5.2 μm x 5.2 μm. This analysis describes the worst case scenario, enabling to rapidly address a safe operating zone.

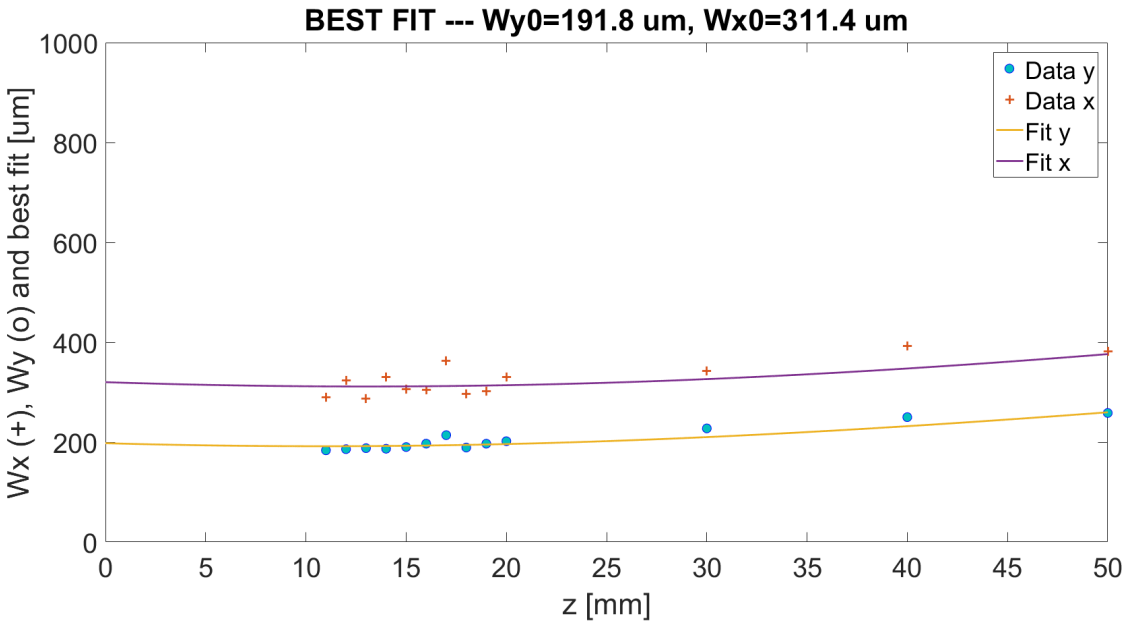

Figure 5.10: *Pump beam radii evolution of the most energetic component of the pump beam. The beam radii are estimated and plotted versus the position on the propagation axis.*

It is clear that in the crystal region the pump beam width is nearly constant. Then, it can be inspected the beam hot spot in detail, in order to address the damage threshold issue.

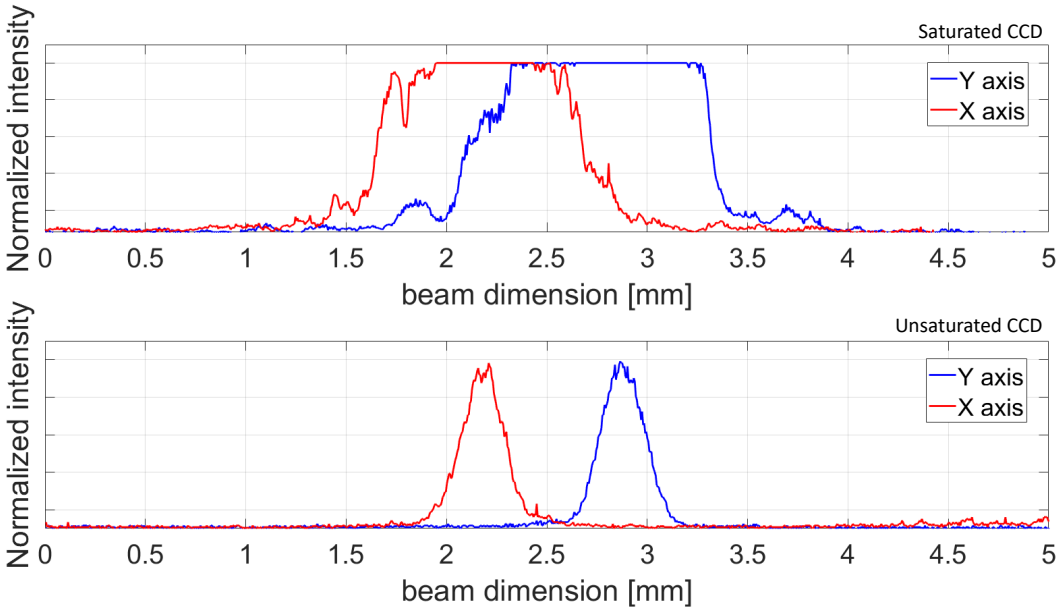

Figure 5.11: *Pump beam dimension and shape inside the OPO cavity, red and blue describe the two orthogonal axis for the beam.*

The damage fluence for all the optical elements employed is around $\sim 10\ J/cm^2$.

$$F_{gaussian} = \frac{2E}{\pi w^2_{gaussian}} \tag{5.24}$$

Experimentally we used a dummy KTP crystal to verify this method for the optical damage, displaying good agreement with Eq. (5.24) related to the most energetic component of the pump beam.

Analyzing the pump energy peaks, the most energetic part of the beam has $w_x \simeq 310\ \mu m$ and $w_y \simeq 190\ \mu m$. The beam is collimated inside the OPO cavity. Exploiting the dummy crystal we observed that 5.5 mJ is the maximum tolerable energy. This value is consistent with a beam radius of 200 μm. For higher incident energies than 5.5 mJ, the cavity experiences optical damage. Indeed, recalling equation (5.24) the corresponding fluence is close to 10 J/cm^2.

5.5.3 Experimental results

The OPO was aligned exploiting the green radiation, generated by Second Harmonic Generation. Once aligned, the cavity emitted red radiation useful to identify the start of the oscillation.

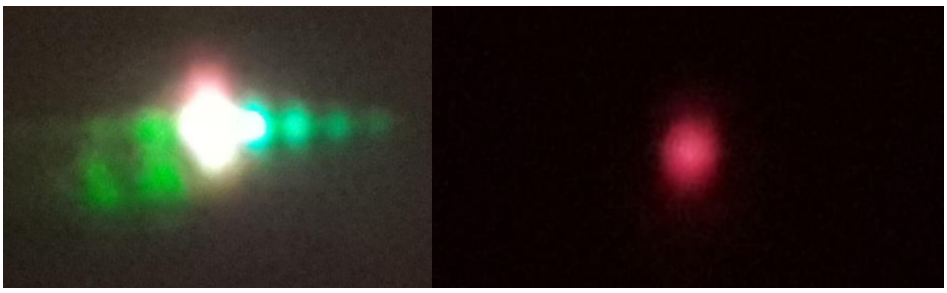

Figure 5.12: *OPO visible radiation generation before and after filtering. Red radiation is obtained with one pump photon and one signal photon.*

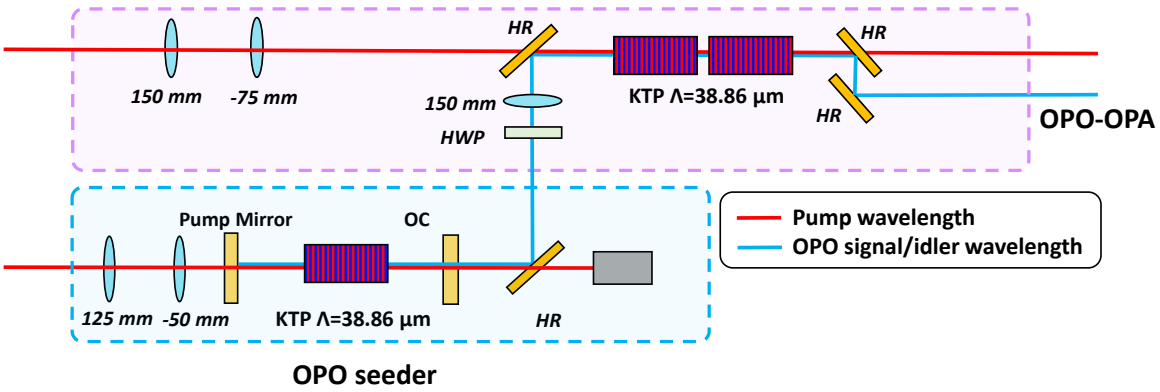

Figure 5.13: *Detail of Fig.(5.4), system setup showing the OPO and the OPA. The pump mirror is a curverd mirror with r=150 mm and the OC has R=0,5. The useful radiation is selected by means of dichroic mirrors.*

The laser beam shape emitted by the (SR)OPO is directly measured by means of a pyrocamera, (Spiricon bandwidth: 13nm-355nm and 1.06-3000µm, Each pixel is 80x80 μm^2). The signal is isolated by means of a dichroic mirror and collimated with a CaF lens.

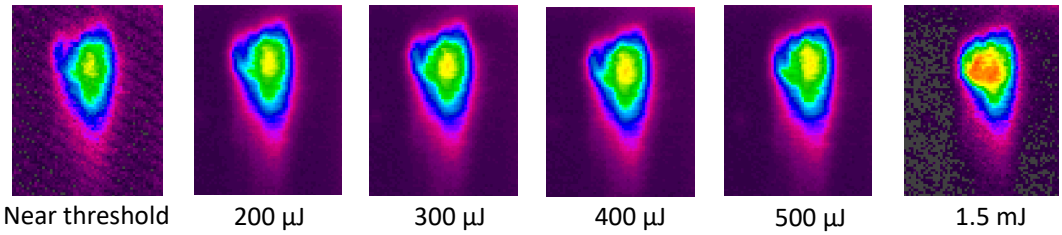

Figure 5.14: *Beam shape for different output pulse energies.*

The pulse duration is of only 7 ns. The pulse width is shorter than the pump pulse width because of the required intensity threshold to trigger the nonlinear process. The conversion efficiency of the OPO realized is high, reaching a 43 % for 3.5 mJ pump pulse energy. This was the maximum pumping energy we used in order to avoid optical damage of the crystal.

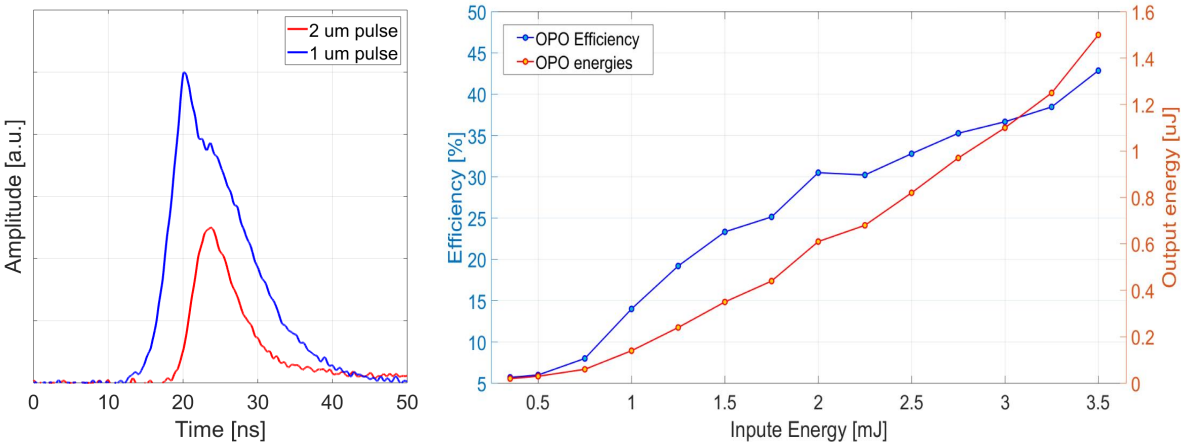

Figure 5.15: *On the left the comparison between the temporal depleted pump shape and the induced parametric temporal shape. On the right the OPO conversion efficiency.*

The signal beam dimension after the CaF lens has an overall beam dimension $2w_x$=2.3 mm and $2w_y$=3 mm, which is comparable to the pump beam after the telescope with magnification x0.5. To achieve these dimensions out of the optical cavity the M^2 is calculated to be $M_x^2 = 7$ and $M_y^2 = 5.5$, considering as initial beam dimensions the pump radii realized in the crystal region, Fig. (5.16). The output beam quality is comparable to the pump M^2.

It should be noticed, that the signal beam shape is far cleaner shape compared to the pump beam shape. The amplification arm used 0.8 mJ seeding energy for amplification. An HWP was used to optimize the polarization matching between pump radiation and signal radiation. The amplification crystals were 12 mm long KTP Periodically Poled crystal with the same periodicity of 38.86 μm and surface AR coating.

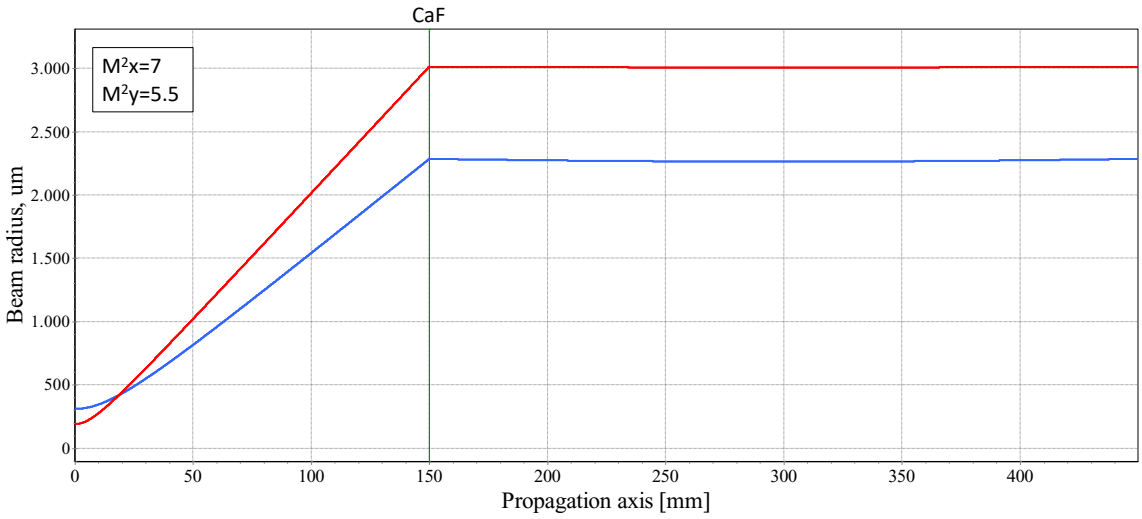

Figure 5.16: *Output beam quality simulation*

The OPO output is superimposed with the pump radiation along the OPA region. Amplification tests were conducted with one crystal and two crystals with identical features. In Fig. (5.17) is presented the amplified pulse energy measured after the dichroic mirror.

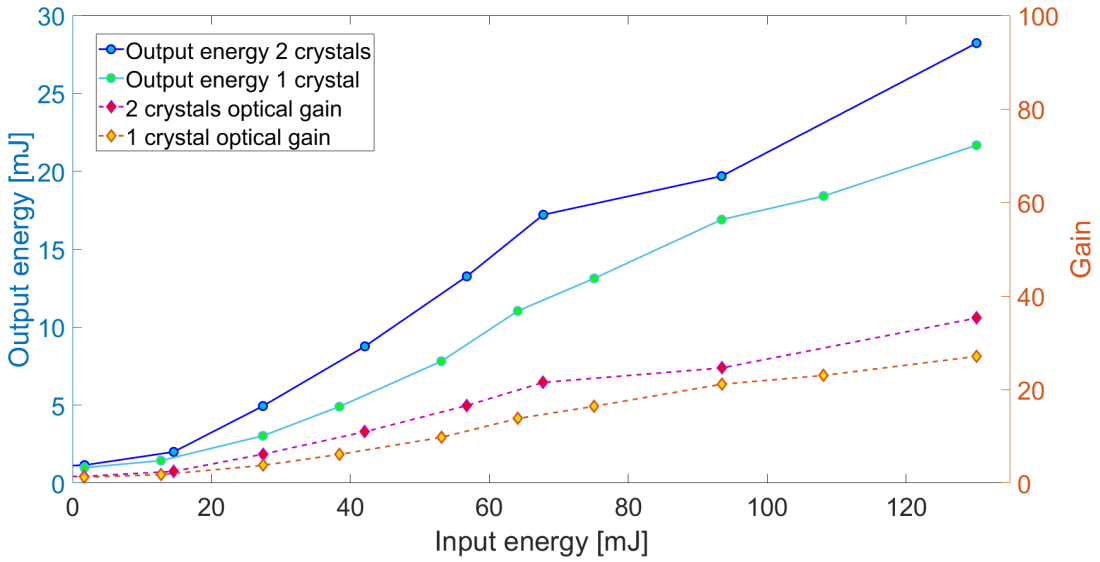

Figure 5.17: *OPA output pulse energy and amplifier gain.*

The maximum gain and conversion efficiency are respectively 35 and 21% employing two amplification KTP crystals. The gain G and conversion efficiency η_{amp} are derived as:

$$G = \frac{E_{output}}{E_{seeding}} \tag{5.25}$$

$$\eta_{amp} = \frac{E_{output}}{E_{input}} \tag{5.26}$$

The depleted pump power is significant during the amplification process, thus indicating that further amplification can be achieved employing longer interaction lengths, such as longer

crystals or more crystals. A more efficient approach would be to maximize the intensity at each amplification stages, but this technique would require to engineer each stage with dedicated optics. In this test, more than 50% of the pump energy is not converted. It must be remembered that down conversion can generate a conversion plateau if the signals photons are too numerous compared to the pump photons in a given spatial region.

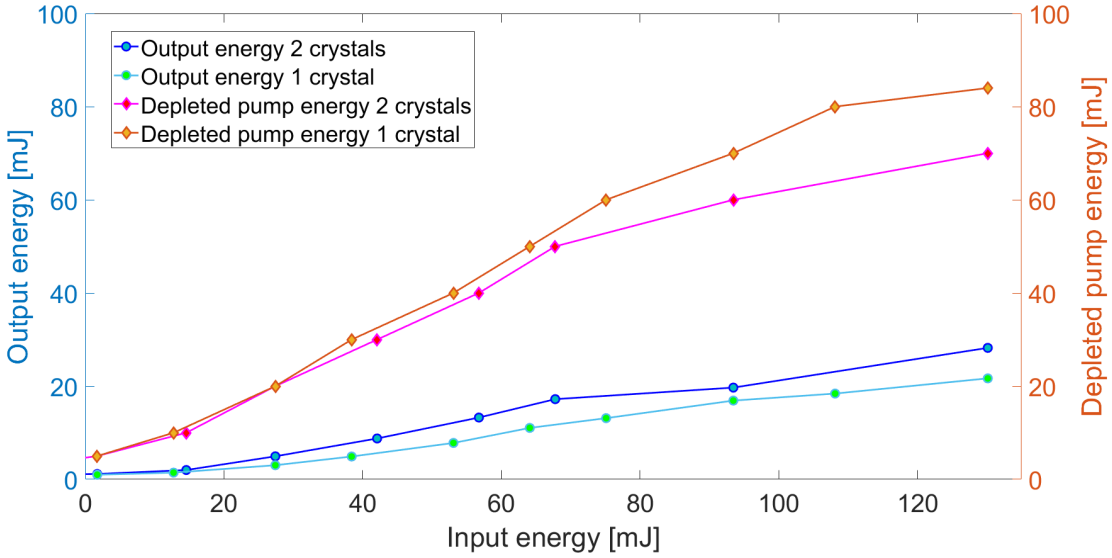

Figure 5.18: OPA output energy and pump depleted energy.

Then, the depleted pump radiation can be still used, creating the possibility to further increase the overall system efficiency. The critical disadvantage of the OPO is the output spectrum. The absence of seeding or intracavity frequency-selective components prevent to control the spectral performance of the device, resulting in poor spectral purity.

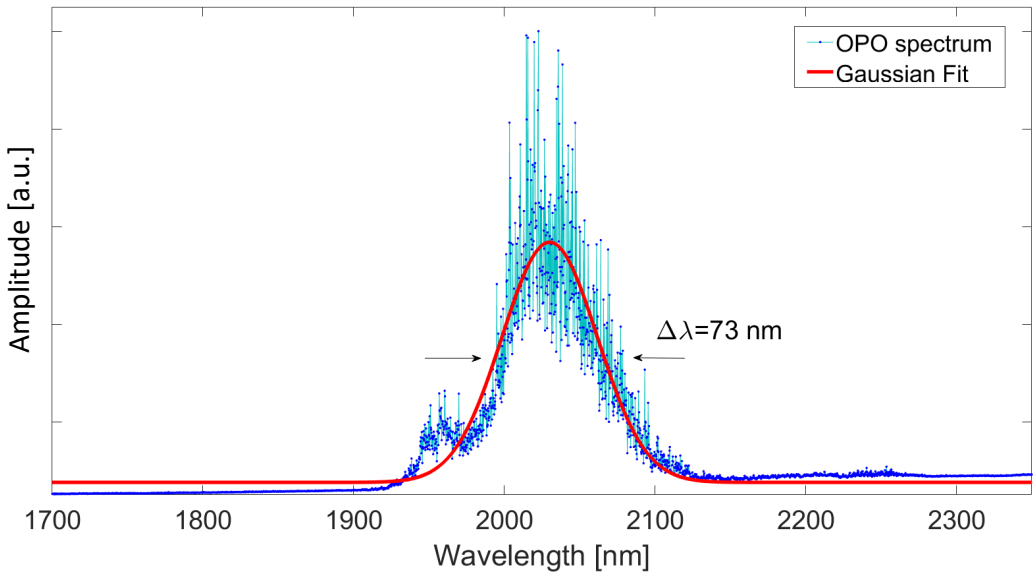

Figure 5.19: *OPO emitted spectrum.*

In order to reduce the optical bandwidth emitted a Bragg Reflector is placed instead of the output coupler (cavity plane mirror). The reflectivity (diffraction efficiency) of the Bragg

grating is of R=50%±10% and the reflective bandwidth is 1 nm. The threshold damage is comparable to the other optical components.

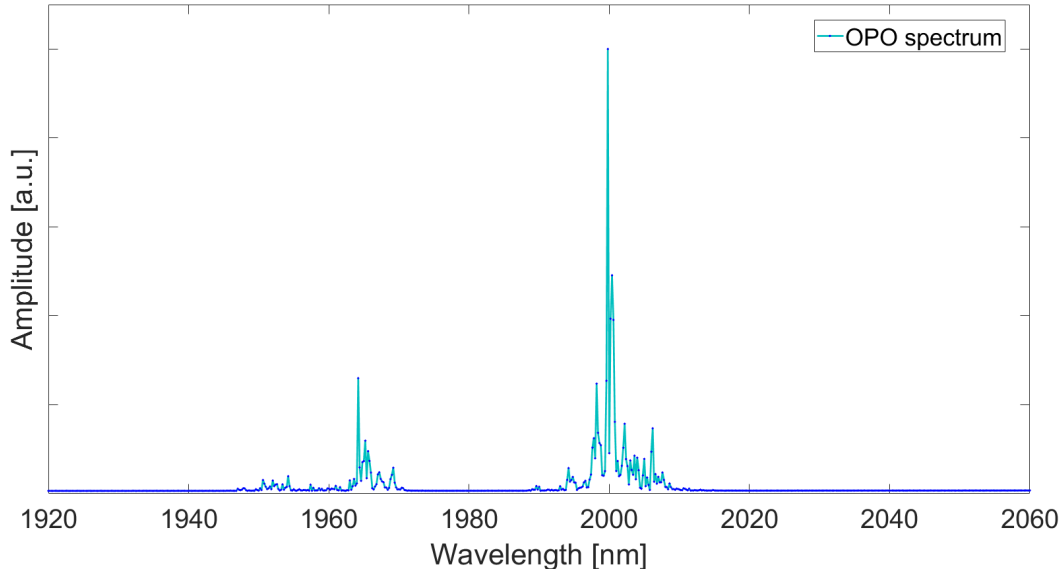

Figure 5.20: *OPO emitted spectrum with Bragg Grating Output Coupler.*

Solid state Bragg gratings are able to drastically reduce the optical spectrum by narrowing the gain bandwidth which can experience oscillation. However, Bragg grating are not attractive because of the high cost per unit and a high sensitivity to alignment.

5.5.4 Backward-Wave Optical Parametric Oscillator

The BWOPO (or MOPO) crystal has an effective grating of 3x1x7 mm^3 uncoated, which is realized inside a KTP crystal of 5x1x12 mm^3. The pump beam diameter is reduced propagating through a first telescope with magnification x0.5, after that a splitting arm is encountered in order to carefully control the amount of energy which is delivered to the crystal. This extra splitter is intended to protect the BWOPO before each operation, because of the extremely valuable manufactured crystal.

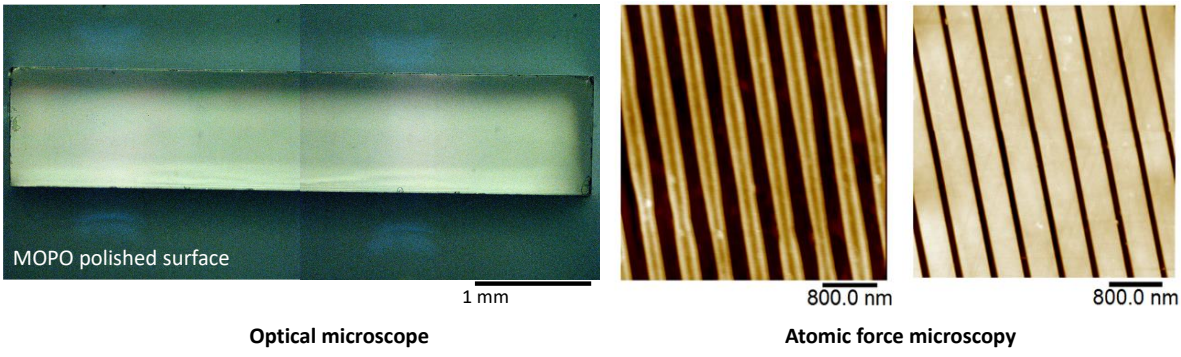

Figure 5.21: *BWOPO crystal polished surface and grating period.*

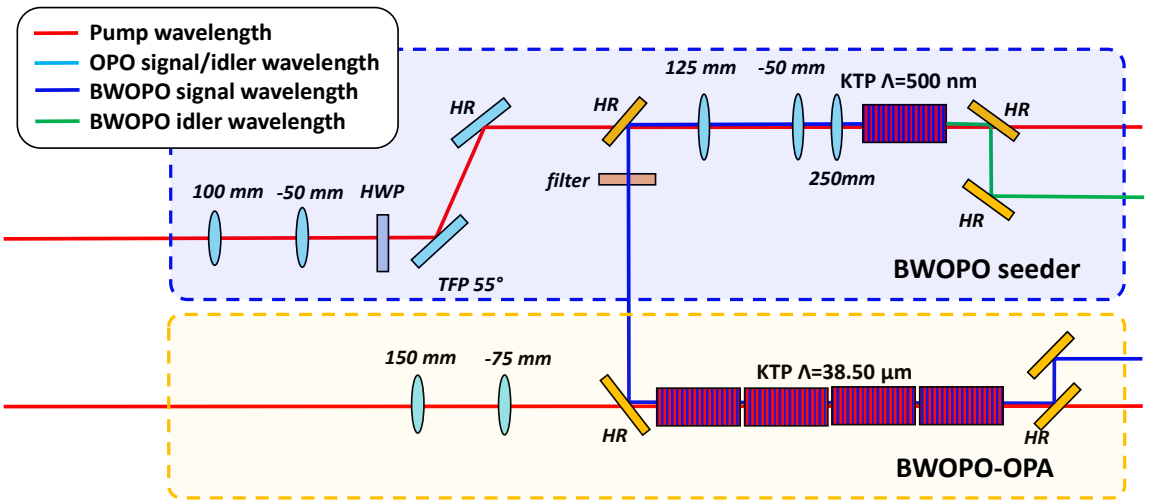

Figure 5.22: *Detail of Fig.(5.4), BWOPO seeder and BWOPO-OPA architecture.*

The pump beam diameter is further reduced and then focused in the crystal region. The optics are a couple of spherical lenses of 125 mm and -50 mm, followed by a CaF spherical lens of 250 mm focal length.

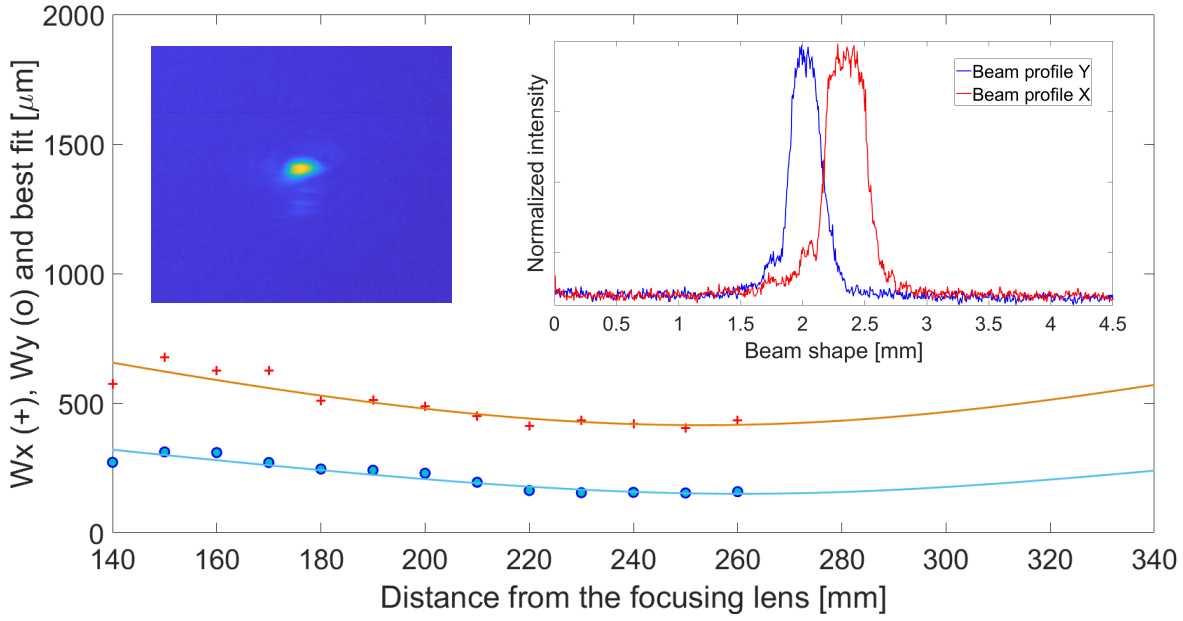

Figure 5.23: *Most energetic componenet of the pump beam for BWOPO imaging.*

The lenses have been placed after the dichroic mirror for two specific reasons. Firstly to avoid optical damage to the mirror and secondly to allow to re-image the generated signal beam in the OPA. The pump beam radii realized are comparable to the smaller dimension of the poled region, i.e., 1 mm. Second but not less important, the pump beam has to propagate along the crystal without crossing the crystal poled region. Then:

$$2Z_{r,pump} = 2\pi \frac{w^2}{\lambda M^2} > l_{BWOPO} \tag{5.27}$$

The damage threshold is then numerically derived and subsequentally tested with a dummy crystal revealing a maximum pump energy of 6 mJ. 6 mJ are transmitted throug a series of uncoated optics and surface, i.e., the uncoated lenses and the BWOPO input face. Then the effective maximum is 4.66 mJ. The energy characterization is showed in Fig. (5.23-5.24).

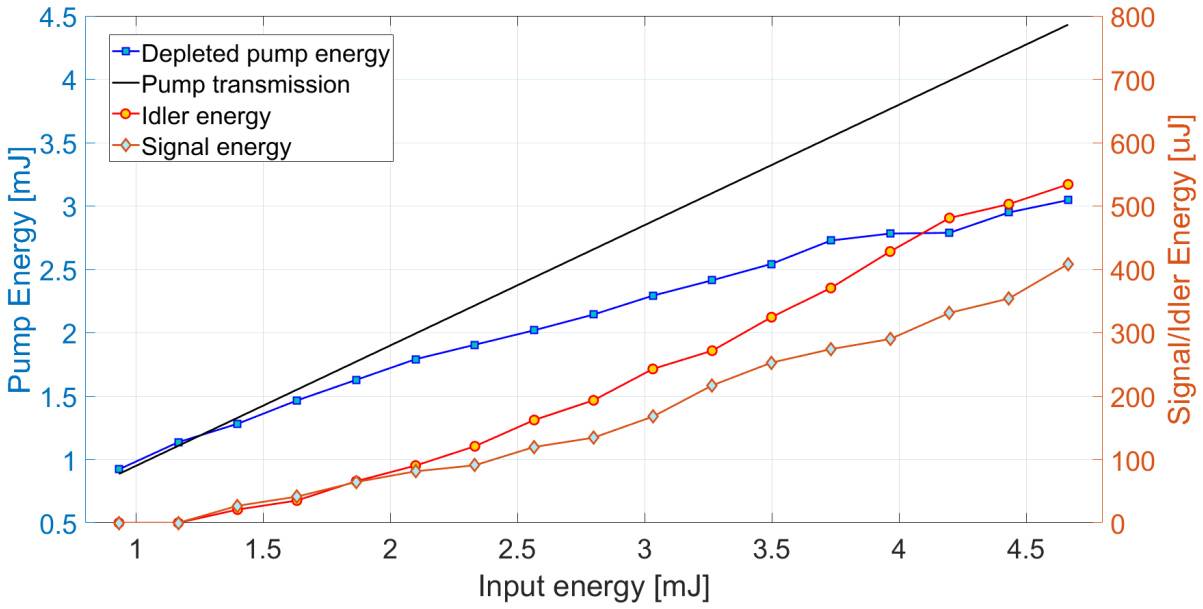

Figure 5.24: *BWOPO energy characterization.*

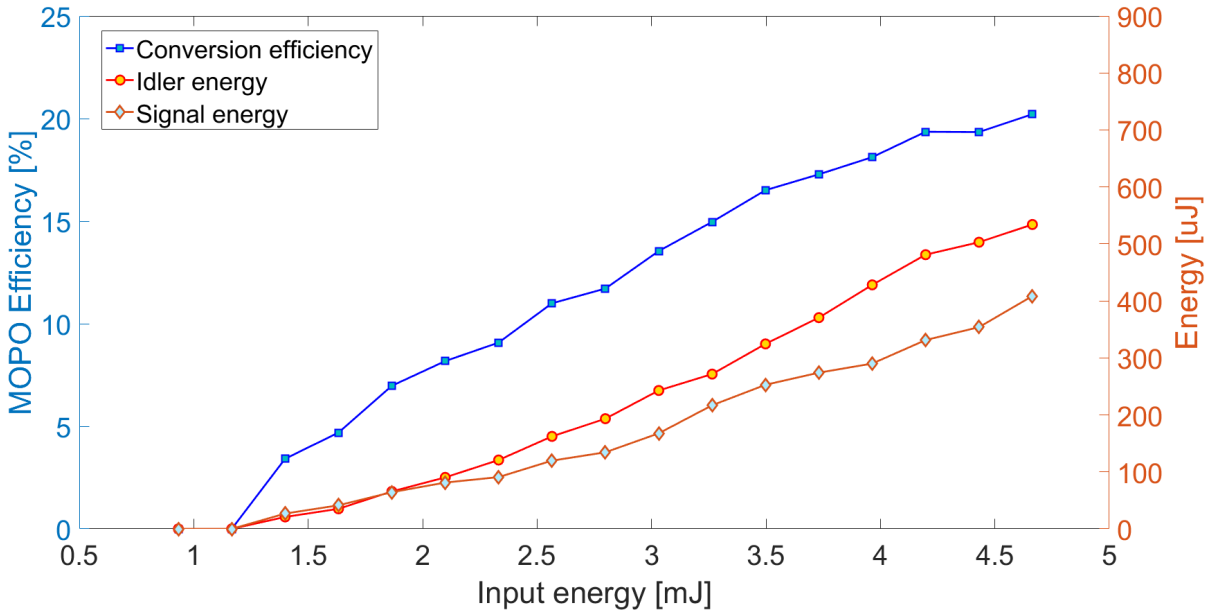

Figure 5.25: *BWOPO energy conversion efficiency.*

The system threshold is around 1.2 mJ of input energy. The nonlinear conversion efficiency reach 20% for maximum input energy, of 4.66 mJ. At maximum pump energy, it is possible to extract around 0.5 mJ of signal and idler radiations respectively. This is an extremely interesting result, considering the simplicity of the system, which requires only a correct

pump spatial and energy sizing. The possibility to grow bigger crystals and use pump beams with higher spatial quality could further enhance the conversion efficiency and interaction length.

The signal and idler wavelengths are respectively 1.855 μm and 2.494 μm (Fig. 5.25). The optical bandwidths are extremely narrow compared to the OPO output spectrum. Signal and idler display pulse durations of 3.3 and 2.6 ns, exhibiting spectra narrower than 0.2 nm respectively.

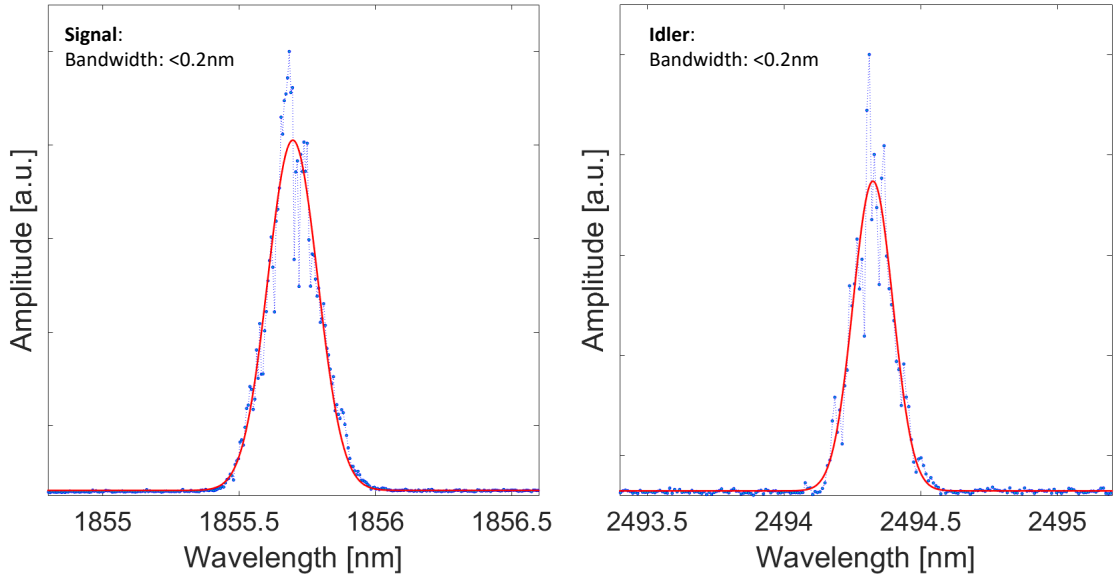

Figure 5.26: *BWOPO signal and idler spectra.*

The beam quality was investigated with a pyro camera. The signal beam is separated from 1 μm radiation by means of dichroic mirror. Then, after propagating through a low pass filter to suppress any green and residual pump radiation, the signal beam is focused with a spherical CaF lens with focal length of 350 mm.

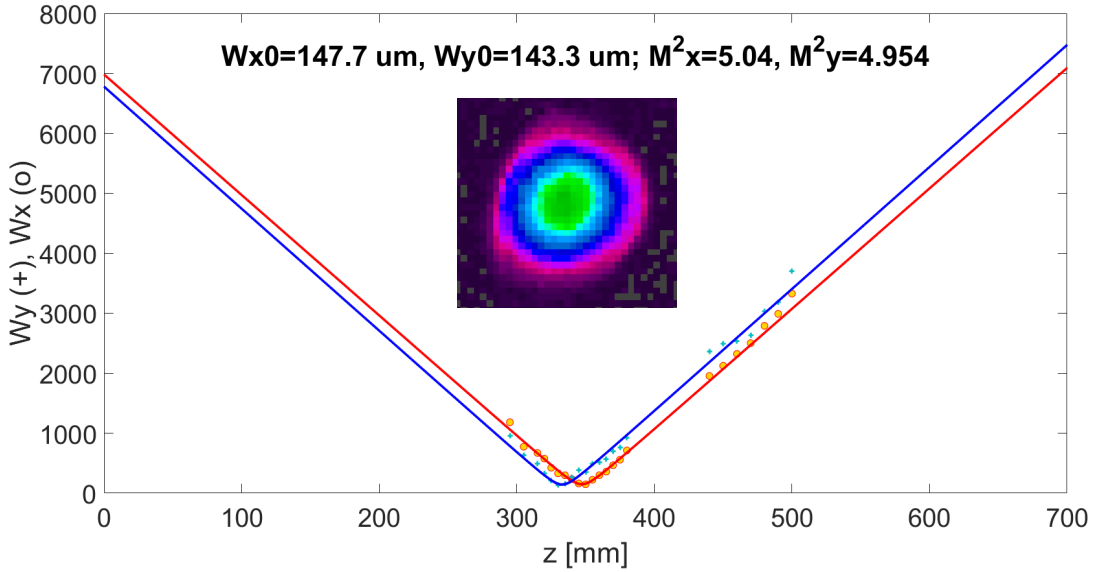

Figure 5.27: *BWOPO signal beam quality.*

The signal beam quality has a comparable M^2 (Fig. 5.26) to the pump radiation, which is an expected result considering the lack of optical cavity. Thus, to enhance the output beam quality of a BWOPO system, it is necessary to increase the pump beam quality. Recalling Fig. (5.22) the OPA stage is composed by several uncoated amplification KTP crystals. The crystal available were 6, which were tested in order to identify the quality of each crystal.

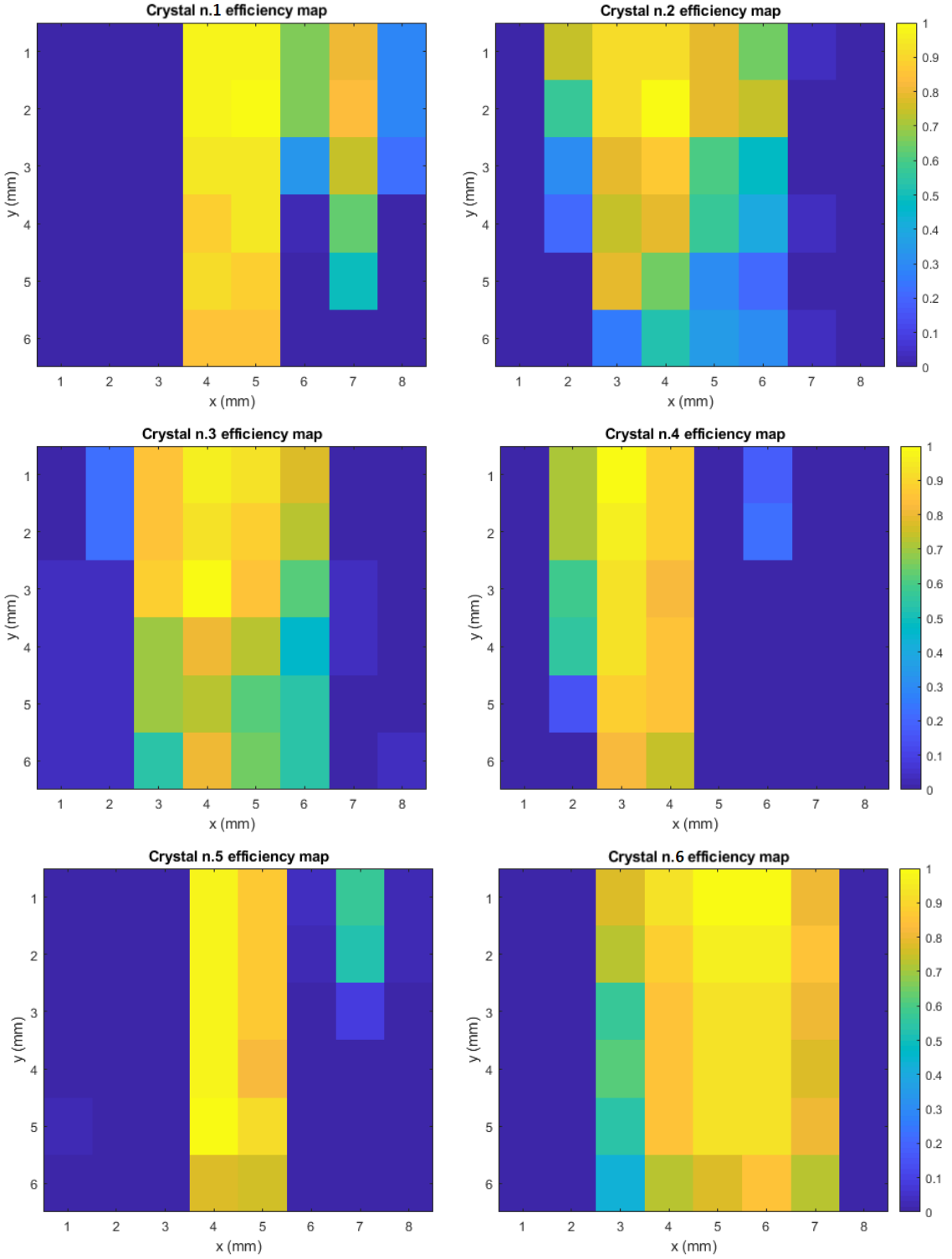

Figure 5.28: *KTP crystals efficiency maps for BWOPO amplification.*

Each crystal was individually investigated to derive the normalized conversion efficiency map. The method consisted in placing the KTP crystal inside the OPO cavity and observing the conversion efficiency change for different crystal positioning in the plane orthogonal the propagation axis. The resolution was given by the intracavity beam mode, which was calculated to be 0.4x0.4 mm^2 spot area by means of ABCD matrix analysis Fig. (5.7). This technique indicates the homogeneity of the crystal in terms of optical performance.
The efficiency map indicates the normalized crystal quality for the nonlinear coefficient. After it was recorded the maximum conversion efficiency, each subsequent inspection was related to the maximum. The dark blue pixel in Fig. (5.28) are the spatial region of the crystal which could not sustain oscillation.

Prior amplification, the signal and the pump beam were superimposed after the dichroic mirror in the BWOPO-OPA setup, (Fig. (5.22)) for optical parametric amplification. This approach allowed to optimize the two beam overlap for each amplification region, i.e., nonlinear crystal locations. The crystals used for amplification, manufactured ad hoc for the BWOPO amplification experiment at KTH, were uncoated KTP 8x8x15 mm^3 with 38.5 μm poling period. For amplification we used the crystal sequence 5-1-4-6 leading to an output pulse energy of 17 mJ with 200 μJ seeding signal energy and 150 mJ pump energy. If seeding was interrupted after the dichroic mirror, only 3 mJ of nonlinear radiation (OPG) were generated. Considering the transmission of the dichroic mirror at signal and idler wavelengths, their energies should be 12.5 mJ and 11.7 mJ for T_{signal}=69% and T_{idler}=73% respectively. It is worth reminding that this is a preliminary investigation for BWOPO amplification, because of the absence of AR coating, which in necessary to drastically enhance the amplification efficiency. The preliminary result gives an overall amplification efficiency of 8% for only signal radiation, realizing an optical gain G=50.

5.6 Comparison OPO vs BWOPO

The widespread OPO technology is a very convenient approach to efficiently convert a large amount of optical pump radiation. The cavity confinement enables to drastically enhance the non linear interaction and for a suitable pumping region the OPO is also able to generate a close to diffraction limited output. The spectral quality of OPO instead is a great disadvantage, because several modes are able to experience enough parametric gain. Thus OPO requires additional spectral sensitive optical elements or external seeding in order to generate narrow bandwidth laser pulses. Thus the overall complexity is quite significant for OPO with enhanced spectral quality. Comparing the OPO to the BWOPO, it can be noted the inferior energy extraction. Indeed, the signal radiation is not confined in a cavity, preventing an high conversion efficiency. However the system is able to generate pulses of hundreds of μJ, more than enough for efficient amplification. The BWOPO could theoretically scale enery extraction if bigger crystal could be grown. Currently, great efforts are made to further increase the BWOPO performance. The BWOPO, thanks to the counter propagating radiation, is able to self-seed itself. This is the cause for a narrow output spectrum, without any additional spectral sensitive element. The optical beam quality is comparable to the pump beam, pointing out the necessity of very high quality pump laser for nonlinear system based on BWOPO seeders, similar to OPG devices. BWOPO laser systems are very attractive, because they offer sufficient energy output level, comparable M^2 to the pump beam quality and

excellent spectral properties. In Tab. (5.2) it is summarized the two systems performance:

	OPO	**BWOPO**
Conversion efficiency	43%	20%
Maximum Output energy	1.5 mJ	400 μJ
Pulse duration	7 ns	3-4 ns
Beam quality: M^2	<5	<5
Spectral quality: Linewidth	73 nm	<0.2 nm
Wavelength	2100 nm	1855 nm
Complexity	High	Low
KTP dimension	5x7x12 mm^3	5x1x12 mm^3
Coating AR	yes	no
KTP poling period	38.86 μm	500 nm
Operative temperature	25-30 C°	25-30 C°

Table 5.2: *OPO and BWOPO results comparison*

The BWOPO technology represents an interesting alternative to the widespread OPO technology. The BWOPO would enable to generate narrow bandwidth laser radiation at specific wavelengths, determined by the pumping radiation and grating period. The complexity of the system is concentrated in the grow of BWOPO crystals of significant dimension. The absence of the cavity and the attractive property of the KTP crystal are key factor to realize simple and reliable optical converter for LIDAR systems. Furthermore OPA stages guarantee reliable energy scaling.

	OPO-OPA	**BWOPO-OPA**
Conversion efficiency	21%	8%
Gain	35	50
Maximum Output energy	28 mJ	12.5 mJ
Seeding energy	0.8 mJ	200 μJ
KTP dimension	5x7x12 mm^3	8x8x15 mm^3
Number of crystals employed	2	4
Effective length	12x2 mm	15x4 mm
Coating AR	yes	no
KTP poling period	38.86 μm	38.5 μm
Operative temperature	25-30 C°	25-30 C°

Table 5.3: *OPO-OPA and BWOPO-OPA results comparison*

The BWOPO signal radiation was successufully amplified, preserving the spectral properties. Currently further investigation on the BWOPO signal radiation amplification are undergoing in KTH.

Chapter 6

Conclusions

In this thesis, narrow bandwidth new DPSS laser architectures in the nanosecond regime, interesting for different applications, were developed and characterized. In all the projects I took part, the laser linewidth was a primary parameter, which is fundamental for several applications such as Doppler LIDAR and HSRL systems. The spectral management, i.e., bandwidth tailoring, is a critical aspect for laser engineering. Typically laser sources require complex optical solution to control the output spectrum. The self seeding technique is proposed as a practical and successful approach for bandwidth tailoring for both conventional laser sources and nonlinear devices.

In the first part of this work Single Longitudinal Mode (SLM) operation theory is described within the possible techniques which can be adopted to enforce this specific regime, necessary for transform limited pulse generation. Then it is also proposed a model for laser operation in Passive Q-Switching regime which takes into account excited states absorption in the saturable absrober, i.e., Cr:YAG^{4+}. This model is of immediate use in the understanding the critical parameters and theirs selection during laser design.

The SISRO (Self Injection Seeded Ring Oscillator) architecture is the technology developed to implement self seeding. The SISRO enables to efficiently suppress spatial hole burning and to seed the laser with an optical radiation, which is already frequency matched and locked to the cavity. The architecture comprehends a ring laser cavity and an external feedback mirror. The feedback mirror is used to redirect back inside the cavity one of the two spatially separated laser output. This action unbalance the laser cavity and help switching from standing wave regime to travelling wave regime. At the same time, the dominant laser longitudinal mode seeds the oscillator, thus amplifying the strongest oscillation. Laser oscillators based on Nd:YVO_4 and Nd:YAG were observed to emit close to transform limited laser pulses with laser linewidths ranging from few units of MHz to few tens of MHz. The output pulse energies stood between few tens of μJ to few hundreds of μJ.

The technique was refined to the point not to require any intracavity filtering element in order to emit close to transform limited pulses of tens of nanosecond. The SISRO architecture is extremely simple, not requiring any expensive filter or additional optical sources compared to conventional approaches. Nd:YVO_4 and Nd:YAG have been proven both reliable active materials for narrow linewidth pulse emission, in the 1 μm region. These materials are very common in laser industrial engineering, enhancing the attractiveness of the SISRO technology as a viable solution for narrow bandwidth laser emission. Pulsed operation is achieved by means of Passive Q-Switching technique, which traduces in the use of a Cr^{4+}:YAG saturable absorber inside the laser cavity. Then, the system has the attractive additional property to be

an all passive, modular and reliable device. With the aid of a rate-equation based model of pulse-to-pulse timing jitter in PQS lasers, we were able to significantly reduce this unwanted effect. The pulse-to-pulse time jitter, which is a common critical issue for PQS oscillators has been drastically mitigated by the implementation of a pulsed optical pump diode, achieving a pulse-to-pulse jitter standard deviation comparable to the pulse duration. Thus, the SISRO architecture represents a suitable candidate for doppler LIDAR sources and a attractive seeder for Master Oscillator Power Amplifier design for high energy class sources, which can be employed by the HSRL.

In addition opitcal parametric oscillators has been investigated for wavelength extension. Accessing exotic wavelength is difficult by means of conventional lasers. Nonlinear techniques represent an elastic approach to generate wavelengths which can not be realized efficiently and/or economically with current state of the art crystals. Optical Parametric Oscillators (OPO) and Distributed Feedback Optical Parametric Oscillators (BWOPO), the latter indicated also as Mirrorless Optical Parametric Oscillators (MOPO), have been designed and tested for wavelengths extension of Nd:YAG source emitting at 1064 nm to the 2 μm region. Nonlinear optical amplifiers were also realized to boost the oscillator energies exploiting the same pump radiation. For both oscillators, spectral analysis was conducted with output energy, pulse duration and beam quality. The nonlinear optical material chosen was the Rubidium Doped KTP. This material is favorable for nonlinear applications due to the high nonlinear coefficient and high damage threshold.

The self seeding operation realized in the BWOPO (or MOPO), enabled by the extremely small poling period of few hundreds of nm, has proven successful to preserve the pulse spectral quality, i.e. the laser linewidth. Pulse spectra of both signal and idler radiations respectively at 1855 and 2494 nm were narrower than 0.2 nm FWHM. This is in contrast to OPO technology, which does not permit to access comparable spectral performance without a significant higher complexity because of the need for frequency selective elements or external seeding. BWOPO displays a series of attractive features which can push forward the technology and potentially supplant OPO in certain fields, such as for remote sensing applications. The very low complexity, the ability to preserve the spectral and the spatial quality of the pump radiation along with a reasonable energy efficiency places this technology as an appealing component for LIDAR systems sources.

Appendix A

CAD drawings for SISRO

This appendix displays the technical drawing used to realize the mechanical parts for the square SISRO. The material used in most of the objects is aluminium 6082, typically used for space frame. Some of the most important properties of aluminium 6082 are:

- Aluminium 6082 Density: 2.70 g/cm³
- Aluminium 6082 Thermal Expansion: 24 x10^{-6} /K
- Aluminium 6082 Modulus of Elasticity: 70 GPa
- Aluminium 6082 Thermal Conductivity: 180 W/m.K
- Aluminium 6082 Electrical Resistivity: 0.038 x10^{-6} Ωm

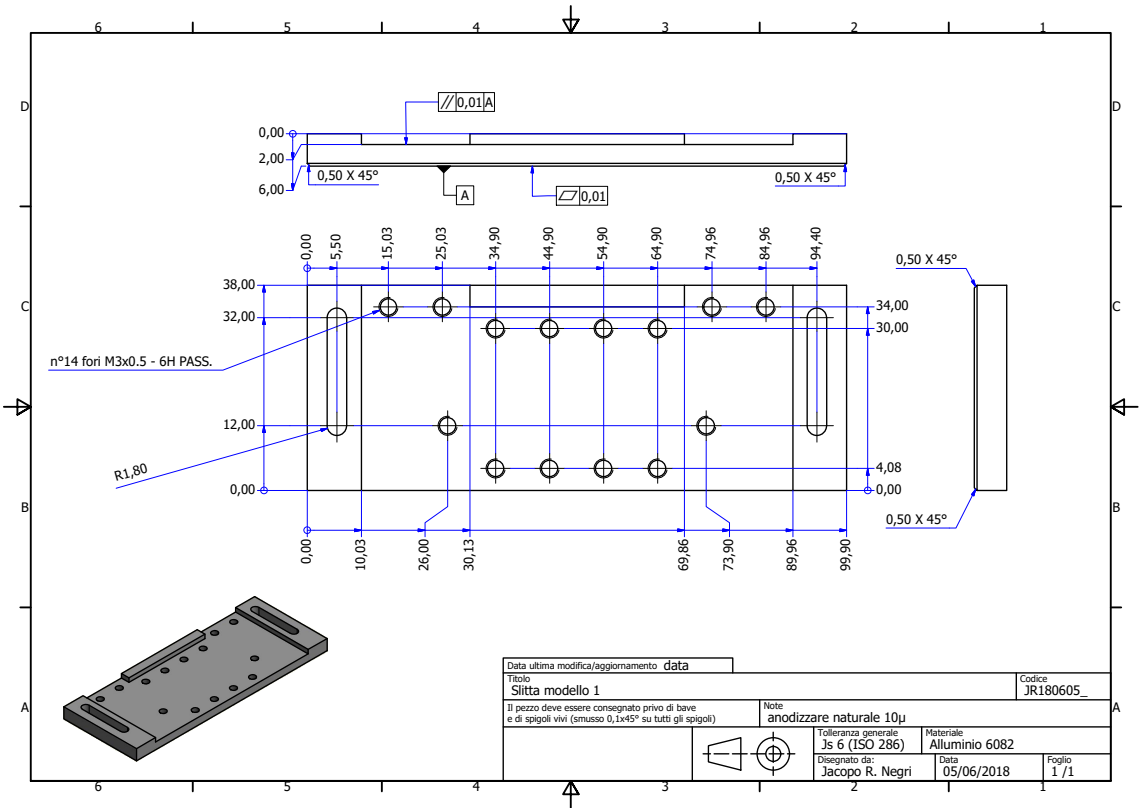

Figure A.1: *Aluminium slit for optical holders and crystal holder*

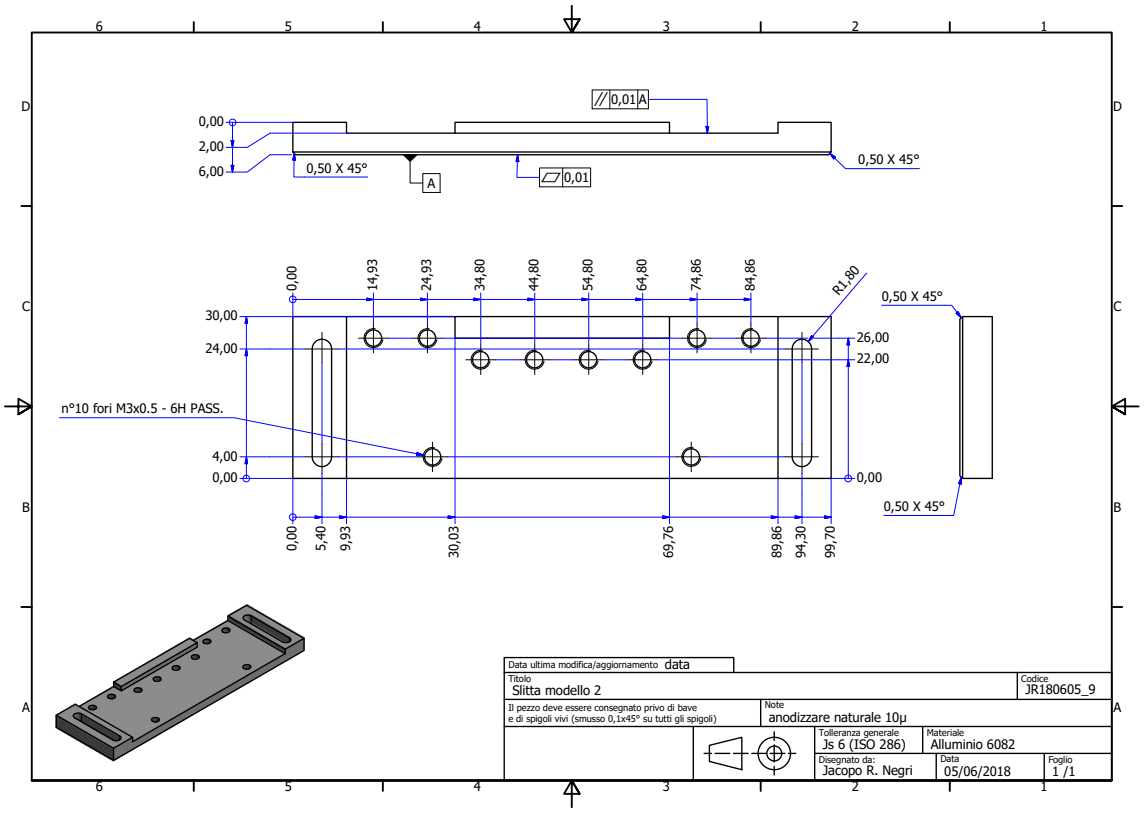

Figure A.2: *Aluminium slit for optical holders*

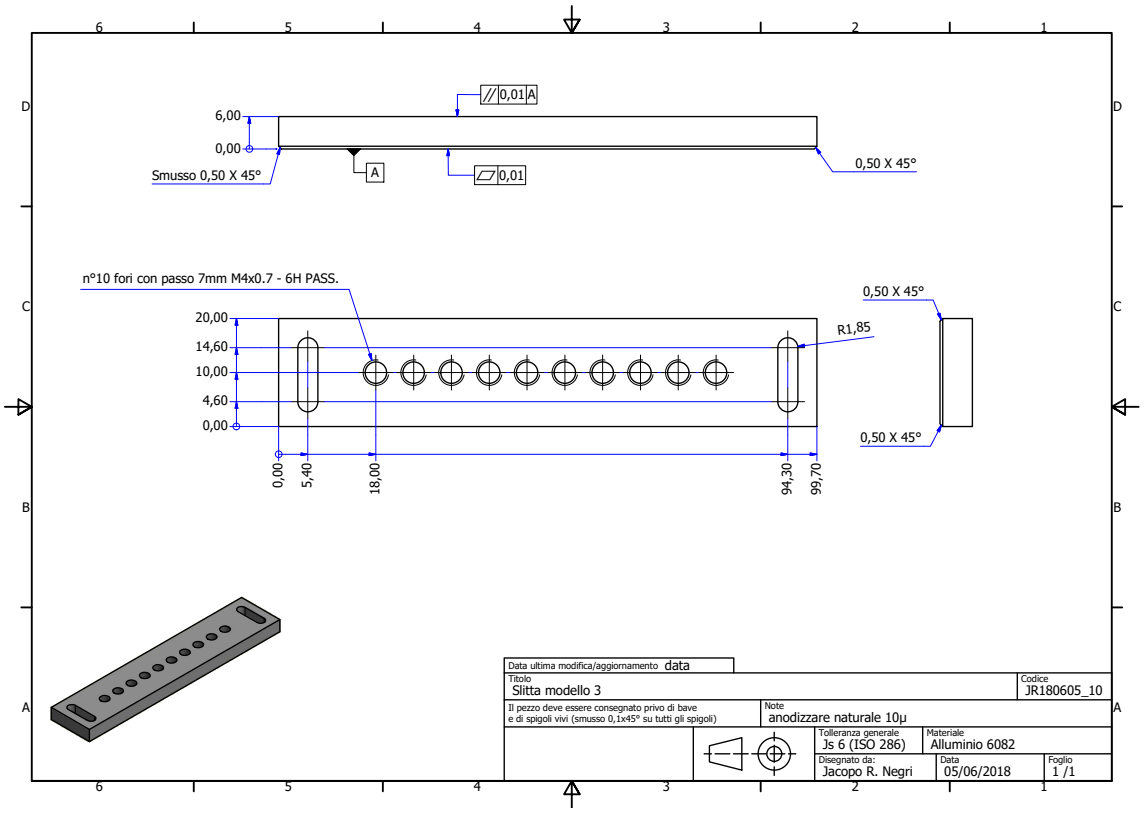

Figure A.3: *Aluminium slit for etalon holder*

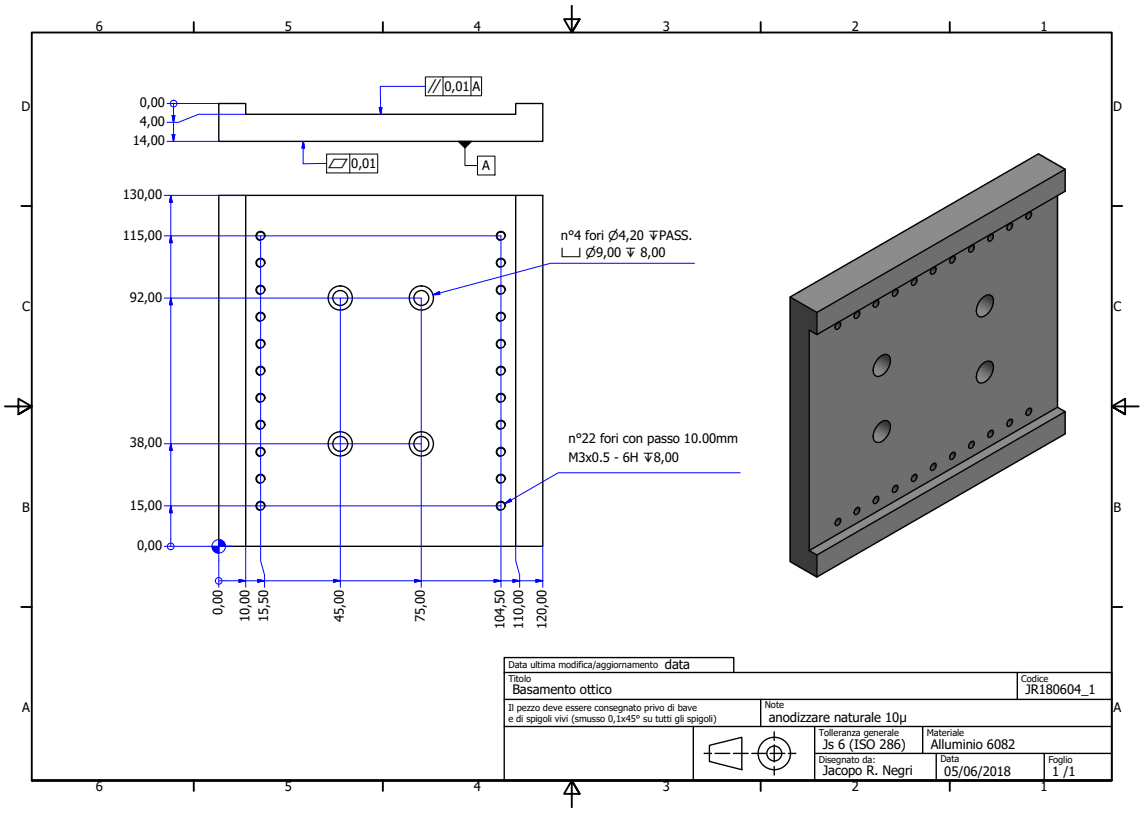

Figure A.4: *Aluminium basament for slits*

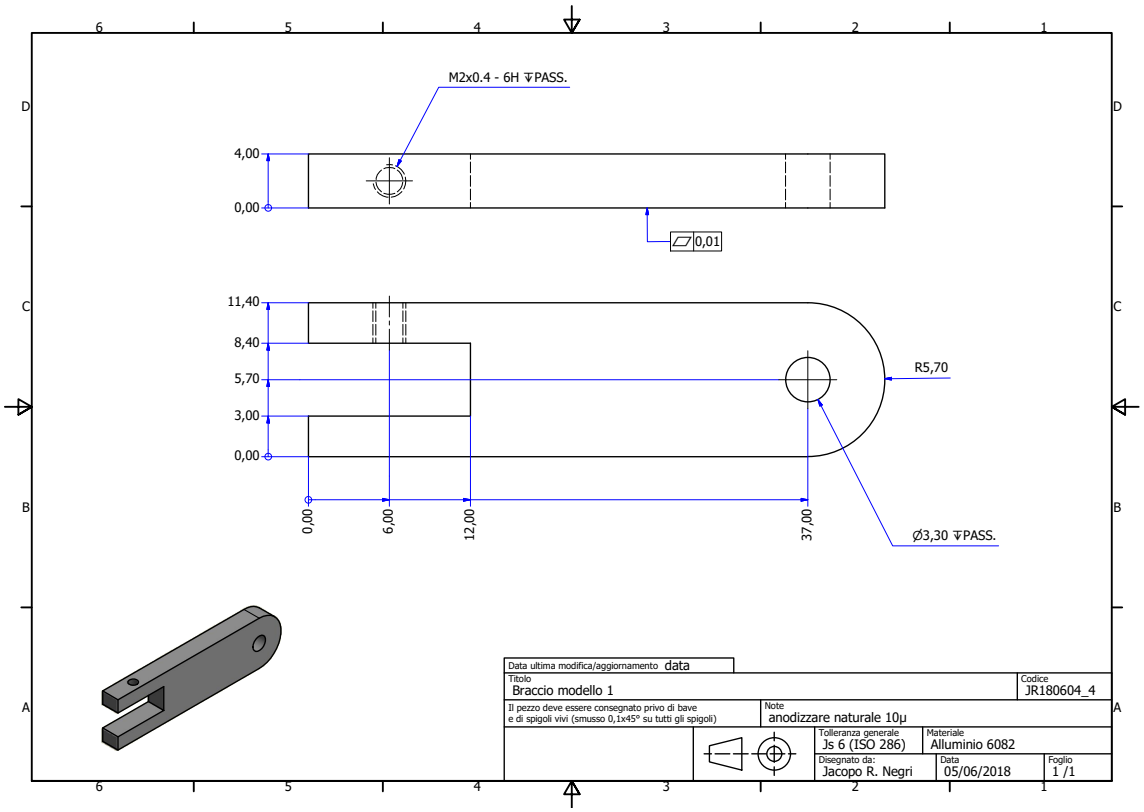

Figure A.5: *Aluminium etalon holder*

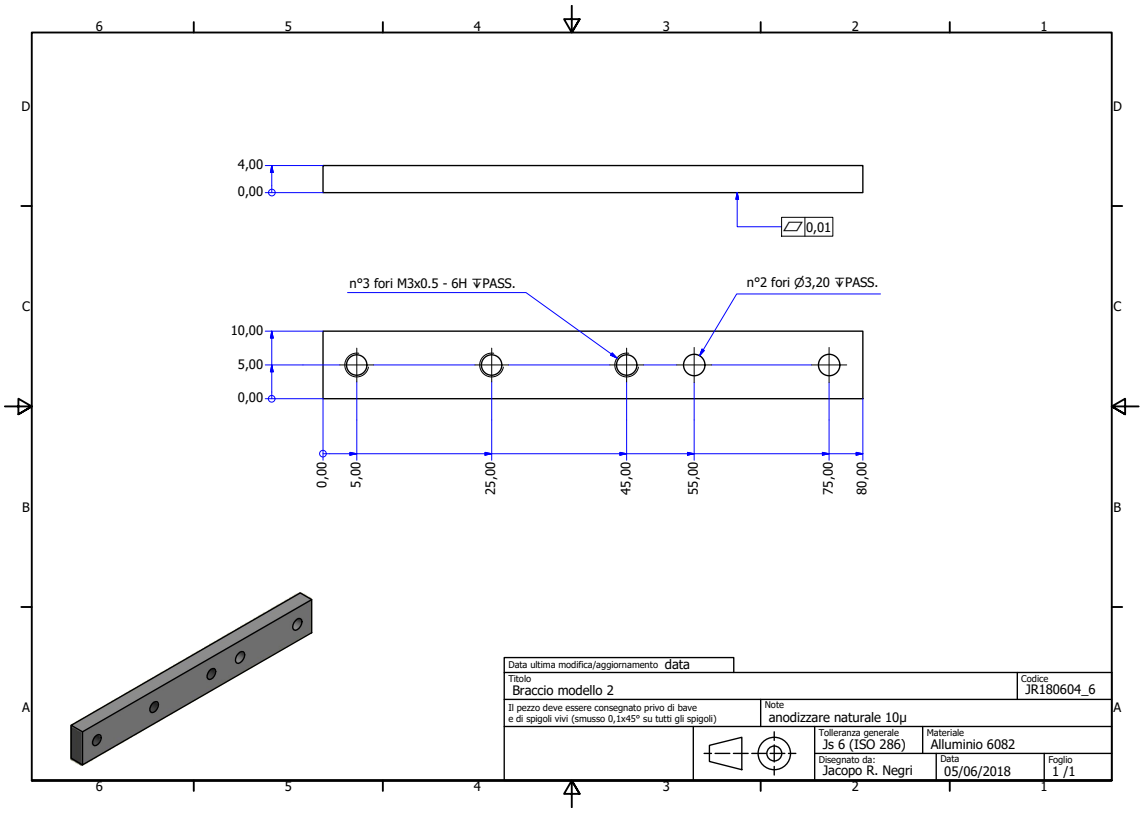

Figure A.6: *Aluminium alignment support arm*

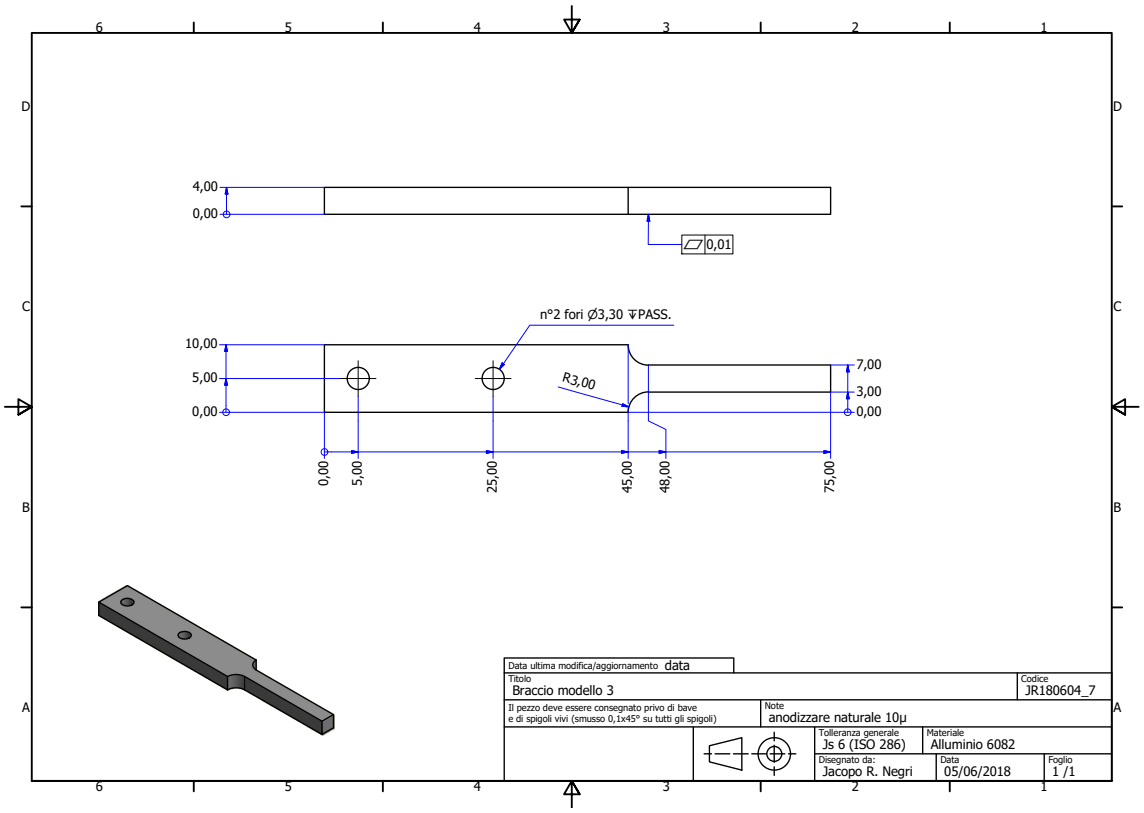

Figure A.7: *Aluminium alignment arm*

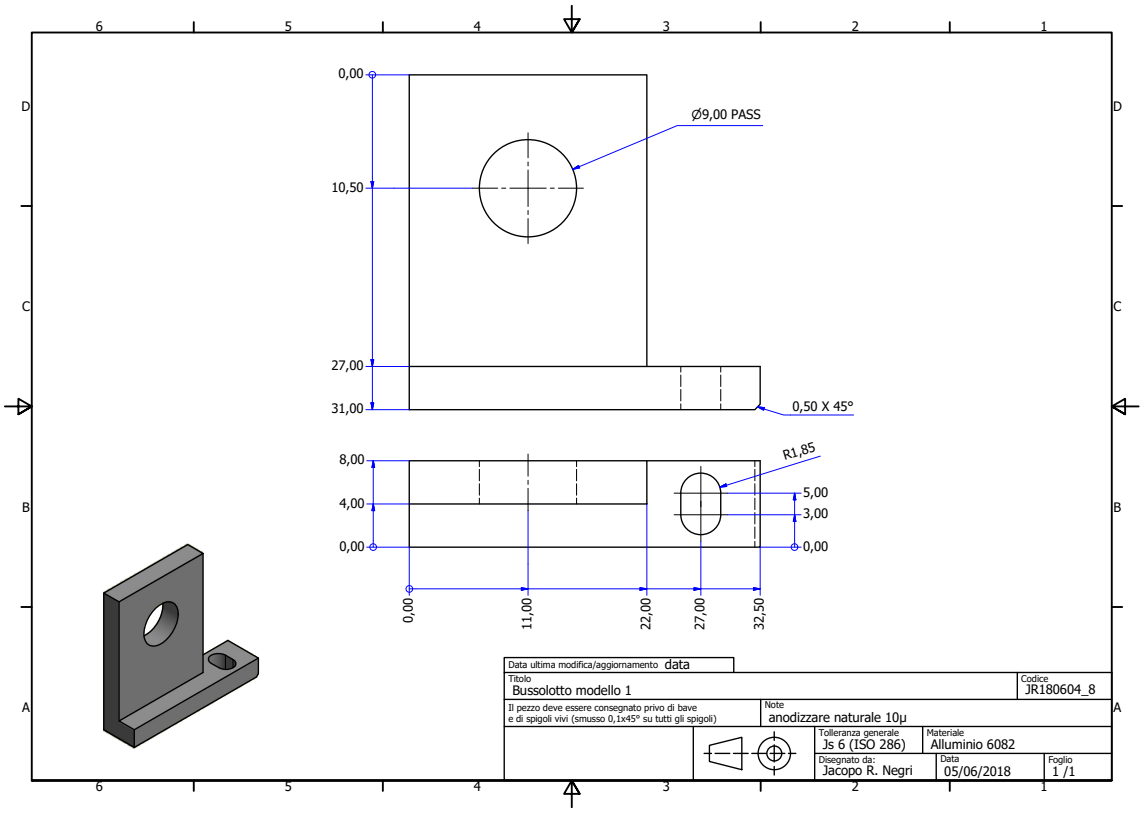

Figure A.8: *Aluminium generic optical element holder*

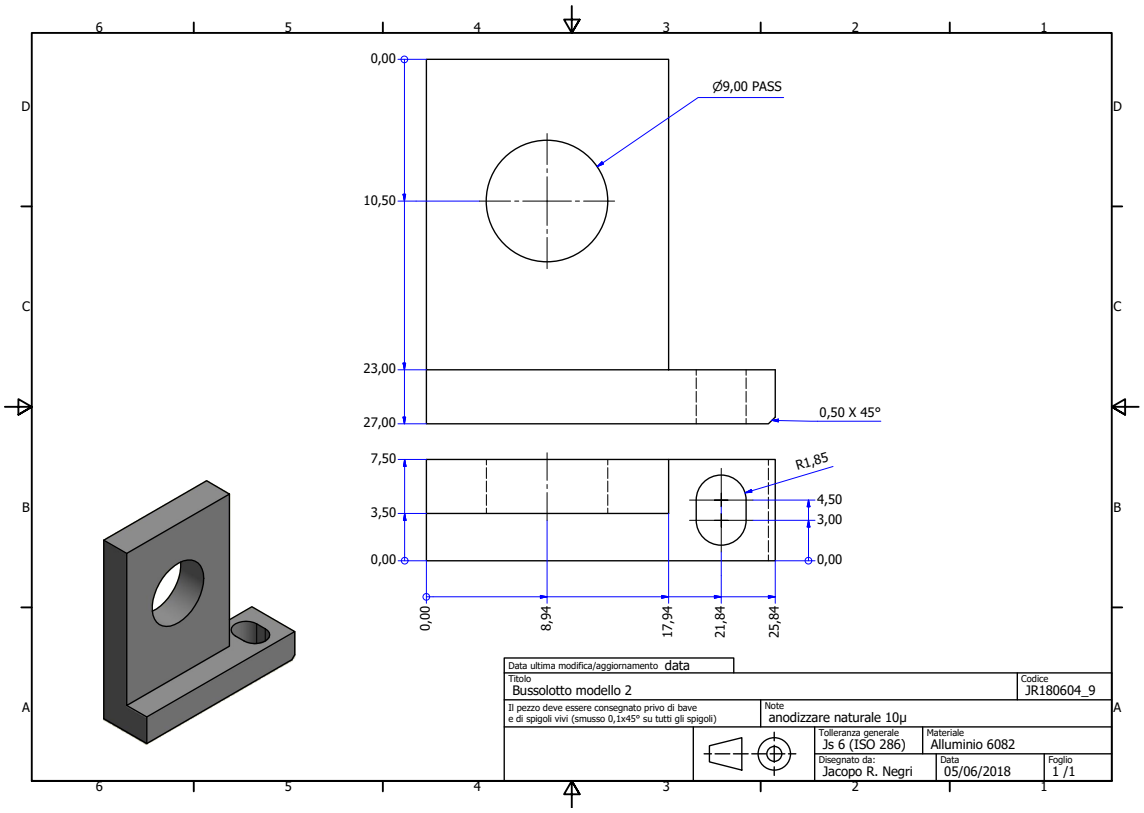

Figure A.9: *Aluminium generic optical element holder*

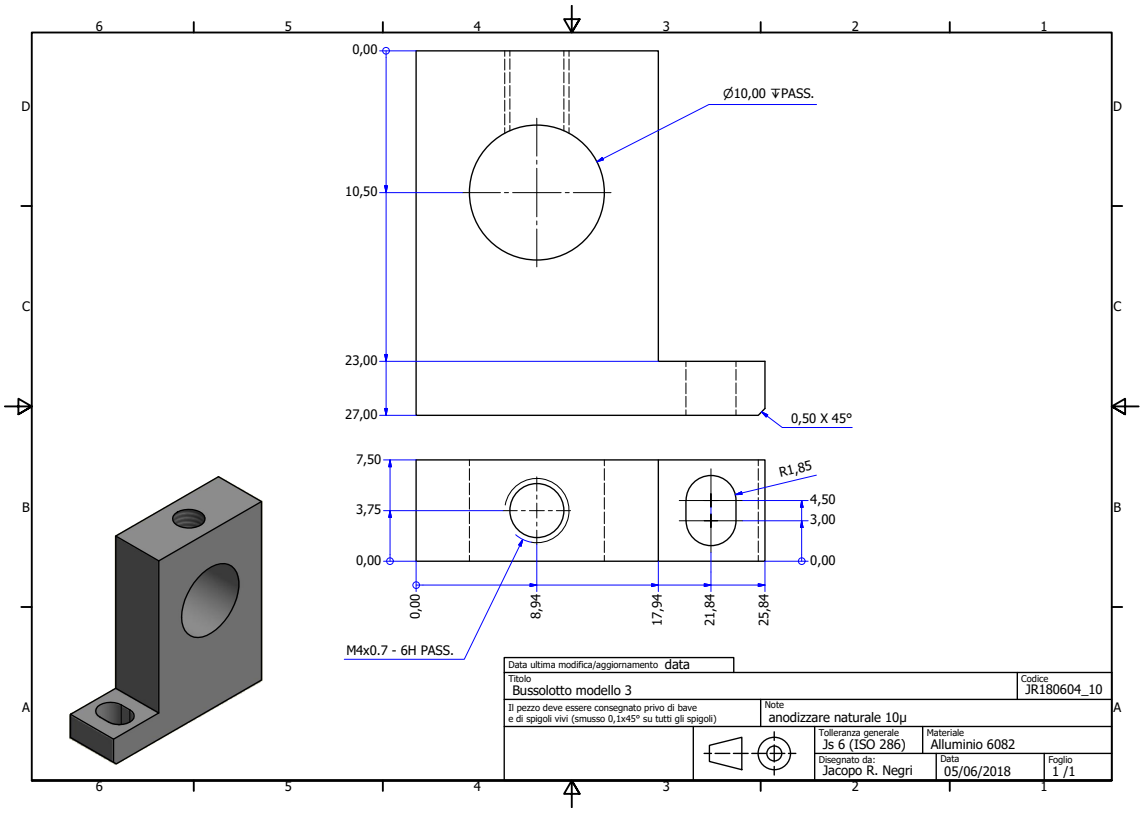

Figure A.10: *Aluminium HWP holder*

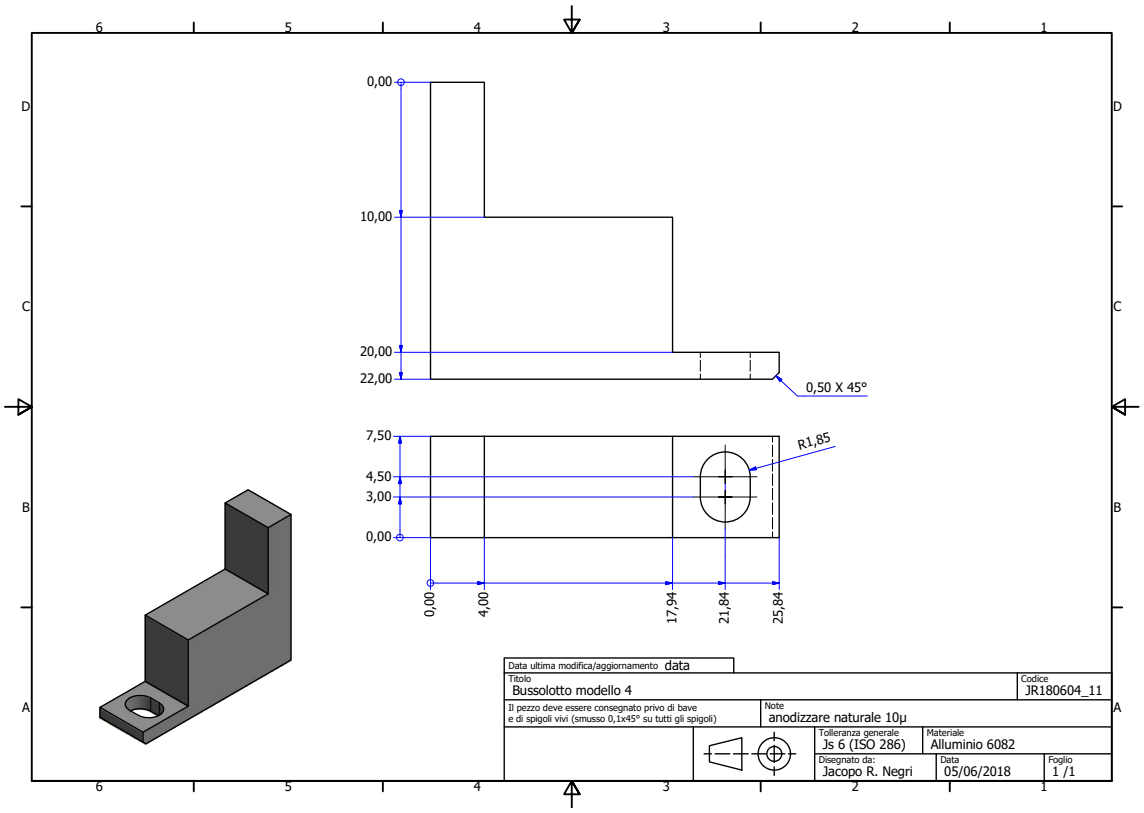

Figure A.11: *Aluminium generic optical element holder*

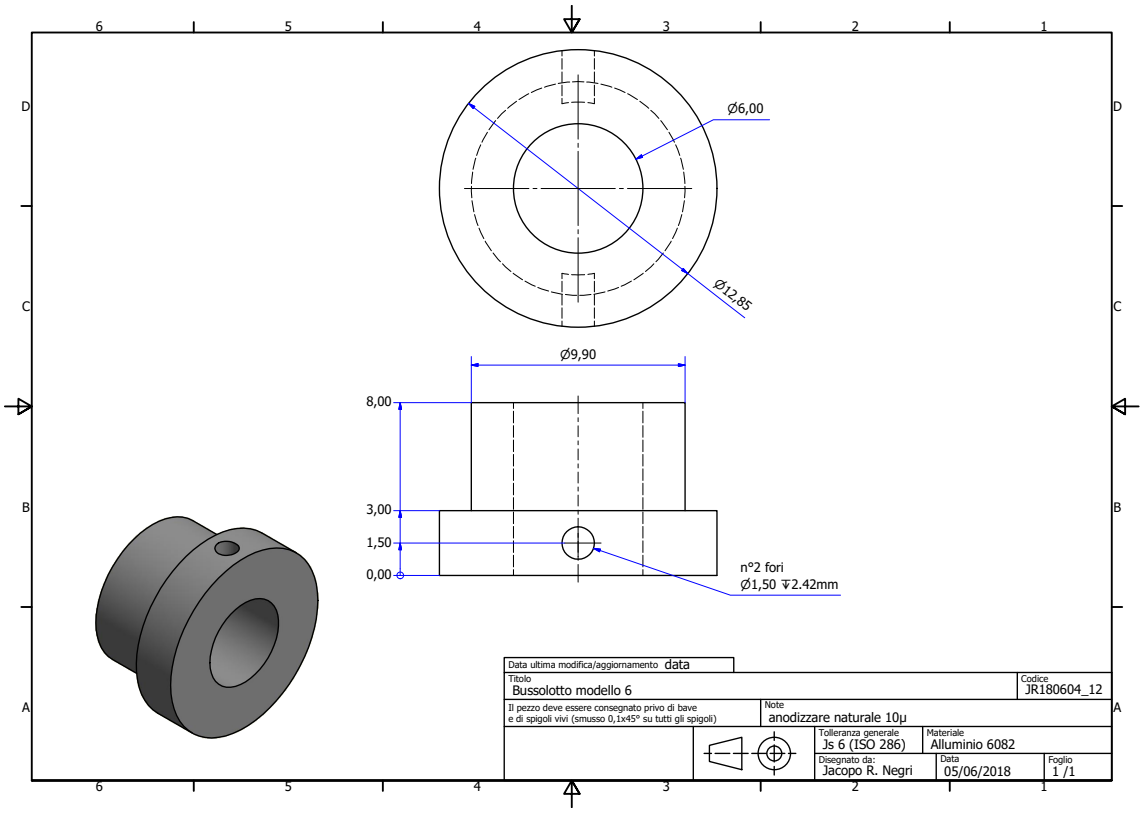

Figure A.12: *Aluminium HWP compass*

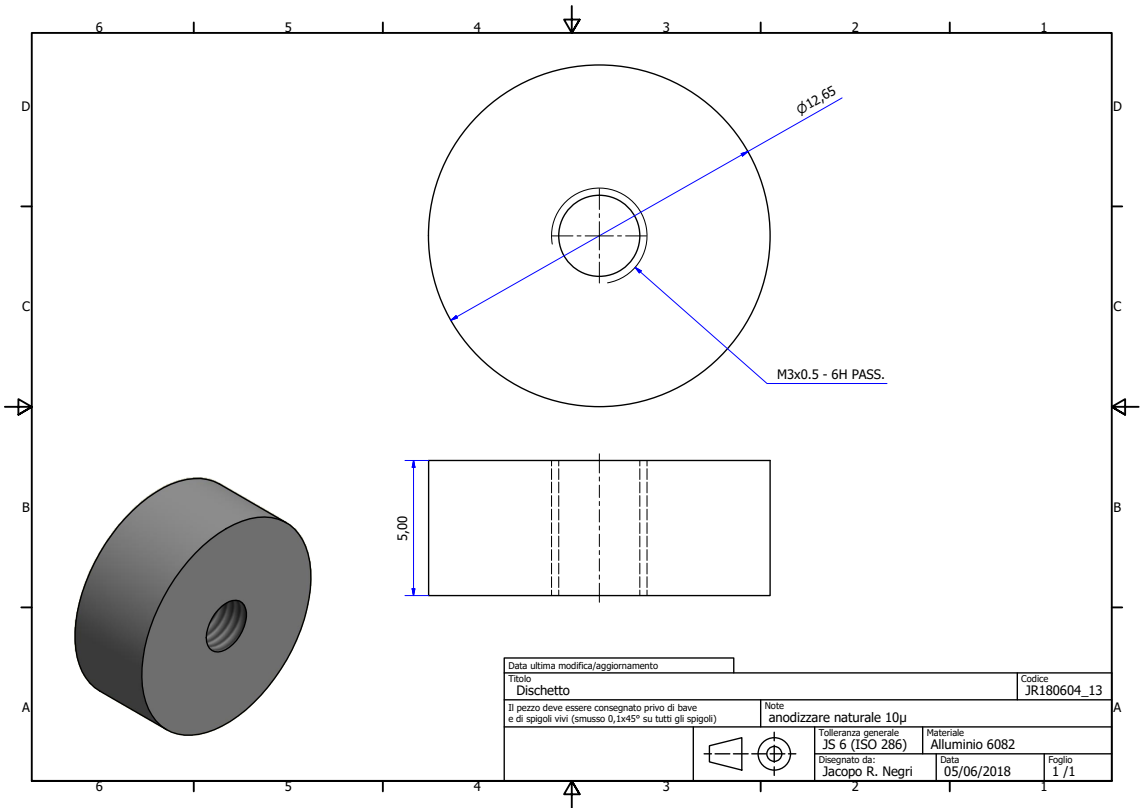

Figure A.13: *Aluminium etalon hoder support*

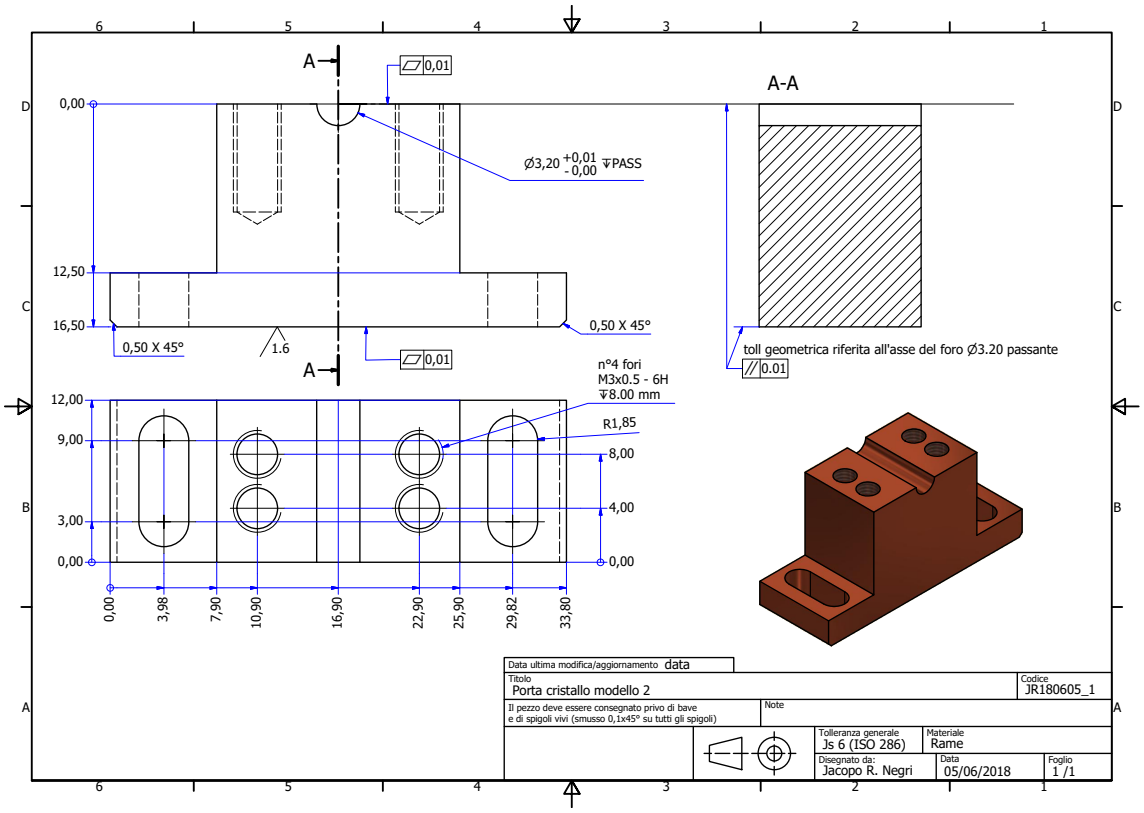

Figure A.14: *Copper crystal holder basis*

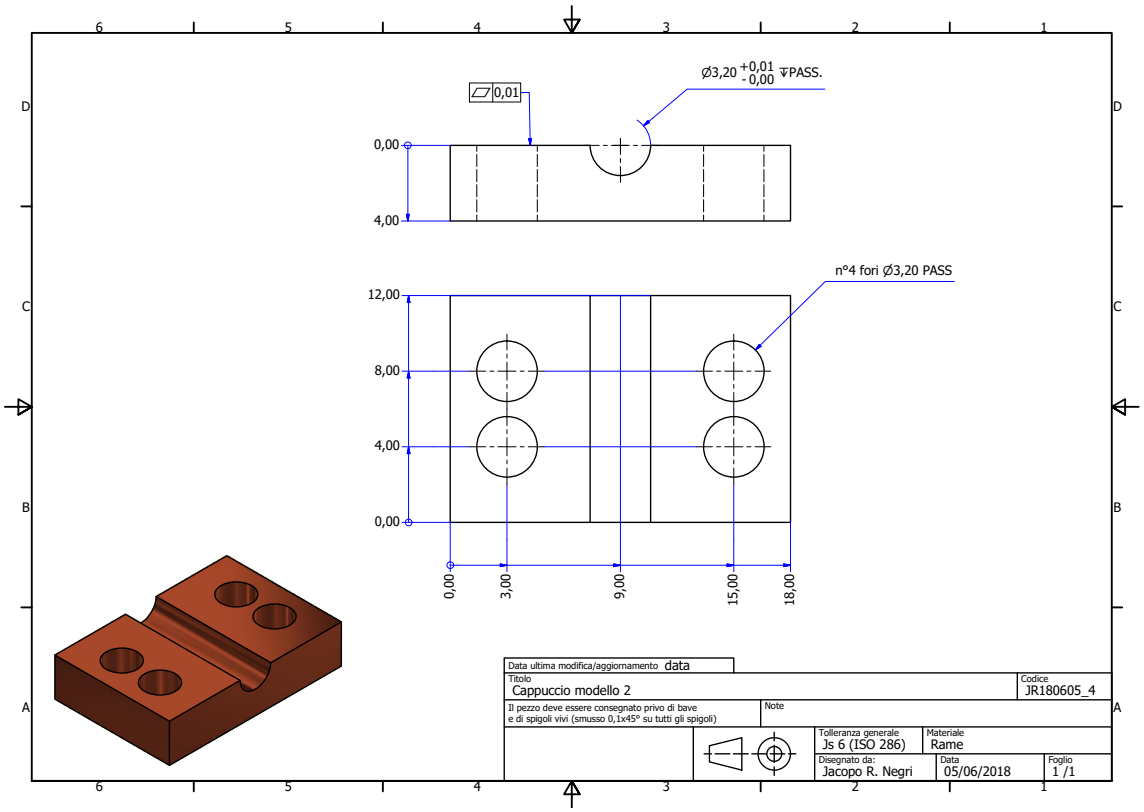

Figure A.15: *Copper crystal holder top*

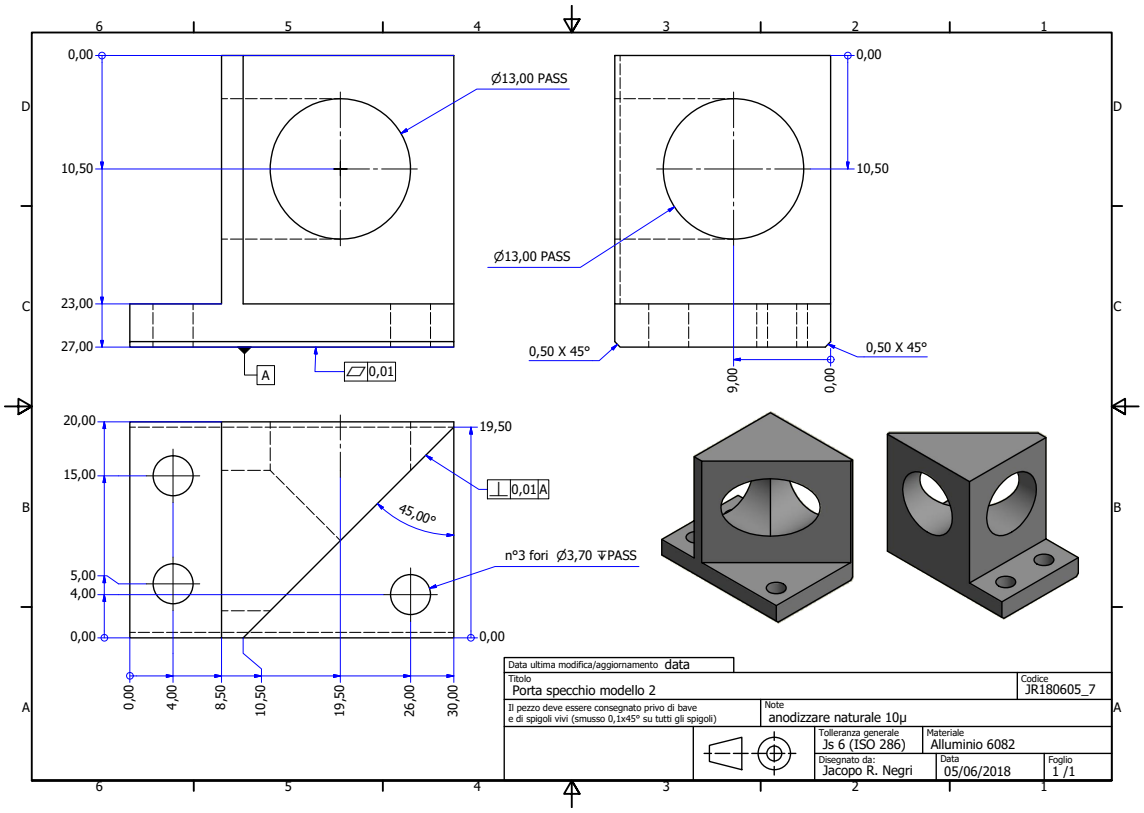

Figure A.16: *Aluminium mirror holder*

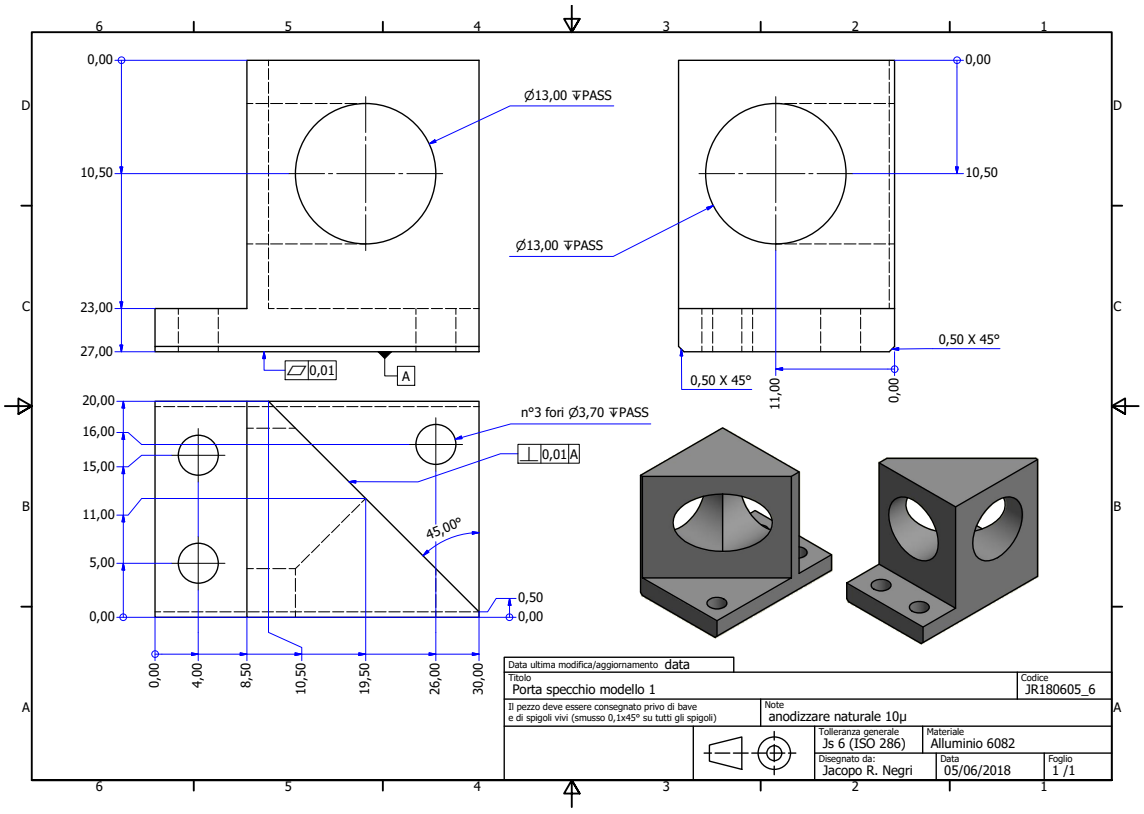

Figure A.17: *Aluminium mirror holder*

Bibliography

[1] Joshi, Deepti, Kumar, Deepak, Maini, Anil K., Sharma, and Ramesh C. Detection of biological warfare agents using ultra violet-laser induced fluorescence lidar. *Spectrochimica Acta Part A: Molecular and Biomolecular Spectroscopy*, 2013. 1

[2] Kechagias-Stamatis, Odysseas, Aouf, Nabil, Richardson, and Mark A. 3d automatic target recognition for future lidar missiles. *IEEE Transactions on Aerospace and Electronic Systems*, 2016. 1

[3] Kechagias-Stamatis, Odysseas, Aouf, and Nabil. Evaluating 3d local descriptors for future lidar missiles with automatic target recognition capabilities. *The Imaging Science Journal*, 2017. 1

[4] Li, Min-le, Hu, Yi-hua, Zhao, Nan-xiang, Qian, and Qi-shu. Modeling and analyzing point cloud generation in missile-borne lidar. *Defence Technology*, 2019. 1

[5] Bufton and Jack L. Lidar and camera fusion approach for object distance estimation in self driving vehicles. *Simmetry*, 2020. 1

[6] European Commision. Annual accident report. 2018. 1

[7] Lee, Hyunsung, Kim, Seonwook, Park, Sungyoul, Jeong, Yonghwan, Lee, Hojoon, Yi, and Kyongsu. Avm / lidar sensor based lane marking detection method for automated driving on complex urban roads. *Simmetry*, 2017. 1

[8] Hälker, Jens, Barth, and Harald. Lidar as a key technology for automated and autonomous driving. *ATZ worldwide*, 2018. 1

[9] G Ajay Kumar, Jin Hee Lee, Jongrak Hwang, Jaehyeong Park, Sung Hoon Youn, and Soon Kwon. Airborne lidar for profiling of surface topography. *Optical Engineering*, 1991. 1

[10] Feng Zhao, Xiaoyuan Yang, Mitchell A. Schull, Miguel O. Román-Colón, Tian Yao, Zhuosen Wang, Qingling Zhang, David L.B. Jupp, Jenny L. Lovell, Darius S. Culvenor, Glenn J. Newnham, and Andrew D. Richardso. Measuring effective leaf area index, foliage profile, and stand height in new england forest stands using a full-waveform ground-based lidar. *Remote sensing of environment*, 2011. 1

[11] Resop, Jonathan P., Lehmann, Laura, Hession, and W. Cully. Drone laser scanning for modeling riverscape topography and vegetation: Comparison with traditional aerial lidar. *Drones*, 2019. 1

[12] Bufton and Jack L. Airborne lidar for profiling of surface topography. *Optical Engineering*, 1991. 1

[13] Ulrich Weiss and Peter Biber. Plant detection and mapping for agricultural robots using a 3d lidar sensor. *Robotics and Autonomous Systems*, 2011. 1

[14] L. Mei, Z. G. Guan, H. J. Zhou, Z. R. Zhu J. Lv, J. A. Cheng, F. J. Chen, C. Löfstedt, S. Svanberg, and G. Somesfalean. Agricultural pest monitoring using fluorescence lidar techniques. *Applied Physics B: Lasers and Optics*, 2012. 1

[15] Schulze-Brüninghoff, Damian, Hensgen, Frank, Wachendorf, Michael v Astor, and Thomas. Methods for lidar-based estimation of extensive grassland biomass. *Computers and Electronics in Agriculture*, 2019. 1

[16] Malavazi, Flavio B.P., Guyonneau, Remy, Fasquel, Jean-Baptiste, Lagrange, Sebastien, Mercier, and Franck. Lidar-only based navigation algorithm for an autonomous agricultural robot. *Computers and Electronics in Agriculture*, 2018. 1

[17] Linda J. Mullen, Vincent M. Contarino, and Peter R. Herczfeld. Patent no. 7,010,339 b2. *United States Patent*, 2006. 1

[18] Murphy, Richard J., Taylor, Zachary, Schneider, Sven, Nieto, and Juan. Mapping clay minerals in an open-pit mine using hyperspectral and lidar data. *European Journal of Remote Sensing*, 2015. 2

[19] Matt Lato, Mark S. Diederichs, D. Jean Hutchinson, and Rob Harrap. Optimization of lidar scanning and processing for automated structural evaluation of discontinuities in rockmasses. *International journal of rock mechanics and Mining sciences*, 2009. 2

[20] Giovanni Gigli and Nicola Casagli. Semi-automatic extraction of rock mass structural data from high resolution lidar point clouds. *International Journal of Rock Mechanics and Mining Sciences*, 2011. 2

[21] J. Kar, M.A. Vaughan, Omar Liu, Z., Trepte A.H., C.R., Tackett, J., Fairlie, T.D., Kowch, and R. Detection of pollution outflow from mexico city using calipso lidar measurements. *Remote Sensing of Environment*, 2015. 2

[22] S.R. Ahmad and E.M. Billiet. Implications of atmospheric attenuation in raman lidar detection of pollutants. *Optics Laser Technology*, 1991. 2

[23] S.R. Ahmad and E.M. Billiet. Performance evaluation of a laboratory-based raman lidar in atmospheric pollution measurement. *Optics Laser Technology*, 1994. 2

[24] H. Edner and S. Svanberg. Lidar measurements of atmospheric mercury. *Water, Air Soil Pollution*, 1991. 2

[25] R.R. Agishev, A. Comeron, B. Gross, F. Moshary, S. Ahmed, A. Gilerson, and V.A. Vlasov. Application of the method of decomposition of lidar signal-to-noise ratio to the assessment of laser instruments for gaseous pollution detection. *Applied Physics B: Lasers and Optics*, 2004. 2

[26] J. Keder, M. Střižík, P. Berger, A. Černý, P. Engst, and I. Němcová. Remote sensing detection of atmospheric pollutants by differential absorption lidar 510m/sodar pa2 mobile system. *Meteorology and Atmospheric Physics*, 2004. 2

[27] Fredriksson K., Galle B., Nyström K., and Svanberg S. Lidar system applied in atmospheric pollution monitoring. *Applied Optics*, 1979. 2

[28] Bossanyi, Kumar E A, A, Hugues-Salas, and O. Wind turbine control applications of turbine-mounted lidar. *Journal of Physics Conference Series*, 2014. 2

[29] Gao, Xiaoxia, Wang, Tengyuan, Li, Bingbing, Sun, Haiying, Yang, Hongxing, Han, Zhonghe, Wang, Yu, Zhao, and Fei. Investigation of wind turbine performance coupling wake and topography effects based on lidar measurements and scada data. *Applied Energy*, 2019. 2

[30] David Schlipf, Dominik Johannes Schlipf, and Martin Kühn. Nonlinear model predictive control of wind turbines using lidar. *Wind Energy*, 2012. 2

[31] Gao, Xiaoxia, Wang, Tengyuan, Li, Bingbing, Sun, Haiying, Yang, Hongxing, Han, Zhonghe, Wang, Yu, Zhao, and Fei. Investigation of wind turbine performance coupling wake and topography effects based on lidar measurements and scada data. *Applied Energy*, 2019. 2

[32] Gao, Xiaoxia, Wang, Tengyuan, Li, Bingbing, Sun, Haiying, Yang, Hongxing, Han, Zhonghe, Wang, Yu, Zhao, and Fei. Wind turbine wake visualization and characteristics analysis by doppler lidar. *Optics Express*, 2016. 2

[33] Aitken, Matthew L., Rhodes, Michael E., Lundquist, and Julie K. Performance of a wind-profiling lidar in the region of wind turbine rotor disks. *Journal of Atmospheric and Oceanic Technology*, 2012. 2

[34] Smalikho, I. N., Pitchugina, Y. L., Banakh, V. A., and W. A. Brewer. Measurements of the wind turbine wake parameters with a pulsed coherent lidar under various atmospheric conditions. *Russian Physics Journal*, 2013. 2

[35] Newsom, Rob K., Berg, Larry K., Shaw, William J., Fischer, and Marc L. Turbine-scale wind field measurements using dual-doppler lidar. *Wind Energy*, 2015. 2

[36] Raghavendra Krishnamurthy, Ronald Calhoun, Brian Billings, and James Doyle. Wind turbulence estimates in a valley by coherent doppler lidar. *Meteorological Applications*, 2011. 2

[37] Graeme J. Nott and Thomas J. Duck. Lidar studies of the polar troposphere. *Meteorological Applications*, 2011. 2

[38] J. C. Davis, C. G. Collier, F. Davies, and K. E. Bozier. Spatial variations of sensible heat flux over an urban area measured using doppler lidar. *Meteorological Applications*, 2008. 2

[39] Pierre H. Flamant. Atmospheric and meteorological lidar: from pioneers to space applications. *Comptes Rendus Physique*, 2005. 2

[40] M. Lilley, S. Lovejoy, K. B. Strawbridge, D. Schertzer, and A. Radkevich. Scaling turbulent atmospheric stratification. ii: Spatial stratification and intermittency from lidar data. *Quarterly Journal of the Royal Meteorological Society*, 2008. 2

[41] R. T. H. Collis. Lidar: A new atmospheric probe. *Quarterly Journal of the Royal Meteorological Society*, 1966. 2

[42] Targ, Russell, Steakley, Bruce C., Hawley, James G., Ames, Lawrence L., Forney, Paul, Swanson, David, Stone, Richard, Otto, Robert G., Zarifis, Vassilis, Brockman, and Philip. Coherent lidar airborne wind sensor ii: flight-test results at 2 and 10 vm. *Applied Optics*, 1996. 2

[43] Mylapore, Anand R., Prasad, Narasimha S., Gerashchenko, and Sergiy. Development and wind tunnel testing of a novel 3d scanning lidar for global velocimetry. *American Institute of Aeronautics and Astronautics AIAA Aviation 2019 Forum - Dallas, Texas*, 2019. 2

[44] MarketsandMarketsy. *https://www.marketsandmarkets.com/*. 2

[45] YOLE DEVELOPPEMENT. *http://www.yole.fr/index.aspx*. 2

[46] Point of Beginning. *https://www.pobonline.com/*. 2

[47] Market research future. *https://www.marketresearchfuture.com/*. 2

[48] Claus Weitkamp. Lidar range-resolved optical remote sensing of the atmosphere. *Optical Science, Springer*, 2005. 4, 5, 6, 8, 9, 11

[49] R. Gai, W. Gong, J. Xu, X. Ren, and D. Liu. The edge technique as used in brillouin lidar for remote sensing of the ocean. *Applied Physics B*, pages B 79, 245–248, 2004. 5

[50] Paul McManomon. Field guid to lidar. *SPIE*, FG36:B 79, 245–248, 2004. 8

[51] Burhan Davarcioglu. An overviewof diodepumped solidstate (dpss) lasers. *International Archive of Applied Sciences and Technology*. 12

[52] Guiqiu Li, Shengzhi Zhao, Hongming Zhao, Kejian Yang, and Shuanghong Ding. Rate equations and solutions of a laser-diode end-pumped passively q-switched intracavity doubling laser by taking into account intracavity laser spatial distribution. *Optics Communications*. 14

[53] Jingang Liu, Deyuan Shen, Siu-Chung Tam, and Yee-Loy Lam. Modeling pulse shape of q-switched lasers. *IEEE Journal of Quantum Electronics*. 14

[54] T. Erneux, P. Peterson, and A. Gavrielides. The pulse shape of a passively q-switched microchip laser. *The European Physical Journal D / Atomic, Molecular, Optical and Plasma Physics*. 14

[55] Yumoto, Masaki, Saito, Norihito, Urata, Yoshiharu, Wada, and Satoshi. 128 mj/pulse, laser-diode-pumped, q-switched tm:yag laser. *IEEE Journal of Selected Topics in Quantum Electronics*. 14, 34

[56] Dallas, J. L., Afzal R. S., and Stephen M. A. Demonstration and characterization of a multibillion-shot, 25-mj, 4-ns, q-switched nd:yag laser. *Applied Optics*. 14

[57] Y. Wang, L. Huang, M. Cong, H. Zhang, M. Lei, and F. He. 1 mhz repetition rate single-frequency gain-switched nd:yag microchip laser. *Applied Optics*. 14

[58] A. E. Siegman. Lasers. *University Science Books*. 15, 23, 32

[59] Walter Koechner. Solid-state laser engineering. *Springer*. 15, 16, 24, 25, 66, 67

[60] Orazio Svelto. Principles of lasers. *Springer*. 15

[61] Federico Pirzio, Jacopo Rubens Negri, Sara Pizzurro, Enrico Piccinini, and Antonio Agnesi. Assessment of broad usability of a simple analytic model for passively q-switched lasers with cr:yag saturable absorbers. *Journal of the Optical Society of America B*, 2020. 17, 55

[62] P. Misra, K. Ranganathan, and S.M. Oak. High efficiency tem00 mode, diode-pumped, conduction-cooled, nd:yag zig-zag slab laser. *Optics Communications*. 25

[63] D.C. Hanna, C.G. Sawyers, and M.A. Yuratich. Large volume tem00 mode operation of nd : Yag lasers. *Optics Communications*. 25

[64] A.J. Berry, D.C. Hanna, and C.G. Sawyers. High power, single frequency operation of a q-switched tem00 mode ndyag laser. *Applied Optics*. 25

[65] Friel, Graham J., Kemp, Alan J., Lake, Tanya K., Sinclair, and Bruce D. Compact and efficient nd:yvo 4 laser that generates a tunable single-frequency green output. *Applied Optics*. 25

[66] T.K. Lake, A.J. Kemp, G.J. Friel, and B.D. Sinclair. Compact and efficient single-frequency nd : Yvo4 laser with variable longitudinal-mode discrimination. *IEEE Photonics Technology Letters*. 25

[67] Owyoung, Adelbert, Hadley G. R., Esherick, Peter, Schmitt R. L., and Rahn L. A. Gain switching of a monolithic single-frequency laser-diode-excited nd:yag laser. *Optics Letters*. 25

[68] Chen Y.F., Huang T.M., and Wang C.L. Passively q-switched diode-pumped nd: Yvo4/cr4+:yag single-frequency microchip laser. *Optics Letters*. 25

[69] Vorobiev, N. Glebov L., and Smirnov V. Single-frequency-mode q-switched nd:yag and er:glass lasers controlled by volume bragg gratings. *Optics Express*. 26

[70] White, Andrew, Elder, Ian, Hall, Gavin, Titterton, David H., Richardson, and Mark A. Single longitudinal mode and dual wavelength cw vbg lasers at 1342nm and 1064nm. *SPIE Proceedings [SPIE SPIE Security + Defence - Edinburgh, United Kingdom (Monday 24 September 2012)] Technologies for Optical Countermeasures IX*. 26

[71] Y. Zhang, C. Gao, M. Gao, Z. Lin, and R. Wang. A diode pumped tunable single-frequency tm:yag laser using twisted-mode technique. *Laser Physics Letters*. 26

[72] E. Wu, H. Pan, S. Zhang, and H. Zeng. High power single-longitudinal-mode operation in a twisted-mode-cavity laser with a c-cut nd:gdvo4crystal. *Applied Physics B: Lasers and Optics*. 26

[73] Erjuan Hao, Huiming Tan, Te Li, and Longsheng Qian. Single-frequency laser at 473nm by use of twisted-mode technique. *Optics Communications*. 26

[74] Pan, Haifeng, Xu, Shixiang, Zeng, and Heping. Passively q-switched single-longitudinal-mode c-cut nd:gdvo4 laser with a twisted-mode cavity. *Optics Express*. 26

[75] Nakagawa K., Shimizu Y., and Ohtsu M. High power diode-laser-pumped twisted-mode nd:yag laser. *IEEE Photonics Technology Letters*. 26

[76] Zhang X.M., Liu A.Q., Lu C., and Tang D.Y. Continuous wavelength tuning in micromachined littrow external-cavity lasers. *IEEE Journal of Quantum Electronics*. 26

[77] A. Saha, A. Ray, S. Mukhopadhyay, P.K. Datta, P.K. Dutta, and S.M. Saltiel. Littrow-type discretely tunable,q-switched nd:yag laser around 1.3. *Applied Physics B: Lasers and Optics*. 26

[78] de Labachelerie M. and G. Passedat. Mode-hop suppression of littrow grating-tuned lasers. *Applied Optics*. 26

[79] Zhihong Gao, Qibo Feng, Wenxi Zhang, Xinxin Kong, Boxia Yan, Yan Qi, Zhou Wub, and Yang Li. Single longitudinal mode operation in diode-end-pumped wedge nd:yvo4 laser. *Optics Communications*. 26

[80] Hercher and Michael. Tunable single mode operation of gas lasers using intracavity tilted etalons. *Applied Optics*. 26

[81] X.L. Zhang, L. Li, J.H. Cui, Y.L. Ju, and Y.Z. Wang. Single longitudinal mode and continuously tunable frequency tm,ho:ylf laser with two solid etalons. *Laser Physics Letters*. 26

[82] Zongfu Hu. To narrow laser linewidth by utilizing dispersion characteristics of gires-tournois etalon. *Chinese Optics Letters*. 26

[83] Mironov E A, Voitovich A V, and Palashov O V. Faraday isolator stably operating in a wide temperature range. *Laser Physics Letters*. 27

[84] Aplet L. J. and Carson J. W. A faraday effect optical isolator. *Applied Optics*. 27

[85] Thompson, Benjamin A., Minassian, Ara, Damzen, and Michael J. Unidirectional single-frequency operation of a nd:yvo4 ring laser with and without a faraday element. *Applied Optics*. 27

[86] Ke ying Wu, Su hui Yang, and Guang hui Wei. The non-planar single-frequency ring laser with variable output coupling. *Optics Communications*. 28

[87] Qing Wang, Chunqing Gao, Yan Zhao, Suhui Yang, Guanghui Wei, and Dongmei Hong 2. Laser-diode-pumped 1319-nm monolithic non-planar ring single-frequency laser. *Chinese Optics Letters*. 28

[88] Burdack, Peer, Fox, Thomas, Bode, Markus, Freitag, and Ingo. 1 w of stable single-frequency output at 1.03 µm from a novel, monolithic, non-planar yb:yag ring laser operating at room temperature. *Optics Express*. 28

[89] Koch, Peter, Bartschke, Juergen, L'huillier, and Johannes A. High-power actively q-switched single-mode 1342 nm nd:yvo_4 ring laser, injection-locked by a cw single-frequency microchip laser. *Optics Express*. 28

[90] Norman P. Barnes and James C. Barnes. Injection seeding i:theory. *IEEE Journal of quantum electronics*. 31

[91] Andrew J.MCGrath, Jesper Munch, Geral Smith, and Peter Veitch. Injection-seeded, single-frequency, q-switched erbium:glass laser for remote sensing. *Applied Optics*. 31

[92] F. R. Faxvog. Modes of a unidirectional ring laser. *Optics Letters*. 31

[93] P.C. Shardlow and M.J. Damzen. 20w single longitudinal mode nd:yvo4 retro-reflection ring laser operated as a self-intersecting master oscillator power amplifier. *Applied Physics B*. 32

[94] Bright Solutions S.r.l. https://brightsolutions.it/bdl-bfp/. 36

[95] Jacopo Rubens Negri, Federico Pirzio, , and Antonio Agnesi. Passively q-switched single-frequency nd:yvo4 ring laser with external feedback. *Optics Express*, 2018. 42

[96] F. Cornacchia M. Tonelli G. Turri, H. P. Jenssen and M. Bass. Temperature-dependent stimulated emission cross section in nd3+:yvo4 crystals. *J. Opt. Soc. Am. B*, 2009. 43

[97] Y. Isyanova and D. Welford. Temporal criterion for single-frequency operation of passively q-switched lasers. *Optics Letters*, 1999. 45

[98] Autodesk Inventor 2018. *https://www.autodesk.it/*. 49

[99] J.A. Caird, S.A. Payne, P.R. Staber, A.J. Ramponi, L.L. Chase, and W.F. Krupke. Quantum electronic properties of the na/sub 3/ga/sub 2/li/sub 3/f/sub 12/:cr/sup 3+/ laser. *IEEE Journal of Quantum Electronics*. 51

[100] M. C. Gupta. Handbook of photonics. *CRC Press*, 1997. 55

[101] Brian Cole, Jonathan Lei, Tom DiLazaro, Bradley Schilling, and Lew Goldberg. Optical triggering of a q-switched nd:yag laser via transverse bleaching of a cr:yag saturable absorber. *Applied Optics*, 2009. 56, 58

[102] http://www.roditi.com/Laser/$Cr4_Y$ag.html. Cr4:yag passive q-switch crystals. *The Roditi International Corporation Ltd*. 56

[103] Jacopo Rubens Negri, Federico Pirzio, , and Antonio Agnesi. *Optics Letters*, 2019. 58

[104] Anthony K. Y., NgaiStefan T., PersijnMaarten M. J. W., van HerpenSimona M. CristescuFrans, and J. M. Harren. Photoacoustic spectroscopy using continuous wave optical parametric oscillators. *Mid-Infrared Coherent Sources and Applications*, 2008. 63

[105] V. A. Serebryakov, E. V. Boiko, N. N. Petrishchev, and A. V. Yan. Medical applications of mid-ir lasers. problems and prospects. *J. Opt. Technol.*, 2010. 63

[106] Sova, Raymond M., Thomas, Michael E., Tobin, David, Byrum, Daniel, Strow, L. Larrabee, Leonelli, Joseph, Killinger, Dennis K., Vaughan, William, Yost, and Michael G. Characterization of candidate dial lidar water-vapor and carbon dioxide absorption lines in the 2-um region. *SPIE Proceedings*, 1995. 63

[107] P. Geiser, U. Willer, and W. Schade. Picosecond mid-infrared lidar system. *Conference on Lasers and Electro-Optics (CLEO)*, 2005. 63

[108] R. W. Boyd. Nonlinear optics. *Boston, Academic Press*, 2008. 64

[109] J. A. Armstrong, N. Bloembergen, J. Ducuing, and P. S. Pershan. Interactions between light waves in a nonlinear dielectric. *The Physical Review*, 1962. 65

[110] John D. Bierlein and Herman Vanherzeele. Potassium titanyl phosphate: properties and new applications. *Journal of the Optical Society of America B*, 1989. 65

[111] A. Hildenbrand, F. R. Wagner, H. Akhouayri, J.-Y. Natoli, M. Commandré, F. Théodore, , and H. Albrecht. Laser-induced damage investigation at 1064 nm in ktiopo$_4$ crystals and its analogy with rbtiopo$_4$. *Applied Optics*, 2009. 66

[112] Tso Yee Fan, C. E. Huang, B. Q. Hu, R. C. Eckardt, Y. X. Fan, Robert L. Byer, and R. S. Feigelson. Second harmonic generation and accurate index of refraction measurements in flux-grown ktiopo$_4$. *Applied Optics*, 1987. 66

[113] Karlsson H. and Laurell F. Electric field poling of flux grown ktiopo$_4$. *Applied Physics Letters*, 1997. 66

[114] Andrius Zukauskas, Nicky Thilmann, Valdas Pasiskevicius, Fredrik Laurell, and Carlota Canalias. 5 mm thick periodically poled rb-doped ktp for high energy optical parametric frequency conversion. *Optical Materials Express*, 2011. 66

[115] Q. JiangPam, A ThomasPam, A ThomasK., B. HuttonRoger, C C WardRoger, and C C Ward. Rb-doped potassium titanyl phosphate for periodic ferroelectric domain inversion. *Journal of Applied Physics*, 2002. 66

[116] Canalias Carlota and Pasiskevicius Valdas. Mirrorless optical parametric oscillator. *Nature Photonics*, 2007. 69

[117] Strömqvist Gustav, Pasiskevicius Valdas, Canalias Carlota, Aschieri Pierre, Picozzi Antonio, and Montes Carlos. Temporal coherence in mirrorless optical parametric oscillators. *Journal of the Optical Society of America B*, 2012. 69

[118] Yan, Xin, Yang, Maosheng, Zhang, Zhang, Liang, Lanju, Wei, Dequan, Wang, Meng, Zhang, Mengjin, Wang, Tao, Liu, Longhai, Xie, Jianhua, Yao, and Jianquan. The terahertz electromagnetically induced transparency-like metamaterials for sensitive biosensors in the detection of cancer cells. *Biosensors and Bioelectronics*, 2018. 69

[119] N. C. Currie, F. J. Demma, D. D. Ferris, B. R. Kwasowsky, R. W. McMillan, and M. C. Wicks. Infrared and millimeter-wave sensors for military special operations and law enforcement applications. *Biosensors and Bioelectronics*, 1996. 69

[120] N. C. Currie, F. J. Demma, D. D. Ferris, B. R. Kwasowsky, R. W. McMillan, and M. C. Wicks. Infrared and millimeter-wave sensors for military special operations and law enforcement applications. *Biosensors and Bioelectronics*, 1996. 69

[121] Kai Chang, Michael A. Pollock, Michael K. Skrehot, and Jerry Suddath G. Dickey. System feasibility study of a microwave/millimeter-wave radar for space debris tracking. *Journal of Infrared, Millimeter and Terahertz Waves*, 1989. 69